

ISSN 2667-4211

ESKİŞEHİR TECHNICAL UNIVERSITY
JOURNAL OF SCIENCE AND TECHNOLOGY
A – Applied Sciences and Engineering

Volume **24** Number **1** - March - **2023**



Volume: 24 / Number: 1 / March - 2023

Eskiőehir Technical University Journal of Science and Technology A - Applied Sciences and Engineering (ESTUJST-A) is a peer-reviewed and refereed international journal published by Eskiőehir Technical University. Since 2000, it has been regularly published and distributed biannually and it has been published quarterly and only electronically since 2016.

The journal accepts only manuscripts written in English.

The journal issues are published electronically in **March, June, September, and December**.

Eskiőehir Technical University Journal of Science and Technology A - Applied Sciences and Engineering is an international peer-reviewed and refereed journal published by Eskiőehir Technical University.

The journal is dedicated to the dissemination of knowledge in applied sciences and engineering disciplines.

The journal aims to publish high quality, original international scientific research articles with specific contributions to the literature in the field of engineering and applied sciences. The journal publishes research papers in the fields of applied science and technology such as Physics, Biology, Mathematics, Statistics, Chemistry and Chemical Engineering, Environmental Sciences and Engineering, Civil Engineering, Earth and Atmospheric Sciences, Electrical and Electronical Engineering, Computer Science and Informatics, Materials Sciences and Engineering, Mechanical Engineering, Mining Engineering, Industrial Engineering, Aeronautics and Astronautics, Pharmaceutical Sciences.

The journal publishes original research articles and special issue articles. All articles are peer-reviewed and the articles that have been evaluated are ensured to meet with researchers as soon as possible.

Eskiőehir Technical University holds the copyright of all published material that appear in Eskiőehir Technical University Journal of Science and Technology A - Applied Sciences and Engineering.

"Anadolu Üniversitesi Bilim ve Teknoloji Dergisi A - Uygulamalı Bilimler ve Mühendislik (Anadolu University Journal of Science and Technology A - Applied Sciences and Engineering)" published within Anadolu University started to be published within Eskiőehir Technical University which was established due to statute law 7141, in 2018. Hence, the name of the journal is changed to " Eskiőehir Technical University Journal of Science and Technology A - Applied Sciences and Engineering (Eskiőehir Teknik Üniversitesi Bilim ve Teknoloji Dergisi A - Uygulamalı Bilimler ve Mühendislik)".

Indexed by **DOAJ** - Directory of Open Access Journals, **EBSCO** and **ULAKBİM**



Volume: 24 / Number: 1 / March– 2023

Owner / Publisher: Prof. Dr. Adnan ÖZCAN for Eskiőehir Technical University

EDITOR-IN-CHIEF

Prof. Dr. Murat TANIŐLI

Eskiőehir Technical University, Institute of Graduate Programs, 26470 Eskiőehir, TURKEY

Phone: +90 222 213 7470

e-mail: mtanisli@eskisehir.edu.tr

CO-EDITOR IN CHIEF

Assoc. Prof. Dr. Tuğba ARAS

Eskiőehir Technical University, Institute of Graduate Programs, 26470 Eskiőehir, TURKEY

Phone: +90 222-213 7472

e-mail: tugbasoganci@eskisehir.edu.tr

CO-EDITOR IN CHIEF

Assit. Prof. Dr. Hüseyin Ersin EROL

Eskiőehir Technical University, Institute of Graduate Programs, 26470 Eskiőehir, TURKEY

Phone: +90 222-213 7473

e-mail: heerol@eskisehir.edu.tr

CONTACT INFORMATION

Eskiőehir Technical University Journal of Science and Technology

Eskiőehir Technical University, Institute of Graduate Programs, 26470 Eskiőehir, TURKEY

Phone: +90 222 213 7485

e-mail : btda@eskisehir.edu.tr



Volume: 24 / Number: 1 / March - 2023

OWNER

Adnan ÖZCAN, **The Rector of Eskiőehir Technical University**

EDITORIAL BOARD

Murat TANIŐLI, **Editor in Chief**

Tuğba ARAS, **Co-Editor in Chief**

Hüseyin Ersin EROL, **Co-Editor in Chief**

LANGUAGE EDITOR-ENGLISH

İlker DEMİROĐLU

SECTION EDITORS

Emin AÇIKKALP (ESTU, Turkey)
Őener AĐALAR (ESTU, Turkey)
Ziya AKÇA (Eskisehir Osmangazi University, Turkey)
Haydar ARAS (Eskisehir Osmangazi University, Turkey)
Tuğba ARAS (ESTU)
Funda ATEŐ (ESTU, Turkey)
Uğur AVDAN (ESTU, Turkey)
Nezihe AYAS (ESTU, Turkey)
Doç. Dr. Rukiye AYRANCI (Kütahya Dumlupınar University)
Özge BAĐLAYAN (ESTU, Turkey)
Recep BAKIŐ (ESTU, Turkey)
Müfide BANAR (ESTU, Turkey)
Ayőe H. BİLGE (Kadir Has University, Turkey)
Mehmet CANDAN (ESTU, Turkey)
Özgür CEYLAN (ESTU, Turkey)
Rasime DEMİREL (ESTU, Turkey)
İlker DEMİROĐLU (ESTU, Turkey)
Sedef DİKMEN (ESTU, Turkey)
Faruk DİRİSAĐLUK (Eskisehir Osmangazi University)
Barıő ERBAŐ (ESTU, Turkey)
Ömer Nezihe GEREK (ESTU, Turkey)
Özer GÖK (ESTU, Turkey)
Serdar GÖNCÜ (ESTU, Turkey)
Zerrin AŐAN GREENACRE (ESTU, Turkey)
Cihan KALELİ (ESTU, Turkey)
Gordona KAPLAN (ESTU, Turkey)
T. Hikmet KARAKOÇ (ESTU, Turkey)

Onur KAYA (ESTU, Turkey)
Murat KILIÇ (ESTU, Turkey)
Sabiha KOCA (Eskiőehir Osmangazi University, Turkey)
Semra KURAMA (ESTU, Turkey)
Gülbin KURTAY (Ankara University)
Anatoly NİKANOV (Saratov State Technical University, Slovenia)
Murad OMAROV (Kharkiv National University of Radio Electronics, Ukraine)
Emre Aytuğ ÖZSOY (ESTU, Turkey)
Özlem ONAY (ESTU, Turkey)
Gürkan ÖZTÜRK (ESTU, Turkey)
Emrah PEKKAN (ESTU, Turkey)
Najeeb REHMAN (Comsat University, Pakistan)
İsmail Hakkı SARPÜN (Akdeniz University, Turkey)
Sevil SÖYLEYİCİ (Pamukkale University)
Uğur SERİNCAN (ESTU, Turkey)
Cem SEVİK (ESTU, Turkey)
İlkin YÜCEL ŐENGÜN (Ege University, Turkey)
Aynur ŐENSOY ŐORMAN (ESTU, Turkey)
Sevil ŐENTÜRK (ESTU, Turkey)
Engin TIRAŐ (ESTU, Turkey)
Ümran Tezcan ÜN (ESTU, Turkey)
Önder TURAN (ESTU, Turkey)
Osman TUTAL (ESTU, Turkey)
Muammer TÜN (ESTU, Turkey)
Gülay ÜNAL (ESTU, Turkey)
Gülgün YILMAZ ÜNAL (ESTU, Turkey)

Secretary/Typset

Handan YİĐİT



ABOUT

Eskişehir Technical University Journal of Science and Technology A - Applied Sciences and Engineering (ESTUJST-A) is a peer-reviewed and refereed international journal published by Eskişehir Technical University. Since 2000, it has been regularly published and distributed biannually and it has been published quarterly and only electronically since 2016.

The journal accepts only manuscripts written in English.

The journal issues are published electronically in **MARCH, JUNE, SEPTEMBER, and DECEMBER.**

AIM AND SCOPE

Eskişehir Technical University Journal of Science and Technology A - Applied Sciences and Engineering is an international peer-reviewed and refereed journal published by Eskişehir Technical University.

The journal is dedicated to the dissemination of knowledge in applied sciences and engineering disciplines.

The journal aims to publish high quality, original international scientific research articles with specific contributions to the literature in the field of engineering and applied sciences. The journal publishes research papers in the fields of applied science and technology such as Physics, Biology, Mathematics, Statistics, Chemistry and Chemical Engineering, Environmental Sciences and Engineering, Civil Engineering, Earth and Atmospheric Sciences, Electrical and Electronical Engineering, Computer Science and Informatics, Materials Sciences and Engineering, Mechanical Engineering, Mining Engineering, Industrial Engineering, Aeronautics and Astronautics, Pharmaceutical Sciences.

The journal publishes original research articles and special issue articles. All articles are peer-reviewed and the articles that have been evaluated are ensured to meet with researchers as soon as possible.

PEER REVIEW PROCESS

Manuscripts are first reviewed by the editorial board in terms of its its journal's style rules scientific content, ethics and methodological approach. If found appropriate, the manuscript is then send to at least two renown referees by editor. The decision in line with the referees may be an acceptance, a rejection or an invitation to revise and resubmit. Confidential review reports from the referees will be kept in archive. All submission process manage through the online submission systems.

OPEN ACCESS POLICY

This journal provides immediate open access to its content on the principle that making research freely available to the public supports a greater global exchange of knowledge. Copyright notice and type of licence : **CC BY-NC-ND.**

PRICE POLICY

Eskişehir Technical University Journal of Science and Technology A - Journal of Applied Sciences and Engineering is an English, peer-reviewed, scientific, free of charge open-access-based journal. The author is not required to pay any publication fees or article processing charges (APCs) for peer-review administration and management, typesetting, and open-access. Articles also receive Digital Object Identifiers (DOIs) from the CrossRef organization to ensure they are always available.

ETHICAL RULES

You can reach the Ethical Rules in our journal in full detail from the link below:

<https://dergipark.org.tr/en/pub/estubtda/policy>

Ethical Principles and Publication Policy

Policy & Ethics

Assessment and Publication

As a peer-reviewed journal, it is our goal to advance scientific knowledge and understanding. We adhere to the guideline and ethical standards from the Committee on Publication Ethics (COPE) and the recommendations of ICMJE (International Committee of Medical Journal Editors) regarding all aspects of publication ethics and cases of research and publication misconduct to ensure that all publications represent accurate and original work and that our peer review process is structured without bias. We have outlined a set of ethical principles that must be followed by all authors, reviewers, and editors.

All manuscripts submitted to our journals are pre-evaluated in terms of their relevance to the scope of the journal, language, compliance with writing instructions, suitability for science, and originality, by taking into account the current legal requirements regarding copyright infringement and plagiarism. Manuscripts that are evaluated as insufficient or non-compliant with the instructions for authors may be rejected without peer review.

Editors and referees who are expert researchers in their fields assess scientific manuscripts submitted to our journals. A blind peer review policy is applied to the evaluation process. The Editor-in-Chief, if he/she sees necessary, may assign an Editor for the manuscript or may conduct the scientific assessment of the manuscript himself/herself. Editors may also assign referees for the scientific assessment of the manuscript and make their decisions based on reports by the referees. The Editor-in-Chief makes the final decision regarding the publishing of the manuscript.

Articles are accepted for publication by the Editor-in-Chief in accordance with the COPE (Committee on Publication Ethics). Authors can access this information online via the journals' websites (<https://publicationethics.org/>). Articles are accepted for publication on the understanding that they have not been published and are not going to be considered for publication elsewhere. Authors should certify that neither the manuscript nor its main contents have already been published or submitted for publication in another journal.

The journal adapts the COPE guidelines to satisfy the high-quality standards of ethics for authors, editors, and reviewers:

Duties of Editors-in-Chief and co-Editors

The crucial role of the journal Editor-in-Chief and co-Editors is to monitor and ensure the fairness, timeliness, thoroughness, and civility of the peer-review editorial process. The main responsibilities of Editors-in-Chief are as follows:

- Selecting manuscripts suitable for publication while rejecting unsuitable manuscripts,
- Ensuring a supply of high-quality manuscripts to the journal by identifying important,
- Increasing the journal's impact factor and maintaining the publishing schedule,
- Providing strategic input for the journal's development,

Duties of Editors

The main responsibilities of editors are as follows:

- An editor must evaluate the manuscript objectively for publication, judging each on its quality without considering the nationality, ethnicity, political beliefs, race, religion, gender, seniority, or institutional affiliation of the author(s). Editors should decline any assignment when there is a potential for conflict of interest.
- Editors must ensure the document(s) sent to the reviewers does not contain information of the author(s) and vice versa.
- Editors' decisions should be provided to the author(s) accompanied by the reviewers' comments and recommendations unless they contain offensive or libelous remarks.
- Editors should respect requests (if well reasoned and practicable) from author(s) that an individual should not review the submission.
- Editors and all staff members should guarantee the confidentiality of the submitted manuscript.
- Editors should have no conflict of interest with respect to articles they reject/accept. They must not have a conflict of interest with the author(s), funder(s), or reviewer(s) of the manuscript.
- Editors should strive to meet the needs of readers and authors and to constantly improve the journal.

Duties of Reviewers/Referees

The main responsibilities of reviewers/referees are as follows:

- Reviewers should keep all information regarding papers confidential and treat them as privileged information.
- Reviews should be conducted objectively, with no personal criticism of the author.
- Reviewers assist in the editorial decision process and as such should express their views clearly with supporting arguments.
- Reviewers should complete their reviews within a specified timeframe (maximum thirty-five (35) days). In the event that a reviewer feels it is not possible for him/her to complete the review of the manuscript within a stipulated time, then this information must be communicated to the editor so that the manuscript could be sent to another reviewer.
- Unpublished materials disclosed in a submitted manuscript must not be used in a reviewer's personal research without the written permission of the author. Information contained in an unpublished manuscript will remain confidential and must not be used by the reviewer for personal gain.
- Reviewers should not review manuscripts in which they have conflicts of interest resulting from competitive, collaborative, or other relationships or connections with any of the authors, companies, or institutions connected to the papers.

- Reviewers should identify similar work in published manuscripts that has not been cited by the author. Reviewers should also notify the Editors of significant similarities and/or overlaps between the manuscript and any other published or unpublished material.

Duties of Authors

The main responsibilities of authors are as follows:

- The author(s) should affirm that the material has not been previously published and that they have not transferred elsewhere any rights to the article.
- The author(s) should ensure the originality of the work and that they have properly cited others' work in accordance with the reference format.
- The author(s) should not engage in plagiarism or in self-plagiarism.
- On clinical and experimental humans and animals, which require an ethical committee decision for research in all branches of science;

All kinds of research carried out with qualitative or quantitative approaches that require data collection from the participants by using survey, interview, focus group work, observation, experiment, interview techniques,

Use of humans and animals (including material/data) for experimental or other scientific purposes,

- Clinical studies on humans,
- Studies on animals,
- Retrospective studies in accordance with the law on the protection of personal data, (Ethics committee approval should have been obtained for each individual application, and this approval should be stated and documented in the article.)

Information about the permission (board name, date, and number) should be included in the "Method" section of the article and also on the first/last page.

During manuscript upload, the "Ethics Committee Approval" file should be uploaded to the system in addition to the manuscript file.

In addition, in case reports, it is necessary to include information on the signing of the informed consent/ informed consent form in the manuscript.

- The author(s) should suggest no personal information that might make the identity of the patient recognizable in any form of description, photograph, or pedigree. When photographs of the patient were essential and indispensable as scientific information, the author(s) have received consent in written form and have clearly stated as much.
- The author(s) should provide the editor with the data and details of the work if there are suspicions of data falsification or fabrication. Fraudulent data shall not be tolerated. Any manuscript with suspected fabricated or falsified data will not be accepted. A retraction will be made for any publication which is found to have included fabricated or falsified data.
- The author(s) should clarify everything that may cause a conflict of interests such as work, research expenses, consultant expenses, and intellectual property.
- The author(s) must follow the submission guidelines of the journal.
- The author(s) discover(s) a significant error and/or inaccuracy in the submitted manuscript at any time, then the error and/or inaccuracy must be reported to the editor.
- The author(s) should disclose in their manuscript any financial or other substantive conflicts of interest that might be construed to influence the results or interpretation of their manuscript. All sources of financial support should be disclosed under the heading of "Acknowledgment" or "Contribution".
- The corresponding author should ensure that all appropriate co-authors and no inappropriate co-authors are included in the paper and that all co-authors have seen and approved the final version of the paper and have agreed to its submission for publication. All those who have made

significant contributions should be listed as co-authors. Others who have participated in certain substantive aspects of the research should be acknowledged or listed under the heading of “Author Contributions”.

Cancellations/Returns

Articles/manuscripts may be returned to the authors in order to increase the authenticity and/or reliability and to prevent ethical breaches, and even if articles have been accepted and/or published, they can be withdrawn from publication if necessary. The Editor-in-Chief of the journal has the right to return or withdraw an article/manuscript in the following situations:

- When the manuscript is not within the scope of the journal,
- When the scientific quality and/or content of the manuscript do not meet the standards of the journal and a referee review is not necessary,
- When there is proof of ruling out the findings obtained by the research, (When the article/manuscript is undergoing an assessment or publication process by another journal, congress, conference, etc.,)
- When the article/manuscript was not prepared in compliance with scientific publication ethics,
- When any other plagiarism is detected in the article/manuscript,
- When the authors do not perform the requested corrections within the requested time (maximum twenty-one (21) days),
- When the author does not submit the requested documents/materials/data etc. within the requested time,
- When the requested documents/materials/data etc. submitted by the author are missing for the second time,
- When the study includes outdated data,
- When the authors make changes that are not approved by the editor after the manuscript was submitted,
- When an author is added/removed, the order of the authors is changed, the corresponding author is changed, or the addresses of the authors are changed without the consent of the Editor-in-Chief,
- When a statement is not submitted indicating that approval of the ethics committee permission was obtained for the following (including retrospective studies):
- When human rights or animal rights are violated,

ETHICAL ISSUES

Plagiarism

The use of someone else’s ideas or words without a proper citation is considered plagiarism and will not be tolerated. Even if a citation is given, if quotation marks are not placed around words taken directly from other authors’ work, the author is still guilty of plagiarism. Reuse of the author’s own previously published words, with or without a citation, is regarded as self-plagiarism.

All manuscripts received are submitted to iThenticate®, which compares the content of the manuscript with a database of web pages and academic publications. Manuscripts are judged to be plagiarized or self-plagiarized, based on the iThenticate® report or any other source of information, will be rejected. Corrective actions are proposed when plagiarism and/or self-plagiarism is detected after publication. Editors should analyze the article and decide whether a corrected article or retraction needs to be published.

Open-access theses are considered as published works and they are included in the similarity checks.

iThenticate® report should have a maximum of 11% from a single source, and a maximum of 25% in total.

Conflicts of Interest

Eskişehir Technical University Journal of Science and Technology A - Applied Sciences and Engineering should be informed of any significant conflict of interest of editors, authors, or reviewers to determine whether any action would be appropriate (e.g. an author's statement of conflict of interest for a published work, or disqualifying a referee).

Financial

The authors and reviewers of the article should inform the journal about the financial information that will bring financial gain or loss to any organization from the publication of the article.

*Research funds; funds, consulting fees for a staff member; If you have an interest, such as patent interests, you may have a conflict of interest that needs to be declared.

Other areas of interest

The editor or reviewer may disclose a conflict of interest that, if known, would be embarrassing (for example, an academic affiliation or rivalry, a close relationship or dislike, or a person who may be affected by the publication of the article).

Conflict of interest statement

Please note that a conflict of interest statement is required for all submitted manuscripts. If there is no conflict of interest, please state “There are no conflicts of interest to declare” in your manuscript under the heading “Conflicts of Interest” as the last section before your Acknowledgments.

AUTHOR GUIDELINES

All manuscripts must be submitted electronically.

You will be guided stepwise through the creation and uploading of the various files. There are no page charges. Papers are accepted for publication on the understanding that they have not been published and are not going to be considered for publication elsewhere. Authors should certify that neither the manuscript nor its main contents have already been published or submitted for publication in another journal. We ask a signed copyright to start the evaluation process. After a manuscript has been submitted, it is not possible for authors to be added or removed or for the order of authors to be changed. If authors do so, their submission will be cancelled.

Manuscripts may be rejected without peer review by the editor-in-chief if they do not comply with the instructions to authors or if they are beyond the scope of the journal. After a manuscript has been accepted for publication, i.e. after referee-recommended revisions are complete, the author will not be permitted to make any changes that constitute departures from the manuscript that was accepted by the editor. Before publication, the galley proofs are always sent to the authors for corrections. Mistakes or omissions that occur due to some negligence on our part during final printing will be rectified in an errata section in a later issue.

This does not include those errors left uncorrected by the author in the galley proof. The use of someone else's ideas or words in their original form or slightly changed without a proper citation is considered plagiarism and will not be tolerated. Even if a citation is given, if quotation marks are not placed around words taken directly from another author's work, the author is still guilty of plagiarism. All manuscripts received are submitted to iThenticateR, a plagiarism checking system, which compares the content of the manuscript with a vast database of web pages and academic publications. In the received iThenticateR report; The similarity rate is expected to be below 25%. Articles higher than this rate will be rejected.

Uploading Articles to the Journal

Authors should prepare and upload 2 separate files while uploading articles to the journal. First, the Author names and institution information should be uploaded so that they can be seen, and then (using the additional file options) a separate file should be uploaded with the Author names and institution information completely closed. When uploading their files with closed author names, they will select the "Show to Referee" option, so that the file whose names are closed can be opened to the referees.

Preparation of Manuscript

Style and Format

Manuscripts should be **single column** by giving one-spaced with 2.5-cm margins on all sides of the page, in Times New Roman font (font size 11). Every page of the manuscript, including the title page, references, tables, etc., should be numbered. All copies of the manuscript should also have line numbers starting with 1 on each consecutive page.

Manuscripts must be upload as word document (*.doc, *.docx vb.). **Please avoid uploading texts in *.pdf format.**

Symbols, Units and Abbreviations

Standard abbreviations and units should be used; SI units are recommended. Abbreviations should be defined at first appearance, and their use in the title and abstract should be avoided. Generic names of chemicals should be used. Genus and species names should be typed in italic or, if this is not available, underlined.

Please refer to equations with capitalisation and unabbreviated (e.g., as given in Equation (1)).

Manuscript Content

Articles should be divided into logically ordered and numbered sections. Principal sections should be numbered consecutively with Arabic numerals (1. Introduction, 2. Formulation of problem, etc.) and subsections should be numbered 1.1., 1.2., etc. Do not number the Acknowledgements or References sections. The text of articles should be, if possible, divided into the following sections: Introduction, Materials and Methods (or Experimental), Results, Discussion, and Conclusion.

Title and contact information

The first page should contain the full title in sentence case (e.g., Hybrid feature selection for text classification), the full names (last names fully capitalised) and affiliations (in English) of all authors (Department, Faculty, University, City, Country, E-mail), and the contact e-mail address for the clearly identified corresponding author. The first page should contain the full title, abstract and keywords (both English and Turkish).

Abstract

The abstract should provide clear information about the research and the results obtained, and should not exceed 300 words. The abstract should not contain citations and must be written in Times New Roman font with font size 9.

Keywords

Please provide 3 to 5 keywords which can be used for indexing purposes.

Introduction

The motivation or purpose of your research should appear in the “Introduction”, where you state the questions you sought to answer, and then provide some of the historical basis for those questions.

Methods

Provide sufficient information to allow someone to repeat your work. A clear description of your experimental design, sampling procedures, and statistical procedures is especially important in papers describing field studies, simulations, or experiments. If you list a product (e.g., animal food, analytical device), supply the name and location of the manufacturer. Give the model number for equipment used.

Results

Results should be stated concisely and without interpretation.

Discussion

Focus on the rigorously supported aspects of your study. Carefully differentiate the results of your study from data obtained from other sources. Interpret your results, relate them to the results of previous research, and discuss the implications of your results or interpretations.

Conclusion

This should state clearly the main conclusions of the research and give a clear explanation of their importance and relevance. Summary illustrations may be included.

Acknowledgments

Acknowledgments of people, grants, funds, etc. should be placed in a separate section before the reference list. The names of funding organizations should be written in full.

Conflict of Interest Statement

The authors are obliged to present the conflict of interest statement at the end of the article after the acknowledgments section.

Author Contributions

All authors, author contributions and contribution rates should be clearly stated.

References

Writing Style; **AMA; References Writing format** should be used in the reference writing of our journal. If necessary, at this point, the reference writings of the articles published in our article can be examined.

Citations in the text should be identified by numbers in square brackets. The list of references at the end of the paper should be given in order of their first appearance in the text. All authors should be included in reference lists unless there are 10 or more, in which case only the first 10 should be given, followed by ‘et al.’. Do not use individual sets of square brackets for citation numbers that appear together, e.g., [2,3,5–9], not [2], [3], [5]–[9]. Do not include personal communications, unpublished data, websites, or other unpublished materials as references, although such material may be inserted (in parentheses) in the text. In the case of publications in languages other than English, the published English title should be provided if one exists, with an annotation such as “(article in Turkish with an abstract in English)”. If the publication was not

published with an English title, cite the original title only; do not provide a self-translation. References should be formatted as follows (please note the punctuation and capitalisation):

Journal articles

Journal titles should be abbreviated according to ISI Web of Science abbreviations.

Guyon I, Elisseeff A. An introduction to variable and feature selection. *J Mach Learn Res* 2003; 3: 1157-1182.

Izadpanahi S, Ozcinar C, Anbarjafari G, Demirel H. Resolution enhancement of video sequences by using discrete wavelet transform and illumination compensation. *Turk J Elec Eng & Comp Sci* 2012; 20: 1268-1276.

Books

Haupt RL, Haupt SE. *Practical Genetic Algorithms*. 2nd ed. New York, NY, USA: Wiley, 2004.

Kennedy J, Eberhart R. *Swarm Intelligence*. San Diego, CA, USA: Academic Press, 2001.

Chapters in books

Poore JH, Lin L, Eschbach R, Bauer T. Automated statistical testing for embedded systems. In: Zander J, Schieferdecker I, Mosterman PJ, editors. *Model-Based Testing for Embedded Systems*. Boca Raton, FL, USA: CRC Press, 2012. pp. 111-146.

Conference proceedings

Li RTH, Chung SH. Digital boundary controller for single-phase grid-connected CSI. In: *IEEE 2008 Power Electronics Specialists Conference*; 15–19 June 2008; Rhodes, Greece. New York, NY, USA: IEEE. pp. 4562-4568.

Theses

Boynukalin Z. *Emotion analysis of Turkish texts by using machine learning methods*. MSc, Middle East Technical University, Ankara, Turkey, 2012.

Tables and Figures

All illustrations (photographs, drawings, graphs, etc.), not including tables, must be labelled “Figure.” Figures must be submitted in the manuscript.

All tables and figures must have a caption and/or legend and be numbered (e.g., Table 1, Figure 2), unless there is only one table or figure, in which case it should be labelled “Table” or “Figure” with no numbering. Captions must be written in sentence case (e.g., Macroscopic appearance of the samples.). The font used in the figures should be Times New Roman. If symbols such as \times , μ , η , or ν are used, they should be added using the Symbols menu of Word.

All tables and figures must be numbered consecutively as they are referred to in the text. Please refer to tables and figures with capitalisation and unabbreviated (e.g., “As shown in Figure 2...”, and not “Fig. 2” or “figure 2”).

The resolution of images should not be less than 118 pixels/cm when width is set to 16 cm. Images must be scanned at 1200 dpi resolution and submitted in jpeg or tiff format. Graphs and diagrams must be drawn with a line weight between 0.5 and 1 point. Graphs and diagrams with a line weight of less than 0.5 point or more than 1 point are not accepted. Scanned or photocopied graphs and diagrams are not accepted.

Figures that are charts, diagrams, or drawings must be submitted in a modifiable format, i.e. our graphics personnel should be able to modify them. Therefore, if the program with which the figure is drawn has a “save as” option, it must be saved as *.ai or *.pdf. If the “save as” option does not include these extensions, the figure must be copied and pasted into a blank Microsoft Word document as an editable object. It must not be pasted as an image file (tiff, jpeg, or eps) unless it is a photograph.

Tables and figures, including caption, title, column heads, and footnotes, must not exceed 16 × 20 cm and should be no smaller than 8 cm in width. For all tables, please use Word’s “Create Table” feature, with no tabbed text or tables created with spaces and drawn lines. Please do not duplicate information that is already presented in the figures.

Article Corrections and Uploading to the System

Authors should upload the desired edits for their articles without destroying or changing the Template file of the article, by selecting and specifying the relevant edits as Colored, and also submit the Clean version of the article in 2 separate files (using the Additional file option if necessary). * In case of submitting a corrected article, a separate File in Reply to the Referees must be prepared and the "Reply to the Referees" option in the Add additional file option should be checked and uploaded. If a separate file is not prepared in response to the referees, the Author will definitely be asked to upload the relevant file again and the evaluation will be in the pending phase.

CONTENTS

RESEARCH ARTICLE

BIOCHEMICAL CHARACTERIZATION AND PARTIAL PURIFICATION OF A BACTERIOCIN LIKE-INHIBITORY SUBSTANCE PRODUCED FROM <i>Bacillus</i> sp. T68 STRAIN <i>S. Kaya Şen, H. Katı</i>	1
PHOTOLUMINESCENCE PROPERTIES OF Nd³⁺, Yb³⁺ CODOPED Ga₂O₃ NANOPARTICLES <i>A. Dulda</i>	14
ON THE EFFECTIVENESS OF PARAGRAPH VECTOR MODELS IN DOCUMENT SIMILARITY ESTIMATION FOR TURKISH NEWS CATEGORIZATION <i>A. Yürekli</i>	23
MODELING OF CO₂ EMISSION STATISTICS in TURKEY BY FUZZY TIME SERIES ANALYSIS <i>F. Çemrek</i>	35
QUARTZ FIBER RADOME AND SUBSTRATE FOR AEROSPACE APPLICATIONS <i>M. Bakır</i>	48
ASYMPTOTIC ANALYSIS OF ACOUSTIC GREEN'S FUNCTIONS <i>H. Yücel, Y. E. Uçar</i>	57
USING INTUITIONISTIC FUZZY C-MEANS CLUSTERING ALGORITHMS TO MODEL COVID-19 CASES FOR COUNTRIES IN THE WORLDWIDE <i>N. İnce, S. Şentürk</i>	71



RESEARCH ARTICLE

**BIOCHEMICAL CHARACTERIZATION AND PARTIAL PURIFICATION OF A
BACTERIOCIN LIKE-INHIBITORY SUBSTANCE PRODUCED FROM *Bacillus* sp. T68
STRAIN**

Sultan KAYA ŞEN¹ , Hatice KATI^{1,*} 

¹Department of Biology, Faculty of Arts and Sciences, Giresun University, Giresun, Turkey

ABSTRACT

Bacteriocins are peptides produced by various types of bacteria. Members of the *Bacillus* genus are known to produce compounds with inhibitory activity in protein structure against pathogenic and non-pathogenic microorganisms. In this study, a bacteriocin-like inhibitory substance (BLIS) synthesized by *Bacillus* sp. T68 strain, which was previously isolated from soil, was characterized. T68 strain was grown on different media to produce bacteriocin. Crude BLIS obtained was tested by well diffusion method against indicator bacterium. It was investigated within the temperature range of 10-121 °C and pH range from 3.0 to 10.0. It was examined in terms of different organic solvents, enzymes and chemicals. Extracellularly produced BLIS was partially purified by ammonium sulphate precipitation method and analyzed on SDS-PAGE. Activity of partially purified BLIS was investigated. It was observed that BLIS produced in Luria Bertani Broth medium was higher as compared to the other media against indicator bacterium at 30 °C for 24 h. BLIS activity maintained at low temperatures (10-40 °C) and lost completely at high temperatures (> 60 °C). It was detected that BLIS exhibited activity in the pH range between 5.0 and 10.0. The effect of EDTA on BLIS activity was slightly positive. Proteinase K and trypsin inhibited BLIS activity. Among the detergents, sodium dodecyl sulphate and Triton X-100 reduced BLIS activity, while Tween 20 and Tween 80 retained it. Additionally, it was determined that application of Tween 20 at 30 °C for 5 hours increased the BLIS activity by 40%. It was found that the solvents used other than butan 1-ol preserved the BLIS activity over 80%. Chloroform and isopropanol increased the BLIS activity slightly. An inhibitory zone formed by the BLIS corresponding to a molecular weight of about 15 kDa was detected. This BLIS exhibited stability over wide pH and temperature ranges and in organic solvent treatments.

Keywords: *Bacillus*, BLIS, Antibacterial activity, *Bacillus thuringiensis* subsp. *indiana*, Soil

1. INTRODUCTION

Some bacteria produce many inhibitory compounds that can prevent the growth or development of certain microorganisms or pathogens that cause degradation in foods [1,2]. Bacteriocin, one of these compounds, was first discovered by Andre Gratia in 1925 and this inhibitor substance produced by *E. coli* was called as colisin [3]. Bacteriocins have recently received particular attention for the control of food-borne pathogens [4]. The use of bacteriocins in the food industry reduces the need for chemical preservatives and at the same time reduces the food damage caused by heat treatment [5,6].

Bacteriocins are ribosomally synthesized natural peptides produced by bacteria that kill or inhibit the growth of related bacteria [7]. Bacteriocin studies have gained great importance in the fight against numerous pathogens and the increasing number of antibiotic resistant pathogens. Most bacteriocins are produced by lactic acid bacteria (LAB) [8,9]. Some bacteriocins obtained from LAB are widely used in the food industry.

*Corresponding Author: hatice.kati@giresun.edu.tr

Received: 19.01.2022 Published: 29.03.2023

The food industry faced a major challenge, opting for safer foods with longer shelf lives and minimally processed products without chemical preservatives [10]. The use of bacteriocins is critical for food preservation, because they extend the shelf life of foods, reduce the risk of contamination by foodborne pathogens, reduce economic losses, reduce the use of chemical preservatives, and bring to market “new” foods with lower acidity, lower salt content, and higher water content [11-13]. Nisin is the only bacteriocin commonly used as a food biopreservative. However, due to its low stability at neutral and alkaline pH and the emergence of nisin-resistant strains, new bacteriocins are needed for use in food biopreservation [14-18].

Unlike bacteriocins produced by LAB, which have a narrow antimicrobial spectrum [19], *Bacillus* bacteriocins attract attention [20]. *Bacillus* species are commonly found in almost all natural habitats and many other sources [21]. They produce important antimicrobial agents such as peptides, lipopeptides, antibiotics and bacteriocins [22]. After LAB, species in *Bacillus* genus have been extensively studied in terms of their bacteriocin and BLIS production. These studies identified many active molecules [23]. The *Bacillus* genus contains many species that have been found to be safe in the industry and food sector [24]. There are important species, such as LAB, registered as GRAS (generally recognized as safe) in the field of agriculture, industry and food. *Bacillus cereus* is one of the representatives of the genus *Bacillus*. The *Bacillus cereus* group consists of closely related species, including *B. anthracis*, *B. cereus*, *B. pseudomycoides* and *B. thuringiensis* [25,26]. In recent years, many bacteriocins have been identified in the *Bacillus cereus* group, such as lantibiotics, sactibiotics, circular bacteriocins and unmodified bacteriocins [26-29].

Bacillus sp. T68 strain was previously isolated from soil and found to have high antimicrobial activity against some tested bacteria [30]. Showing high antimicrobial activity against some pathogenic and non pathogenic bacteria make this *Bacillus* sp. T68 strain as a potential BLIS producer. In this study we aimed to identify the BLIS production ability of the *Bacillus* sp. T68 strain. Subsequently, the biochemical properties of the produced BLIS will be determined.

2. MATERIALS AND METHODS

In this study, the strain *Bacillus* sp. T68, which belongs to the *Bacillus cereus* group and has antibacterial activity [30], and *Bacillus thuringiensis* subsp. *indiana* HD521 (4S2, *Bacillus* Stock Center) was used as indicator.

2.1. BLIS Production

The BLIS production was carried out according to the methods described by Sensoy Karaoglu et al. [31] and Touraki et al. [32] with minor modifications. The preculture was prepared from the *Bacillus* sp. T68 strain in Nutrient Broth (NB) at 30 °C for about 18 h at 150 rpm (GFL 3031 incubator). To determine the effects of different media on BLIS production, Luria Bertani Broth (LBB), Tryptic Soy Broth (TSB) and NB were inoculated from preculture. Samples were incubated at 30 °C for 5 days (NUVE EN120) and 2 ml of the cultures were taken every 24 hours. The cultures were centrifuged at 10,000 rpm for 30 min. The supernatant obtained was filtered through a sterile membrane filter (Whatman) with a pore diameter of 0.2 µm and used as crude BLIS for further characterization. The antibacterial activity of crude BLIS was determined using the well diffusion assay against indicator bacterium (*Bacillus thuringiensis* subsp. *indiana* HD521).

2.2. Well Diffusion Assay

To determine crude BLIS activity, a well diffusion assay was performed according to the method of Rajaram et al. [33] with slight modification. The nutrient agar (NA) medium containing 40 µl of an overnight culture (16-18 h) of the indicator bacterium was poured into the petri dish. The activity was

determined by pouring 100 µL of the crude BLIS into the hole (6 mm) generated on the NA plates. The plates were incubated at 30 °C for about 16-18 h and after incubation, the clear zones formed around the holes were measured.

2.3. Characterization of BLIS

The effects of temperature, pH, some proteolytic enzymes, organic solvents, chemicals and detergents on crude BLIS activity were identified. All experiments were performed in duplicate. The following formula was used to calculate the residual activities in % [34].

$$\% = A * 100/K$$

Control zone diameter = K

Processed zone diameter = A

2.3.1. Effect of temperature on BLIS activity

To determine the effect of temperature on BLIS activity, the filtered supernatant was incubated at 10-90 °C for 30 min and at 121 °C for 15 min. Activity was then measured using the well diffusion assay.

2.3.2. Effect of pH on BLIS activity

Buffers (sodium acetate buffer, pH 3.0-5.0; potassium phosphate buffer, pH 6.0-7.0; Tris-HCl buffer, pH 8.0; and glycine NaOH buffer, pH 9.0-10.0) were prepared at a concentration of 10 mM for the pH experiments. The crude BLIS and pH buffer were mixed at a 1:1 ratio. The mixtures were treated at +4 °C for 24 h, and at 10 to 30 °C for 1 h. BLIS activity was measured using the well diffusion assay.

2.3.3. Effect of some organic solvents on BLIS activity

Organic solvents such as chloroform, acetonitrile, acetone, isopropanol, methanol, butan-1-ol, ethyl alcohol and hexane were used. Ethyl alcohol and hexane were added to the crude BLIS at a rate of 25% (v/v) and other solvents at a rate of 10% (v/v). Organic solvents without crude BLIS were used as negative controls, and crude BLIS without organic solvents were used as positive controls. BLIS activity was measured using the well diffusion assay.

2.3.4. Effect of some detergents and chemicals on BLIS activity

Sodium dodecyl sulfate (SDS), Tween 80, Tween 20 and Triton X-100 were used as detergents. The crude BLIS was incubated with different detergents at a final concentration of 1% (v/v) at 10 to 30 °C for 1 and 5 hours [35]. Untreated crude BLIS served as controls. BLIS activity was measured using the well diffusion assay.

The crude BLIS was incubated with ethylene diamine tetra-acetic acid (EDTA) at final concentrations of 0.1, 0.2, and 0.5 mM, at 10 to 30 °C for 1 and 5 h. At the end of this period, BLIS activity was measured using the well diffusion assay.

2.3.5. Effect of enzymes on BLIS activity

Proteinase K and trypsin enzymes were added to crude BLIS at a final concentration of 1 and 10 mg/ml, respectively. The mixtures were incubated at 37 °C for 1 and 2 h. Untreated crude BLIS were used as controls [36]. BLIS activity was measured using the well diffusion assay.

2.4. Partial Purification of BLIS

For the partial purification of the BLIS, ammonium sulfate was added to the crude BLIS to obtain 40%, 60%, and 80% saturation according to He et al. [37] with slight modifications. After each saturation, samples were centrifuged at 8,000 rpm for 10 min and the resulting pellets were dissolved in dH₂O and stored at -20 °C. BLIS activity was measured using the well diffusion assay.

2.5. Detection of BLIS Activity on Gel

The estimated molecular weight of the partially purified BLIS was determined by SDS-PAGE using 15% resolving and 5% stacking gels as described by Laemmli [38]. To detect the BLIS activity on gel, SDS and β -mercaptoethanol were not added to the sample buffer and the boiling step was also omitted. Electrophoresis was performed at 100 V. After electrophoresis, the gel was divided into two parts. To estimate the MW, one half, which contained the marker and samples, was placed in the staining solution prepared with Coomassie Brilliant Blue R-250 (CBB R-250) for about 2.5 h and then placed in the decolorizing solution. To detect the BLIS activity, the other half of the gel was transferred to the sterile dH₂O at +4 °C, which was changed at regular intervals during about 16 and 18 h to remove SDS according to Lim et al. [39] with slight modifications. The gel was then covered with NA medium containing indicator bacterium. Plate was incubated at 30 °C for about 16-18 h and observed for the presence of an inhibition zone for the direct detection of BLIS. After incubation, the activity was examined by measuring the clear zone and compared with the stained part.

3. RESULTS

3.1. BLIS Production

The antibacterial activities of the crude BLIS of *Bacillus* sp. T68 strain grown in different media and at different time points are shown in Figure 1. Cultivation of strain T68 at 24 h proved to be best for BLIS production on LB medium.

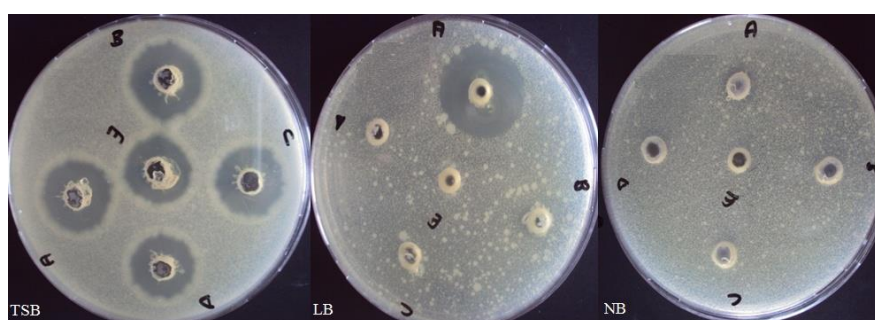


Figure 1. Antibacterial activities of crude BLIS by *Bacillus* sp. T68 in different media and at different time points. A) 24h, B) 48h, C) 72h, D) 96h, E) 120h.

3.2. Characterization of BLIS

Examination of the effect of temperature on BLIS activity identified good activity at between 10-40 °C, a decrease in activity between 50-60 °C and a loss of 100% of activity at temperatures above 60 °C. The highest BLIS activity was observed at 10 °C (Figure 2). The activity was 96% at 20 °C, 91% at 30 and 40 °C, 84% at 50 °C and 52% at 60 °C.

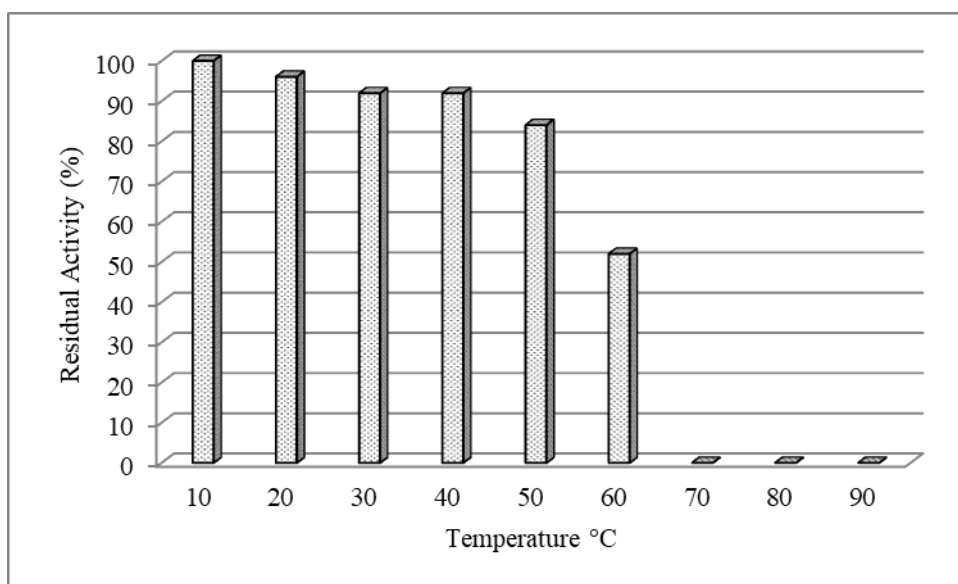


Figure 2. Effect of temperature on the activity of crude BLIS from strain *Bacillus* sp. T68.

When the effect of pH on BLIS activity was examined, it showed activity highest at pH 6 at 10 °C, highest at pH 10 at 30 °C. There was no loss of activity at pH 6, pH 9 and pH 10 at +4 °C (Figure 3).

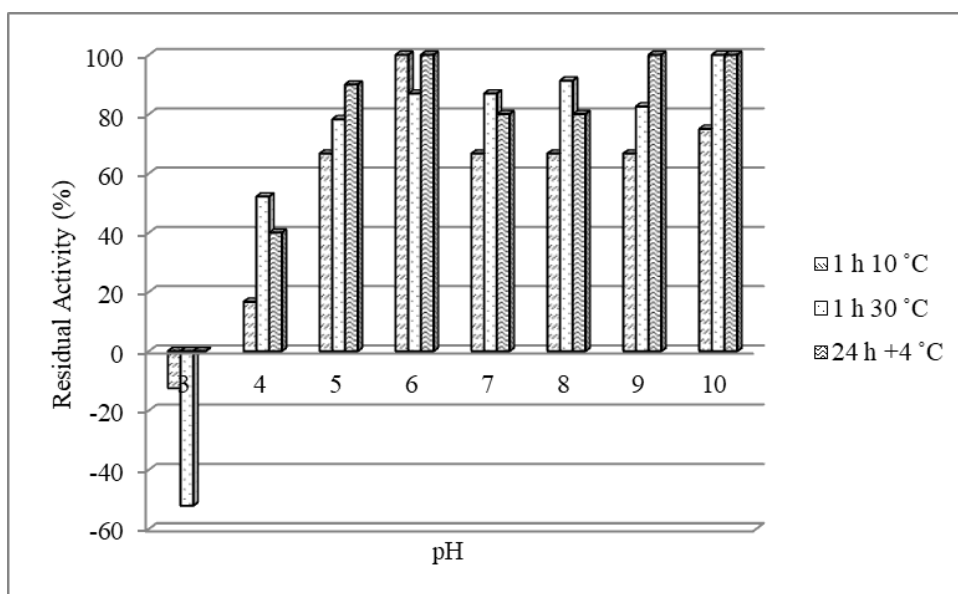


Figure 3. Effect of pH on crude BLIS obtained from *Bacillus* sp. T68 strain.

It was found that some organic solvents generally have a positive effect on crude BLIS activity. The activity of acetonitrile increased by 20%, that of ethyl alcohol by 12.5%, and that of hexane by 25% for 1 h at 10 °C, whereas the activity of methanol was reduced by 8.3%, that of butan-1-ol by 60% and that of chloroform by 10%. Isopropanol and acetone had no effect on the activity. The activity of acetonitrile and methanol for 1s at 30 °C increased by 13%, that butan-1-ol by 21%, that of isopropanol 31%, that of chloroform 33%, and that of ethyl alcohol 16%. Hexane and acetone had no effect on activity (Figure 4).

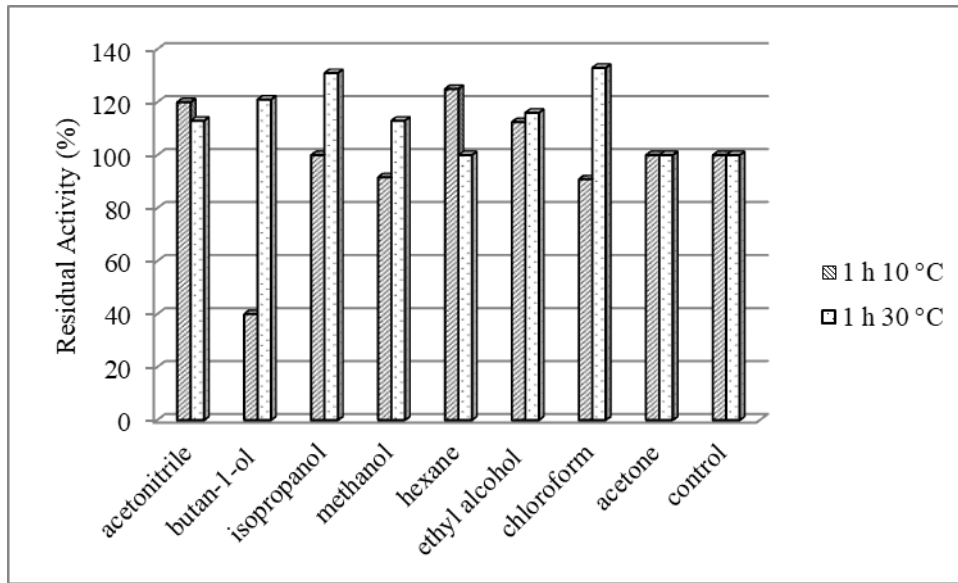


Figure 4. Effect of several organic solvents on crude BLIS obtained from *Bacillus* sp. T68 strain. 10% chloroform, acetonitrile, acetone, isopropanol, methanol, butan-1-ol, 25% ethyl alcohol and hexane solvents were used. Crude BLIS without organic solvents were used as positive controls.

When the effect of some detergents on crude BLIS was obtained, it was found that SDS and Triton X-100 were more effective in the activity for 1 and 5 h at 10 °C or 30 °C. For 1 h at 10 °C, Triton X-100 decreased activity by 91.7%, SDS decreased activity by 90.4% and Tween 80 decreased activity by 16.7%, while Tween 20 increased activity by 4.7%. For 5 h at 10 °C, Triton X-100 decreased activity by 83.3% and Tween 80 decreased activity by 16.6%, SDS inhibited activity 100%, and Tween 20 had no effect on activity. For 1 h at 30 °C, Triton X-100 decreased the activity by 75% while SDS inactivated it 100%, and activity increased by 16% in Tween 20 and Tween 80. For 5 h at 30 °C, Triton X-100 decreased activity by 80% while SDS inactivated it by 100%, and activity increased by 40% in Tween 20 and 25% in Tween 80 (Figure 5).

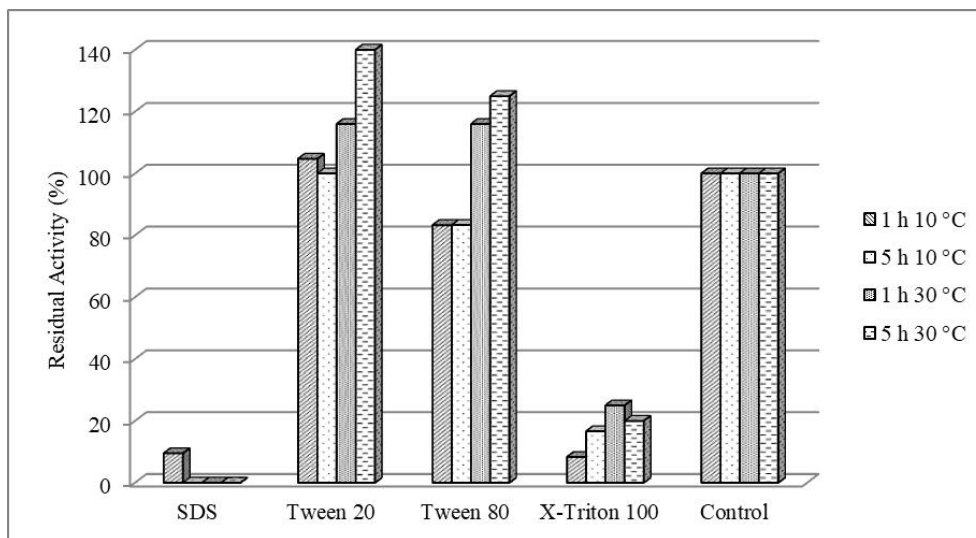


Figure 5. Effect of some detergents on crude BLIS from *Bacillus* sp. T68 strain. The crude BLIS was incubated with detergents at a final concentration of 1%. Untreated crude BLIS served as control.

For 1 h at 10 °C, EDTA increased BLIS activity by 4% at 0.1 mM, but by 8% at 0.2 mM and by 16% at 0.5 mM concentrations. For 5 h at 10 °C, activity decreased by 8% at 0.1 mM, increased by 12% at 0.2 mM and had no effect at 0.5 mM. At 1 h 30 °C, the activity increased by 10% at 0.1 mM, by 22% at 0.2 mM, and by 27% at 0.5 mM. While it did not affect the activity at 0.1 and 0.5 mM for 5 h at 30 °C, it increased by 9% at 0.2 mM.

Treatment with proteinase K resulted in 100% loss of activity. When treated with 1 and 10 mg/ml trypsin for 1 h at 37 °C, activity was reduced by 23% and 25%, respectively. For 2 h at 37 °C, activity was reduced by 53.5% and 76.4% upon treatment with 1 and 10 mg/ml trypsin, respectively.

3.3. Detection of BLIS Activity on Gel

Activity was observed in the ammonium sulfate precipitation of the crude BLIS of the T68 strain. The maximum antibacterial activity was found in the resolved precipitate with 40% saturation of ammonium sulfate. However, it still showed activity when 60 and 80 % saturation of ammonium sulfate was added. In the activity study, 40% saturation of ammonium sulfate precipitation, which showed the best activity, was used. Overlaying the gel with NA supplemented with the indicator strain revealed a single protein band in a region with antibacterial activity. The band had apparent molecular weight of about 15 kDa (Figure 6). The band corresponding to this region could not be seen on SDS-PAGE.

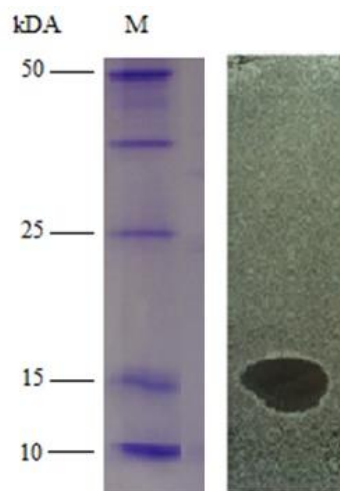


Figure 6. Activity of the BLIS (obtained through 40% ammonium sulfate precipitation). M: Marker (Promega)

4. DISCUSSION

Bacteriocins produced by the *Bacillus* genus are considered as important as those produced by LAB. Bacteriocins from *Bacillus* species, like those from LAB, have an important place for applications in human and animal health [39]. A wide variety of antimicrobial peptides with different chemical structures are produced by the genus *Bacillus* [40,41].

In the present study, isolation and characterization of a BLIS from *Bacillus* sp.T68 were performed.

The best antibacterial activity was found in LB medium for 24 h compared to other media. Different media have been used to produce bacteriocin from *Bacillus* species [31,37,42-44]. In a study using LAB isolates obtained from fish, it was reported that bacteriocin production increased to 72 h [45]. In

another study, the bacteriocin activity synthesized by *Bacillus thuringiensis* subsp. *entomocidus* was found to be higher in TSB and LBB medium compared to the other media [46]. Different media such as BHI and LB were used to produce bacteriocin by *Bacillus* species [37,42].

The antibacterial activity of BLIS in the present study was stable a wide temperature range and lost its activity at temperatures above 60 °C. Lee et al. [47] reported that a bacteriocin produced by *B. polyfermenticus* maintained its inhibitory activity up to 60 °C, and lost its activity after 30 min at 70 °C. The decreases in bacteriocin activity at high temperatures and denaturation or loss of total activity are due to the proteinaceous structure of bacteriocin [48]. Bacteriocin produced by *Brevibacterium linens* remained active for 30 minutes at 40-50 °C [49]. However, bacteriocin RX7 isolated from *Bacillus amyloliquefaciens* retained its activity at 100 °C for 30 minutes [39]. Bacthuricin F4 obtained from *Bacillus thuringiensis* subsp. *course* lost 80% of its activity at 90 °C within 30 min, but was protected at 40-70 °C [50].

The antibacterial activity of BLIS showed the best activity at pH 6-10 at different temperatures. It was observed that bacteriocin activity decreased or disappeared in acidic media at pH 9 and above [43,48,51]. In a study performed with Nisin, no activity was observed at pH 3, while the highest activity was observed at pH 6.5. Similarly, in a study performed with Sakasin A, the highest activity was observed at pH 5.5, while the activity decreased to 75% at pH 2 [52]. In other studies, bacteriocins from strains B10 [31] and LBM 5006 [43] were stable in a pH range of 3-9 and 3-8, respectively.

It has been found that BLIS generally has little or no effect on activity when treated with organic solvents such as acetonitrile, chloroform, ethyl alcohol, acetone, hexane, methanol, butan-1-ol and isopropanol. Many researchers have found that most bacteriocins produced by LABs are resistant to organic solvents [53-55]. In a study by Pirzada et al. [56], bacteriocin was found to remain active against propanol from organic solvents at a concentration of 1% and its activity was lost by acetone, methanol, heptane and chloroform.

In this study, SDS and Triton X-100 affected BLIS activity more than Tween 20 and Tween 80 and the complete disappearance of activity, especially when treated with SDS, suggests that the protein structure of bacteriocin is impaired. SDS and Triton X-100 treatment caused loss of activity and this effect became persistent. Another study investigated the effects of certain detergents on bacteriocin activity. The effect of detergents on bacteriocin activity provides information about the structure of the active molecule. Detergents form a complex with the hydrophobic center in the natural structure of proteins resulting in opening and deterioration of the three-dimensional structure of the protein. The decrease in activity after treatment with detergent is due to partial denaturation of bacteriocin or deterioration of its association with other molecules effective for stabilization of activity [35]. It was found that the BLIS activity of EDTA increased with increasing concentrations. However, the activity of bacteriocin incubated with EDTA and urea was completely lost [33]. EDTA can increase the antibacterial activity of bacteriocin by complex formation. It can damage the cell membrane and facilitate the antimicrobial effect of bacteriocin [57].

The antibacterial activity of BLIS was completely destroyed by proteinase K. Treatments with trypsin resulted in a reduction in activity of up to 76%. These results indicate that the antibacterial substance in the supernatant is a protein or peptide. It was concluded that the antimicrobial substance was a BLIS. It has been reported that protein-based bacteriocins are unable to stabilize and lose their antimicrobial activity after proteolytic enzyme treatment [58]. Many researchers have found that enterocins are sensitive to one or more proteolytic enzymes [59]. These results confirm that this bacteriocin has a proteinaceous structure and are consistent with this literature [36,60].

The best activity of the crude BLIS was obtained at 40% saturation in ammonium sulfate precipitate. Thuricin 439 was best obtained at 80% saturation [61]. In the activity study, a single inhibitory zone corresponding to about 15 kDa was found and this peptide was classified as an intermediate size (10-30 kDa) peptide. In a study by Tumbariski et al. [62], a peptide of approximately 19 kDa was reported as an intermediate size peptide. The molecular weight of the bacteriocin synthesized by *B. thuringiensis* entomocidus HD9 which is active against Gram (-), Gram (+) and some fungi was reported to be 12.4 kDa [7]. Polyfermenticin SCD obtained from a commercial probiotic strain of *B. polyfermenticus* has been reported to have a molecular weight of about 14.3 kDa [47]. Some other bacteriocins, produced by strains of the *Bacillus* genus, cerein [51], and thuricin 7 [63] have molecular weights of 11.6 and 9 kDa, respectively. The molecular weight of the bacteriocin obtained from *Bacillus subtilis* R75 was found to be 12 kDa [64].

Here we reported the biochemical characterization and partial purification of BLIS from *Bacillus* sp. T68. This BLIS showed stability over a wide range of pH values (5-10), and at heat and solvent treatments. Additionally, it was found sensitive to proteinase K, trypsin, SDS and triton X-100, and was generally unaffected by EDTA, and organic solvents. BLIS has a molecular weight of about 15 kDa.

CONFLICT OF INTEREST

The authors stated that there are no conflicts of interest regarding the publication of this article.

AUTHORSHIP CONTRIBUTIONS

Concept: H.K., Desing: H.K., S.K.Ş., Execution: S.K.Ş., Material supplying: H.K., Data acquisition: S.K.Ş., Data analysis/interpretation: H.K., S.K.Ş., Writing: H.K., S.K.Ş., Critical review: H.K., S.K.Ş.

REFERENCES

- [1] Hurst A. Microbial antagonism in foods. Can Inst Food Sci Technol J 1973; 6: 80-90.
- [2] Hill C. Bacteriocins: Natural Antimicrobials from Microorganisms: New Methods for Food Preservation. Blackie Academic and Professional, London, 1995.
- [3] Gratia A. Sur un remarquable exemple d'antagonisme entre deux souches de colibacille (On a remarquable example of antagonism between two stocks of colibacillus). C R Socbiol 1925; 93: 1040-1042.
- [4] Xin B, Xu H, Liu H, Liu S, Wang J, Xue J, Zhang F, Deng S, Zeng H, Zeng X, et al. Identification and characterization of a novel circular bacteriocin, bacicyclicin XIN-1, from *Bacillus* sp. *Xin1*. Food Control 2021; 121: 107696.
- [5] Islam R, Hossain MN, Alam MK, Uddin ME, Rony MH, Imran MAS, Alam MF. Antibacterial activity of lactic acid bacteria and extraction of bacteriocin protein. Adv Biosci Biotechnol 2020; 11(2): 49-59.
- [6] O'Connor PM, Kuniyoshi TM, Oliveira RP, Hill C, Ross RP, Cotter PD. Antimicrobials for food and feed; a bacteriocin perspective. Curr Opin Biotechnol 2020; 61: 160-167.

- [7] Cherif A, Chehimi S, Limem F, Hansen BM, Hendriksen NB, Daffonchio D, Boudabous A. Detection and characterization of the novel bacteriocin entomocin 9, and safety evaluation of its producer, *Bacillus thuringiensis* subsp. *entomocidus* HD9. *J Appl Microbiol* 2003; 95:990-1000.
- [8] Ennahar S, Sashihara T, Sonomoto K, Ishizaki A. Class Iia bacteriocin biosynthesis, structure and activity. *FEMS Microbiol Rev* 2000; 24: 85-106.
- [9] Garneau S, Martin NI, Vederas JC. Two peptide bacteriocins produced by lactic acid bacteria. *J Biochem* 2002; 84: 577-592.
- [10] Cotter PD, Hill C, Ross RP. Bacteriocins: Developing innate immunity for food. *Nat Rev Microbiol* 2005; 3: 777-788.
- [11] Barberis S, Quiroga HG, Barcia C, Talia JM, Debattista N. Natural food preservatives against microorganisms. In *Food Safety and Preservation 2018*; 621-658. Academic Press.
- [12] Delesa DA. Bacteriocin as an advanced technology in food industry. *Int J Adv Res Biol Sci* 2017; 4(12): 178-190.
- [13] Johnson MEM, Jung YG, Jin YY, Jayabalan R, Yang SH, Suh JW. Bacteriocins as food preservatives: Challenges and emerging horizons. *Crit Rev Food Sci Nutr* 2017; 58: 2743-2767.
- [14] Des F, Ross RP, Hill C. Developing bacteriocins of lactic acid bacteria into next generation biopreservatives. *Curr Opin Food Sci* 2018; 20: 1-6.
- [15] Draper LA, Cotter PD, Hill C, Ross RP. Lantibiotic resistance. *Microbiol Mol Biol Rev* 2015; 79(2): 171-191.
- [16] Garg N, Tang W, Goto Y, Nair SK, van der Donk WA. Lantibiotics from *Geobacillus thermodenitrificans*. *Proc Natl Acad Sci USA* 2012; 109: 5241-5246.
- [17] Rollema HS, Kuipers OP, Both P, de Vos WM, Siezen RJ. Improvement of solubility and stability of the antimicrobial peptide nisin by protein engineering. *Appl Environ Microbiol* 1995; 61: 2873-2878.
- [18] Zhou H, Fang J, Tian Y, Lu X. Mechanisms of nisin resistance in Gram-positive bacteria. *Ann Microbiol* 2014; 64: 413-420.
- [19] Jack RW, Tagg JR, Ray B. Bacteriocins of Gram-positive bacteria. *Microbiol Rev* 1995; 59: 171-200.
- [20] Cordovilla P, Valdivia E, Gonzalez-Sequra A, Galvez A, Martinez-Bueno M, Maqueda M. Antagonistic action of the bacterium *Bacillus licheniformis* M-4 toward the amoeba *Naegleria fowleri*. *J Eukaryot Microbiol* 1993; 40: 323-328.
- [21] Nicholson WL. Roles of *Bacillus* endospores in the environment. *Cell Mol Life Sci* 2002; 59: 410-416.
- [22] Stein T. *Bacillus subtilis* antibiotics: structures, syntheses and specific functions. *Mol Microbiol* 2005; 56: 845-857.

- [23] Abriouel H, Franz CM, Ben Omar N, Gálvez A. Diversity and applications of *Bacillus thuringiensis*. FEMS Microbiol Rev 2011; 35: 201-232.
- [24] Paik HD, Bae SS, Pan JG. Identification and partial characterization of tochicin, a bacteriocin produced by *Bacillus thuringiensis* subsp. *tochigiensis*. J Ind Microbiol Biotechnol 1997; 19: 294-298.
- [25] Ehling-Schulz M, Lereclus D, Koehler TM. The *Bacillus cereus* group: *Bacillus* species with pathogenic potential. Microbiol Spectr 2019; 7(3): 1-60.
- [26] Xin B, Liu H, Zheng J, Xie C, Gao, Y, Dai D, Peng D, Ruan L, Chen H, Sun M. *In Silico* analysis highlights the diversity and novelty of circular bacteriocins in sequenced microbial genomes. Appl Environ Sci 2020; 5(3): e00047-20.
- [27] Huo L, van der Donk WA. Discovery and characterization of bicereucin, an unusual d-amino acid-containing mixed two-component lantibiotic. J Am Chem Soc 2016; 138(16): 5254-5257.
- [28] Mo T, Ji X, Yuan W, Mandalapu D, Wang F, Zhong Y, Li F, Chen Q, Ding W, Deng Z, et al. Thuricin Z: A narrow-spectrum sactibiotic that targets the cell membrane. Angew Chem Int Ed 2019; 58(52): 18793-18797.
- [29] Xin B, Zheng J, Liu H, Li J, Ruan L, Peng D, Sajid M, Sun M. Thusin, a novel two-component lantibiotic with potent antimicrobial activity against several Gram-positive pathogens. Front Microbiol 2016; 7: 1115.
- [30] Katı H, Karaca B, Gülşen ŞH. Topraktan izole edilen *Bacillus* türlerinin tanımlanması ve biyolojik özelliklerinin araştırılması. SAÜ Fen Bil Der 2016; 20(2): 281-290.
- [31] Sensoy Karaoglu S, Sevim A, Sevim E. Production and characterization of bacteriocin-like peptide produced by *Bacillus amyloliquefaciens* B10. ERÜ Fen Bil Ens Der 2014; 30(5): 338-345.
- [32] Touraki M, Frydas I, Karamanlıdou G, Mamara A. Partial purification and characterization of a bacteriocin produced by *Bacillus subtilis* NCIMB 3610 that exhibits antimicrobial activity against fish pathogens. J Biol Res-Thessalon 2012; 18: 310-319.
- [33] Rajaram G, Manivasagan P, Thilagavathi B, Saravanakumar A. Purification and Characterization of a Bacteriocin Produced by *Lactobacillus lactis* Isolated from Marine Environment. Adv J Food Sci Technol 2010; 2(2): 138-144.
- [34] Rasheed HA, Tuoheti T, Zhang Y, Azi F, Tekliye M, Dong M. Purification and partial characterization of a novel bacteriocin produced by bacteriocinogenic *Lactobacillus fermentum* BZ532 isolated from Chinese fermented cereal beverage (Bozai). LWT - Food Sci Technol 2020; 124: 109113.
- [35] Ivanova I, Miteva V, Stefanova Ts, Pantev A, Budakov I, Danova S, Moncheva P, Nikolova I, Dousset X, Boyaval P. Characterization of a bacteriocin produced by *Streptococcus thermophilus* 81. Int J Food Microbiol 1998; 42: 147-158.
- [36] Bizani D, Brandelli A. Characterization of a bacteriocin produced by a newly isolated *Bacillus* sp. strain 8A. J Appl Microbiol 2002; 93: 512-519.

- [37] He L, Chen W, Liu Y. Production and partial characterization of bacteriocin-like peptides by *Bacillus licheniformis* ZJU12. *Microbiol Res* 2006; 161: 321-326.
- [38] Laemmli UK. Cleavages of structural proteins during the assembly of the head of bacteriophage T4. *Nature* 1970; 227: 680-685.
- [39] Lim KB, Balolong MP, Kim SH, Oh JK, Lee JY, Kang DK. Isolation and characterization of a broad spectrum bacteriocin from *Bacillus amyloliquefaciens* RX7. *BioMed Res Int* 2016; 1-7.
- [40] Gebhardt K, Schimana J, Muller J. Screening for biologically active metabolites with endosymbiotic bacilli isolated from arthropods. *FEMS Microbiol Lett* 2002; 217: 199-205.
- [41] Stein T, Heinzmann S, Dusterhus S, Borchert S, Entian KD. Expression and functional analysis of the subtilin immunity genes *spaIFEG* in the subtilin sensitive host *Bacillus subtilis* MO1099. *J Bacteriol* 2005; 187: 822-828.
- [42] Lucas R, Grande MA, Abriouel H, Maqueda M, Ben Omar N, Valdivia E, Martinez-Canamero M, Galvez A. Application of the broad-spectrum bacteriocin enterocin AS-48 to inhibit *Bacillus coagulans* in canned fruit and vegetable foods. *Food Chem Toxicol* 2006; 44: 1774-1781.
- [43] Lisboa MP, Bonatto D, Bizani D, Henriques JAP, Brandelli A. Characterization of a bacteriocin-like substance produced by '*Bacillus amyloliquefaciens*' isolated from the Brazilian Atlantic forest. *Int Microbiol* 2006; 9: 111-118.
- [44] Benitez LB, Caumo K, Brandalli A, Rott MB. Bacteriocin-like substance from *Bacillus amyloliquefaciens* shows remarkable inhibition of *Acanthamoeba polyphaga*. *Parasitol Res* 2011; 108: 687-669.
- [45] Campos CA, Rodriguez O, Mata PC, Prado M, Velazquez JB. Preliminary characterization of bacteriocins from *Lactococcus lactis*, *Enterococcus faecium* and *Enterococcus mundtii* strains isolated from turbot (Psetta Maxima). *Food Res Int* 2008; 7: 432-441.
- [46] Cherif A, Rezgui W, Raddadi N, Daffonchio D, Boudabous A. Characterization and partial purification of entomocin 110, a newly identified bacteriocin from *Bacillus thuringiensis* subsp. *entomocidus* HD110. *Microbiol Res* 2008; 163: 684-692.
- [47] Lee K H, Jun K D, Kim W S, Paik H D. Partial characterization of polyfermentacin SCD, a newly identified bacteriocin of *Bacillus polyfermenticus*. *Lett Appl Microbiol* 2001; 32: 146-151.
- [48] Bizani D, Dominguez A, Brandelli A. Purification and partial chemical characterization of the antimicrobial peptide cerein 8A. *Lett Appl Microbiol* 2005; 41(3): 269-273.
- [49] Valdes-Stauber N, Scherer S. Isolation and characterization of Linocin M18, a bacteriocin produced by *Breibacterium linens*. *Appl Environ Microbiol* 1994; 60: 3809-3814.
- [50] Kamoun F, Mejdoub H, Aouissaoui H, Reinbolt J, Hammami A, Jaoua S. Purification, amino acid sequence and characterization of Bacthuricin F4, a new bacteriocin produced by *Bacillus thuringiensis*. *J Appl Microbiol* 2005; 98: 881-888.

- [51] Naclerio G, Ricca E, Sacco M, De Felice, M. Antimicrobial activity of a newly Identified bacteriocin of *Bacillus cereus* with a broad spectrum of activity. FEMS Microbiol Lett 1993; 178: 337-341.
- [52] Yang R, Ray B. Factors influencing production of bacteriocins by lactic acid bacteria. Food Microbiol 1994; 11: 281-291.
- [53] Yıldırım Z, Johnson MG. Detection and characterization of a bacteriocin produced by *Lactococcus lactis* subsp. *cremoris* R isolated from radish. Lett Appl Microbiol 1998; 26: 297-304.
- [54] Lee NK, Paik HD. Partial characterization of lacticin NK24, a newly identified bacteriocin of *Lactococcus lactis* NK24 isolated from jeot-gal. Food Microbiol 2001; 18: 17-24.
- [55] Asutay D. Yöresel bir gıdadan izole edilen bakteriyosin üreten bakterinin teşhisi ve bakteriyosinin karakterizasyonu. Yüksek Lisans Tezi, Gaziosmanpaşa Üniversitesi, Tokat, Türkiye, 2007.
- [56] Pirzada ZA, Syed AA, Khan BM, Rasool SA. Production and physico-chemical characterization of bacteriocins-like inhibitory substances from marine bacterium ZM81. Pak J Biol Sci 2004; 7(12): 2026-2030.
- [57] Vaara M. Agents that increase the permeability of the outer membrane. Microbiol Rev 1992; 56: 395-411.
- [58] Ogunbanwo ST, Sanni AI, Onilude AA. Characterization of bacteriocin produced by *Lactobacillus plantarum* F1 and *Lactobacillus brevis* OG1. J Biotechnol 2003; 8: 179-184.
- [59] Herranz C, Casaus P, Mukhopadhyay S, Martinez JM, Rodriguez JM, Nes IF, Hernández PE, Cintas LM. *Enterococcus faecium* P21: a strain occurring naturally in dry-fermented sausages producing the class II bacteriocins enterocin A and enterocin B. Food Microbiol 2001; 18(2): 115-131.
- [60] Florencia CA, Caron GR, Adriano B. Bacteriocin-like substance production by *Bacillus licheniformis* strain P40. Lett Appl Microbiol 2004; 38 (4): 251-256.
- [61] Ahern M, Verschuere S, Sinderen DV. Isolation and characterisation of a novel bacteriocin produced by *Bacillus thuringiensis* strain B439. FEMS Microbiol Lett 2003; 220: 127-131.
- [62] Tumbarski Y, Deseva I, Mihaylova D, Stoyanova M, Krastev L, Nikolova R, Yanakieva V, Ivanov I. Isolation, Characterization and Amino Acid Composition of a Bacteriocin Produced by *Bacillus methylotrophicus* Strain BM47. Food Technol Biotechnol 2018; 56(4): 546-552.
- [63] Cherif A, Ouzari H, Daffonchio D, Cherif H, Ben Slama K, Hassen A, Jaoua S, Boudabous A. Thuricin 7: a novel bacteriocin produced by *Bacillus thuringiensis* BMG1.7, a new strain isolated from soil. Lett Appl Microbiol 2001; 32: 243-247.
- [64] Sharma N, Kapoor R, Gautam N, Kumari R. Purification and characterization of bacteriocin produced by *Bacillus subtilis* R75 isolated from fermented chunks of mung bean (*Phaseolus radiatus*). Food Technol Biotechnol 2011; 49 (2): 169-176.



RESEARCH ARTICLE

PHOTOLUMINESCENCE PROPERTIES OF Nd³⁺, Yb³⁺ CODOPED Ga₂O₃
NANOPARTICLES

Ayşe DULDA * 

Department of Material Science and Nanotechnology Engineering, Engineering Faculty, Yeditepe University, İstanbul, Turkey

ABSTRACT

The availability of sensitive photon detectors and inexpensive lasers allowed us to explore more efficient fluorescent probes that will work in second near-infrared optical window. In this study, the optical properties of Nd³⁺ and Yb³⁺ co-doped Ga₂O₃ nanoparticles were studied. In order to indicate the correlation between particle size, crystallinity and optical property of present samples XRD, TEM, and Photoluminescence analyses were performed. Various excitation wavelengths and dopant concentrations were used to understand the energy transfer mechanism in Nd³⁺ and Yb³⁺ co-doped Ga₂O₃ nanoparticles. As the excitation wavelength increased from 325 nm to 477 and 515 nm, Yb³⁺ emission peak intensity decreased while Nd³⁺ emission peak intensity increased. This inverse relationship between the emission intensities of Yb³⁺ and Nd³⁺ ion showed the presence of energy transfer between them. Resulting emission peaks were broad and weak, indicating the presence of a non-radiative decay channel due to the crystal defects.

Keywords: Energy Transfer, Gallium Oxide, Nd³⁺, Yb³⁺, Near Infrared Emission, Luminescence

1. INTRODUCTION

One of the most important issue that researchers work on is the ability of monitoring biological structures and their functioning at the molecular level. Among the other bioimaging techniques fluorescence microscopy offers a unique approach for visualizing morphological details in tissue with subcellular resolution [1,2] In recent decades, upconversion nanoparticles (UCNPs) frequently preferred over other commercial fluorescent probes such as quantum dots, metal complexes and dye molecules because of many advantages [3] . These UCNPs composed of rare earths that emit radiations from visible (400–700 nm) to near-infrared (NIR-I, 750–900 nm) regions of the electromagnetic spectrum. However, the limited penetration depth of light in tissue (1–2 mm) leads to extension of biological window to 1000–1700 nm (NIR-II window)[4–9] . In addition, the advances in optoelectronic technology such as fabrication of sensitive cameras (InGaAs and HgCdTe cameras), fiber optics, and diode lasers have allowed us to shift our working area to the second near-infrared window [4]Lim et al. have reported that 1000-fold improvement in fluorescence imaging quality in the NIR-II window [10].

Diao, S. et al. have shown that auto-fluorescence free emission over 1500 nm (NIR-II window) [11]. Wang et al. have developed a fluorescent probe emitting at 1525 nm that achieves high penetration depth (18 mm), even detectable with a low concentration of 5 nM [12]. Those are the extrinsic effects influencing penetration depth as a result of light interaction with tissue (absorbance, scattering and autofluorescence). Intrinsic properties of fluorescence probe (host materials and defects) are also important for prob efficiency, hence image quality.

In our previous study, over thousand nanometer emission from Nd³⁺ and Yb³⁺ co-doped Ga₂O₃ nanoparticles reported under NIR excitations. Nd³⁺ and Yb³⁺ were selected as dopants as the transitions between (Nd³⁺: ⁴F_{3/2}→⁴I_{9/2}) and (Yb³⁺: ²F_{7/2}→²F_{5/2}) energy levels highly overlap for efficient energy transfer [13,14]. Here excitations in the visible range is studied to understand the effect of defects on the energy transfer mechanism and the optical property of present sample. To the best of our knowledge, although there are many lanthanides doped Ga₂O₃ have been reported in literature, this study will be the first investigating energy transfer in Nd³⁺ and Yb³⁺ co-doped Ga₂O₃ system.

2. MATERIALS and METHODS

2.1. Chemicals

GaCl₃ (ultra dry 99,999% Abcr), YbCl₃ (Ytterbium(III) chloride anhydrous, -10 mesh, 99.99%, Sigma Aldrich), NdCl₃ (Neodymium(III) chloride hexahydrate (99.9% trace metals basis, Sigma Aldrich), oleic acid (97%, ACROS Organics), sodium oleate(≥82% fatty acids (as oleic acid) basis, Sigma Aldrich) and 1-Octadecene (90%, tech., ACROS Organics) were used without further purification, n-hexane, ethanol.

2.2. Procedure

2.2.1. Synthesis of metal-oleate complex

Yb³⁺ and Nd³⁺ codoped Ga₂O₃ nanocrystals were prepared by thermal decomposition method[15]. In a typical synthesis, 10 mmol metal chlorides (%99,4 or %99,5 GaCl₃, %0,4, or %0,5 YbCl₃, %0,1 NdCl₃) and sodium oleate (20 mmol) were dissolved in a mixture of solvents of ethanol (10 mmol), hexane (17,5 mmol) and deionised water (7,5 mmol) by stirring in a heating mantle. This mixture heated to 60°C and kept at this temperature for 4 hours in inert atmosphere. The resulting solution was in two phase. Upper organic phase containing metal oleate complex was separated via separating funnel and the metal oleate complex washed several times. The resulting waxy solution was left in an oven at 100°C to allow the remaining solvent (hexane and water) to be completely evaporated off.

2.2.2. Synthesis of Nd³⁺, Yb³⁺ doped Ga₂O₃ nanoparticles

The final organic complex (2 mmol metal oleate) was heated to 320 °C in a mixture of 10 g octadecene and 1mmol oleic acid with a heating rate of 2 °C/min. and then maintained for one hour at this temperature. When the reaction is completed resulting particles were washed with hexane and ethanol to separate organics from nanoparticles through centrifugation.

2.3. Instrumentations

The crystalline phases of the samples were determined by powder X-Ray Diffraction method using a Bruker D8 Advance X-ray diffractometer with CuK α radiation. The scan rate of 2 θ /min was set over the range of 10 – 70°. The morphological characterization of the samples was monitored using transmission electron microscopy (FE-TEM, 200 kV, Tecnai F20). Samples were prepared for TEM investigations by putting an aliquot of n-hexane solution of nanoparticles onto an amorphous carbon substrate supported on a copper grid. X-ray diffraction analyses were carried out using Micro-area X-ray diffractometer (Rigaku, D/MAX-2500). The room temperature photoluminescence (PL) spectrum of the powder samples was measured using a grating monochromator and a thermo-electrically cooled InGaAs photodiodes for the IR region employing the standard lock-in technique. The 325 nm line of a He-Cd laser (10 mW) and the 477 and 515 nm lines of an Ar laser (200 mW) were used as excitation sources. All spectrum results were corrected for the system response.

3. RESULTS and DISCUSSIONS

3.1. Morphology and Crystallinity

The crystalline structures and phase purities of $\text{Ga}_2\text{O}_3:\text{Yb}^{3+}, \text{Nd}^{3+}$ sample prepared through the thermal decomposition method is examined by XRD. Figure 1 shows the XRD pattern of $\text{Ga}_2\text{O}_3:\text{Nd}_{0,1}, \text{Yb}_{0,5}$ nanoparticles. The diffraction peaks agree with the XRD pattern of Gallium oxide registered in JCPDS card No: 43-1011 with a monoclinic crystal structure in the space group $c2/m$ and lattice parameters are $a = 12.23 \text{ \AA}$, $b = 3.04 \text{ \AA}$, $c = 5.80 \text{ \AA}$ and $\beta = 103.7^\circ$ [16]. The resulting peaks are sharp, indicating the high crystallinity of the present sample. Since a small amount of lanthanide ion is added, it does not cause any peak shifts or an additional peak in the spectrum.

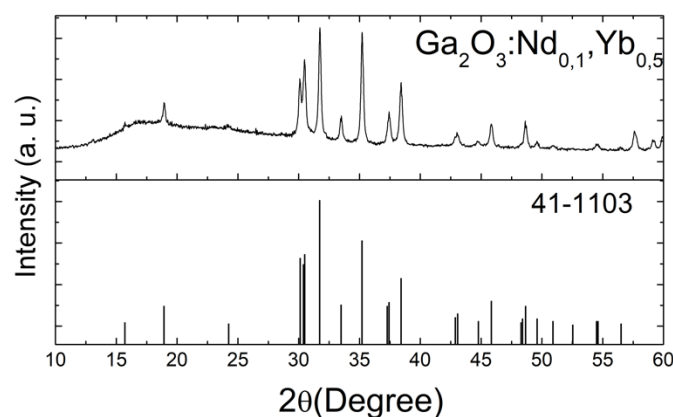


Figure 1. XRD pattern of $\text{Ga}_2\text{O}_3:\text{Nd}_{0,1}, \text{Yb}_{0,5}$ nanoparticles

Figure 2 shows the TEM image of $\text{Ga}_2\text{O}_3:\text{Yb}^{3+}, \text{Nd}^{3+}$ nanoparticles. The prepared nanoparticles present spherical morphology and their size distribution is uniform with an average diameter of $\sim 100\text{-}500 \text{ nm}$.

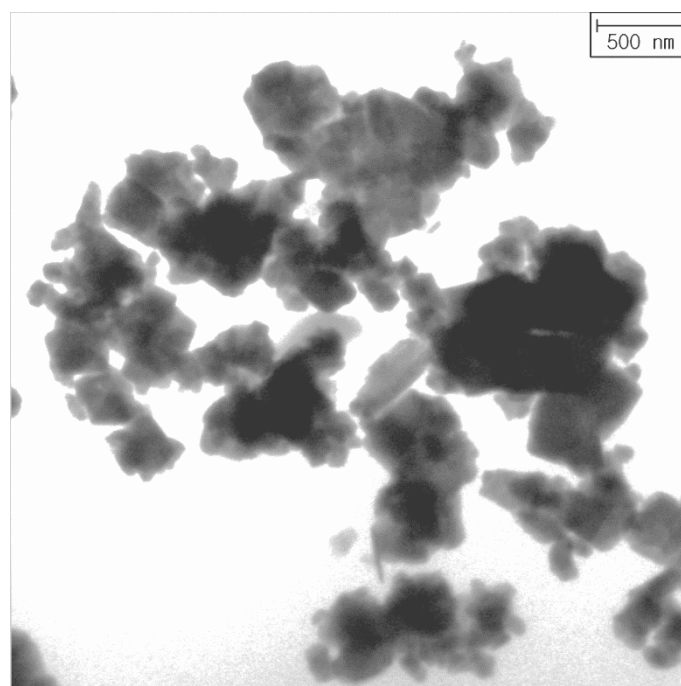


Figure 2. TEM image of $\text{Ga}_2\text{O}_3:\text{Nd}_{0,1}, \text{Yb}_{0,5}$ nanoparticles

3.2. Photoluminescence Properties of Ga₂O₃:Yb³⁺, Nd³⁺ Nanoparticles

The room temperature photoluminescence emission spectrum of Ga₂O₃:Yb³⁺, Nd³⁺ nanoparticles in the infrared region (900 -1400 nm) is shown in Figure 3. The 325 nm line of the He-Cd laser (10 mW) is used for sample excitation. PL emission spectrum consist of emission bands centered at 968 and 1070 nm. The band located at 968 nm has been associated with the ²F_{5/2}→²F_{7/2} transition of Yb³⁺ ion, while the second emission band located at 1070 nm can be attributed to ⁴F_{3/2}→⁴I_{9/2} transition of Nd³⁺ ion. It should be noticed that no clear emission is observed below ~900 nm due to the low sensitivity of the detector. Concentration of Nd³⁺ is fixed to 0,1 mol% and concentration of Yb³⁺ is varied from 0,4 to 0,5 mol% to understand energy transfer between Nd³⁺ and Yb³⁺ ions in the Ga₂O₃ samples. As Yb³⁺ ion concentration is increased, average distance between Yb³⁺ and Nd³⁺ ions is decreased. Therefore, it is expected that Yb³⁺ emission relative to Nd³⁺ should be increased due to an increase in energy transfer or the probability of cross relaxations [17,18]. However, the lower emission intensity of Yb³⁺ at 968 nm can be attributed to low energy transfer efficiency of Ga₂O₃ host crystal or back energy transfer [18].

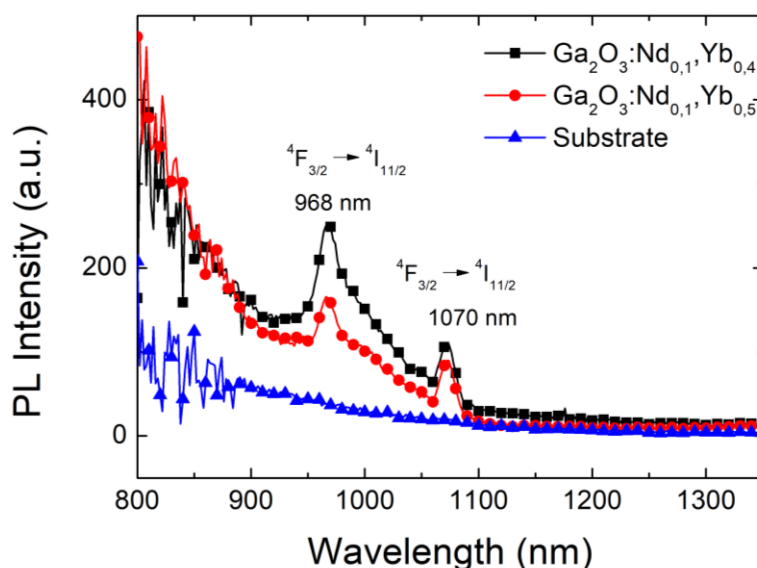


Figure 3. Photoluminescence emission spectrum of Ga₂O₃:Yb³⁺, Nd³⁺ nanoparticles under 325 nm excitation

Figure 4 shows emission spectrum of Ga₂O₃:Yb³⁺, Nd³⁺ nanoparticles under 477 nm wavelength laser excitation (~200 mW). Weak infrared emission bands are observed at 826, 876 nm (Nd³⁺: ⁴F_{3/2}→⁴I_{9/2}), 968 nm (Yb³⁺:²F_{5/2}→²F_{7/2}), 1070 nm (Nd³⁺: ⁴F_{3/2}→⁴I_{11/2}) and 1238, 1336 nm (Nd³⁺: ⁴F_{3/2}→⁴I_{13/2}). As excitation wavelength is increased from 325 to 477 nm, Yb³⁺ emission intensity is decreased and Nd³⁺ emission intensity is increased. This emission intensity increase in Nd³⁺ can be attributed to the loss of one of the cross-relaxation channel leading to Yb³⁺ emission [13]. Besides, the peaks are weak and not sharp indicating the lower crystalline environment around the Nd³⁺ ions due to the lattice distortions that resulted from the large atomic radius difference between lanthanides (Yb, Nd) and Ga ions [14]

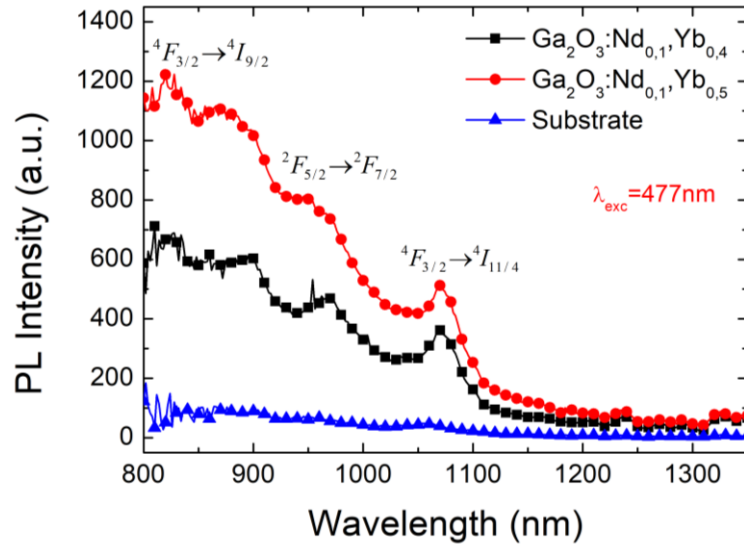
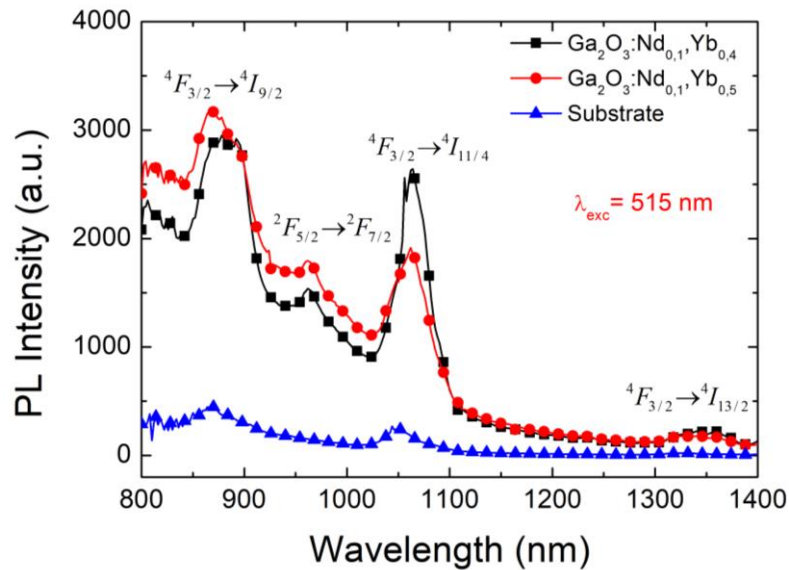


Figure 4. Photoluminescence Emission spectrum of Ga₂O₃: Nd³⁺, Yb³⁺ nanoparticles under 477 nm excitation

The PL emission spectrum of Ga₂O₃: Nd³⁺, Yb³⁺ nanoparticles under 515 nm wavelength laser excitation (~200 mW) is shown in Figure 5.



Three emission peaks observed at 868, 964 and 1070 nm corresponding to the Nd³⁺: $^4F_{3/2} \rightarrow ^4I_{9/2}$, Yb³⁺: $^2F_{5/2} \rightarrow ^2F_{7/2}$ and Nd³⁺: $^4F_{3/2} \rightarrow ^4I_{11/2}$, respectively. Multiple emission lines at 868 and 1070 nm are originated from the formation of stark sublevels due to the crystal field of Nd³⁺ ions [13,19] As the excitation wavelength is increased from 325 to 477 and 515 nm, Yb³⁺ emission peak intensity decreases while Nd³⁺ emission peak intensity increases. Also, another peak belongs to the Nd³⁺ ion at 1350 nm appears as the excitation wavelength is increased to 515 nm. This inverse relationship between the emission intensities of Yb³⁺ and Nd³⁺ ions indicates the presence of energy transfer between them [18]. Schematic representations of the energy level diagram describing possible energy transfer mechanism and transitions over the lanthanide ions in our sample is shown in Figure 6.

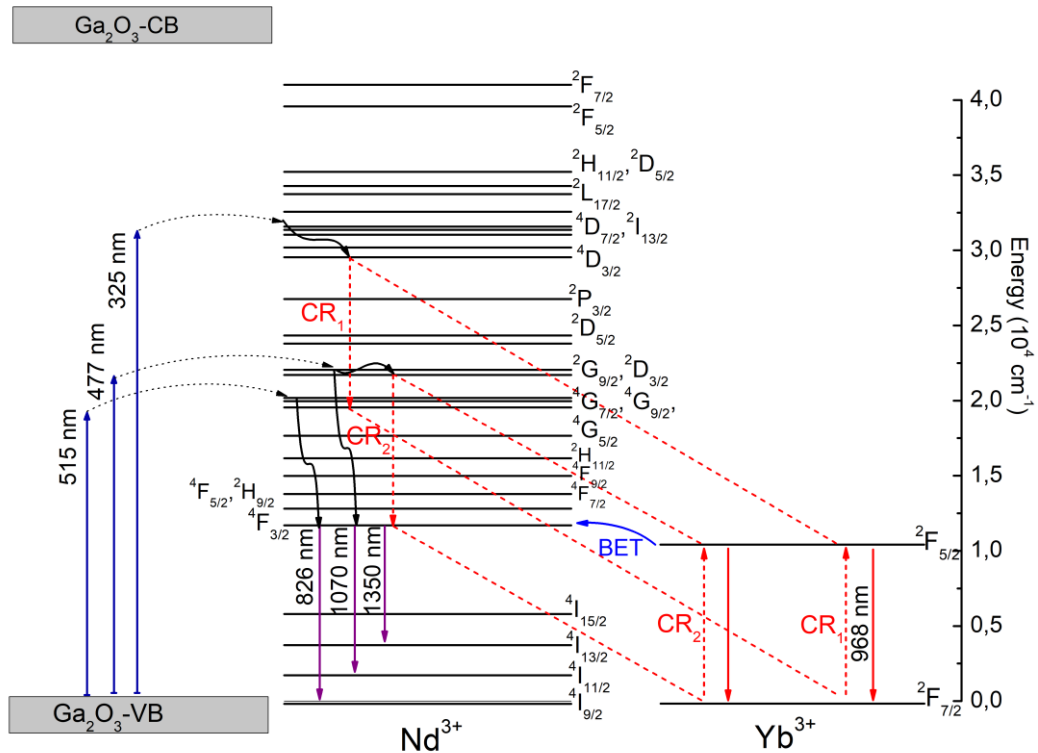


Figure 6. Schematic representations of the energy level diagram describing possible energy transfer mechanism

There are two possible ways for the excitation of lanthanide ions. The first possibility occurs via transitions throughout the electron trapped states within the band gap. The second one is the direct excitation of lanthanide ions via resonant energy transfer (Figure 6). One can find many examples in the literature explaining the energy transfer mechanisms in lanthanide-doped wide bandgap semiconductors. For example, Zhao et al. reported that excitation energy can be transferred to Eu^{3+} ions via electron traps in wide bandgap semiconductors, thereby leading to characteristic emissions of Eu^{3+} ion [20]. Bouras et al. claimed that the excitation of Nd^{3+} ions in the SnO_2 host crystal can occur either by (i) non-radiative energy transfer to the Nd^{3+} ions after band to band excitations of the SnO_2 host crystal or (ii) by electron traps within the bandgap [21]. In this study, the band gap of Ga_2O_3 is around 4,9 eV and its band to band excitation can be achieved at least with a 254 nm wavelength light source. Therefore, band to band excitation of present sample with 325 nm laser is not possible. Here, the optical property of the present samples seems to be controlled by electron traps. In general, a certain amount of oxygen vacancies are formed in semiconductor oxides depending on synthesis conditions [22–24]. These oxygen vacancies form empty energy levels below conduction band minimum (CBM), acting as electron traps. When $\text{Ga}_2\text{O}_3:\text{Nd}^{3+}, \text{Yb}^{3+}$ nanoparticles are exposed to the 325 nm laser, electrons in the valence band are excited from the ground state to these electron traps. As soon as the electrons recombine with photogenerated holes, the resulting energy is transferred to the corresponding energy level of Nd^{3+} ions [25,26]. After multiphonon relaxations between $^4\text{D}_{7/2}$ and $^4\text{D}_{3/2}$ energy levels, there are two possibilities in the energy transfer process. First, electrons might decay from $^4\text{D}_{3/2}$ to $^4\text{F}_{3/2}$ energy levels of Nd^{3+} ions non-radiatively and then produce NIR emissions at 1070 nm via transitions between $^4\text{F}_{3/2}$ and $^4\text{I}_{13/2}$ energy levels. Second, electrons might transfer their energy to Yb^{3+} ions via CR1 cross-relaxations yielding emissions at 986 nm (Figure 6). It is difficult to talk about the existence of quantum cutting process here since the phonon energy of Ga_2O_3 is more than 500 cm^{-1} [18,27]. If so, the Yb^{3+} emission intensity should be the highest for high energy excitation (325 nm). When excitation wavelength increased to 477 nm, excited electrons in the $^2\text{G}_{9/2}$ energy level relax to $^4\text{F}_{3/2}$ energy level non-radiatively through both multiphonon and cross relaxations (CR2) resulting in weak emissions at 826, 876 nm ($\text{Nd}^{3+}: ^4\text{F}_{3/2} \rightarrow ^4\text{I}_{9/2}$),

968 nm ($\text{Yb}^{3+}:^2\text{F}_{5/2} \rightarrow ^2\text{F}_{7/2}$), 1070 nm ($\text{Nd}^{3+}:^4\text{F}_{3/2} \rightarrow ^4\text{I}_{11/2}$) and 1238, 1336 nm ($\text{Nd}^{3+}:^4\text{F}_{3/2} \rightarrow ^4\text{I}_{13/2}$). But, as the energy levels are very close to each other between $^2\text{G}_{9/2}$ and $^4\text{F}_{3/2}$ levels, energy loss through the multiphonon relaxation reduces the energy transfer to Yb^{3+} ion. This may explain the reason for the decrease in Yb^{3+} emission compared to the 325 nm excitation (Figure 4). A strong Nd^{3+} and very weak Yb^{3+} emission are observed when the sample is excited with 515 nm laser irradiation. Compared to higher energy excitations (325 and 477 nm), Nd^{3+} emission intensity is the highest while Yb^{3+} emission intensity is the lowest (Figure 5). This could be originated from the loss of the CR1 and CR2 cross relaxations leading to Yb^{3+} emission. Besides, for all excitations (325, 477 and 515 nm), as Yb^{3+} concentration is increased the emission intensities of both Yb^{3+} and Nd^{3+} ions are decreased due to lattice distortions [18].

4. CONCLUSIONS

In summary, in order to understand the effects of defects (lanthanide dopants and oxygen vacancies) on the energy transfer mechanism, various excitation wavelengths and dopant concentrations experimented. As the excitation wavelength increased from 325 nm to 477 and 515 nm, Yb^{3+} emission peak intensity decreased while Nd^{3+} emission peak intensity increased. This inverse relationship between the emission intensities of Yb^{3+} and Nd^{3+} ion indicated the presence of energy transfer between them. However, it was observed that energy transfer from the host material was very weak due to lattice distortions and high phonon energies of Ga_2O_3 crystal. This result was deduced from the broad and weak emission peaks observed for each excitation wavelengths. The strongest Nd^{3+} emission was observed when the sample was resonantly pumped with 515 nm. This results indicate that Yb^{3+} and Nd^{3+} doped Ga_2O_3 can be used as imaging contrast agent for near infrared imaging applications in future.

CONFLICT OF INTEREST

The author stated that there are no conflicts of interest regarding the publication of this article.

REFERENCES

- [1] Zhou J, Liu Z, Li F. Upconversion nanophosphors for small-animal imaging. *Chem Soc Rev*, 2012;41(3):1323-1349.
- [2] Yu M, Li F, Chen Z, et al. Laser scanning up-conversion luminescence microscopy for imaging cells labeled with rare-earth nanophosphors. *Anal Chem*, 2009;81(3):930-935.
- [3] Naccache R, Rodríguez EM, Bogdan N, et al. High resolution fluorescence imaging of cancers using lanthanide ion-doped upconverting nanocrystals. *Cancers (Basel)*, 2012;4(4):1067-1105.
- [4] Hong G, Antaris AL, Dai H. Near-infrared fluorophores for biomedical imaging. *Nat Biomed Eng*, 2017;1(1):0010.
- [5] Wang C, Cheng L, Liu Z. Drug delivery with upconversion nanoparticles for multi-functional targeted cancer cell imaging and therapy. *Biomaterials*, 2011;32(4):1110-1120.
- [6] Naczynski DJ, Tan MC, Zevon M, et al. Rare-earth-doped biological composites as in vivo shortwave infrared reporters. *Nat Commun*, 2013;4(1):2199.
- [7] Smith AM, Mancini MC, Nie S. Second window for in vivo imaging. *Nat Nanotechnol*, 2009;4(11):710-711.

- [8] Hong G, Lee JC, Robinson JT, et al. Multifunctional in vivo vascular imaging using near-infrared II fluorescence. *Nat Med*, 2012;18(12):1841-1846.
- [9] Li Y, Zeng S, Hao J. Non-invasive optical guided tumor metastasis/vessel imaging by using lanthanide nanoprobe with enhanced down-shifting emission beyond 1500 nm. *ACS Nano*, 2019;13(1):248-259.
- [10] Lim YT, Kim S, Nakayama A, Stott NE, Bawendi MG, Frangioni J V. Selection of quantum dot wavelengths for biomedical assays and imaging *Mol Imaging*, 2 (1): 50–64. Find this article online. Published online 2003.
- [11] Diao S, Hong G, Antaris AL, et al. Biological imaging without autofluorescence in the second near-infrared region. *Nano Res*, 2015;8:3027-3034.
- [12] Wang R, Li X, Zhou L, Zhang F. Epitaxial seeded growth of rare-earth nanocrystals with efficient 800 nm near-infrared to 1525 nm short-wavelength infrared downconversion photoluminescence for in vivo bioimaging. *Angewandte Chemie International Edition*, 2014;53(45):12086-12090.
- [13] Talewar RA, Mahamuda S, Swapna K, Rao AS. Sensitization of Yb³⁺ by Nd³⁺ emission in alkaline-earth chloro borate glasses for laser and fiber amplifier applications. *J Alloys Compd*, 2019;771:980-986.
- [14] Lupei A, Lupei V, Ikesue A, Gheorghe C, Hau S. Nd→ Yb energy transfer in (Nd, Yb): Y₂O₃ transparent ceramics. *Opt Mater (Amst)*, 2010;32(10):1333-1336.
- [15] Park J, An K, Hwang Y, et al. Ultra-large-scale syntheses of monodisperse nanocrystals. *Nat Mater*, 2004;3(12):891-895.
- [16] Zhao J, Zhang W, Xie E, Ma Z, Zhao A, Liu Z. Structure and photoluminescence of β-Ga₂O₃: Eu³⁺ nanofibers prepared by electrospinning. *Appl Surf Sci*, 2011;257(11):4968-4972.
- [17] Xia Z, Luo Y, Guan M, Liao L. Near-infrared luminescence and energy transfer studies of LaOBr: Nd³⁺/Yb³⁺. *Opt Express*, 2012;20(105):A722-A728.
- [18] Borrero-González LJ, Nunes LA de O. Near-infrared quantum cutting through a three-step energy transfer process in Nd³⁺–Yb³⁺ co-doped fluorindogallate glasses. *Journal of Physics: Condensed Matter*, 2012;24(38):385501.
- [19] Lupei V, Lupei A, Ikesue A. Spectroscopic properties of Nd³⁺ and highly efficient Nd³⁺ to Yb³⁺ energy transfer in transparent Sc₂O₃ ceramics. In: *Advanced Solid-State Photonics*. Optica Publishing Group, 2005;41.
- [20] Jia Z, Arcangeli A, Tao X, et al. Efficient Nd³⁺→ Yb³⁺ energy transfer in Nd³⁺, Yb³⁺: Gd₃Ga₅O₁₂ multicenter garnet crystal. *J Appl Phys*, 2009;105(8):083113.
- [21] Bouras K, Rehspringer JL, Schmerber G, et al. Optical and structural properties of Nd doped SnO₂ powder fabricated by the sol–gel method. *J Mater Chem C Mater*, 2014;2(39):8235-8243.
- [22] Liu Y, Luo W, Zhu H, Chen X. Optical spectroscopy of lanthanides doped in wide band-gap semiconductor nanocrystals. *J Lumin*, 2011;131(3):415-422.
- [23] Kamiya T, Hosono H. Material characteristics and applications of transparent amorphous oxide semiconductors. *NPG Asia Mater*, 2010;2(1):15-22.

- [24] Buckeridge J, Catlow CRA, Farrow MR, et al. Deep vs shallow nature of oxygen vacancies and consequent n-type carrier concentrations in transparent conducting oxides. *Phys Rev Mater*, 2018;2(5):054604.
- [25] Wu Z, Bai G, Hu Q, et al. Effects of dopant concentration on structural and near-infrared luminescence of Nd³⁺-doped beta-Ga₂O₃ thin films. *Appl Phys Lett*, 2015;106(17):171910.
- [26] Chen Z, Wang X, Noda S, et al. Effects of dopant contents on structural, morphological and optical properties of Er doped Ga₂O₃ films. *Superlattices Microstruct*, 2016;90:207-214.
- [27] Sun J, Sun Y, Cao C, Xia Z, Du H. Near-infrared luminescence and quantum cutting mechanism in CaWO₄: Nd³⁺, Yb³⁺. *Applied Physics B*, 2013;111:367-371.



RESEARCH ARTICLE

ON THE EFFECTIVENESS OF PARAGRAPH VECTOR MODELS IN DOCUMENT
SIMILARITY ESTIMATION FOR TURKISH NEWS CATEGORIZATION

Ali YÜREKLİ * 

Department of Computer Engineering, Faculty of Engineering, Eskişehir Technical University, Eskişehir, Turkey

ABSTRACT

News categorization, which is a common application area of text classification, is the task of automatic annotation of news articles with predefined categories. In parallel with the rise of deep learning techniques in the field of machine learning, neural embedding models have been widely utilized to capture hidden relationships and similarities among textual representations of news articles. In this study, we approach the Turkish news categorization problem as an ad-hoc retrieval task and investigate the effectiveness of paragraph vector models to compute and utilize document-wise similarities of Turkish news articles. We propose an ensemble categorization approach that consists of three main stages, namely, document processing, paragraph vector learning, and document similarity estimation. Extensive experiments conducted on the TTC-3600 dataset reveal that the proposed system can reach up to 93.5% classification accuracy, which is a remarkable performance when compared to the baseline and state-of-the-art methods. Moreover, it is also shown that the Distributed Bag of Words version of Paragraph Vectors performs better than the Distributed Memory Model of Paragraph Vectors in terms of both accuracy and computational performance.

Keywords: Turkish news categorization, Text classification, Neural embeddings, Paragraph vectors, Document similarity

1. INTRODUCTION

Text classification, which is the process of assigning text documents to one or more predefined categories [1], is a challenging task in machine learning due to the unstructured nature of textual data. In addition to the mentioned amorphousness, the substantial growth of data stored as text in information systems arises the need for effective and accurate text classification techniques that automatically organize data into categories [2].

The problem of text classification finds applications in a wide variety of domains [3] such as natural language inference, sentiment analysis and question answering. One such common application area of text classification is news categorization, in which the primary goal is to associate a given news article with a predefined news category such as economy, politics, sports, or technology. In today's era of digital media, where users prefer to follow daily news through online platforms [4], the ability to automatically categorize news articles is a necessity to automate and ease the data management and business procedures.

This study focuses on Turkish news categorization and approaches the problem as an ad-hoc retrieval task. We investigate the effectiveness of learning distributed word representations to capture semantic similarities of Turkish news articles. We employ Paragraph Vectors [5] (also known as Doc2Vec in the literature) to create neural embeddings of documents, and then perform top-*k* document retrieval on those embeddings to categorize given news articles. Although Doc2Vec has been successfully utilized for feature extraction and input vector generation in several news classification approaches [6-8], the effectiveness of paragraph vector models has not been well-explored in an ad-hoc retrieval setting.

During the experimental phase of the study, we evaluate several models combining two paragraph vector architectures with ad-hoc retrieval. The experiments performed on a well-known Turkish news collection [9] show that the proposed approach can reach up to 93.5% classification accuracy, which results in more accurate predictions than the baseline benchmark methods provided by Kılınç et al. [9]. Furthermore, our results are highly close and comparable to the current state-of-the-art [6].

1.1. Contributions and Organization

In this study, we propose an ad-hoc retrieval system for the task of Turkish news categorization. In order to evaluate the effectiveness of the system, extensive experiments are conducted on a collection of Turkish news articles. The main contributions of the study can be listed as follows:

- An end-to-end news categorization approach based on paragraph vectors and top- k document retrieval is proposed.
- Different modalities of paragraph vector learning architectures are explored.
- All source code and data required to reproduce the experimental results are made publicly available for interested researchers (see Section 4.2).

The rest of the paper is organized as follows. Section 2 provides a brief theoretical background of paragraph vectors and their learning architectures. Section 3 introduces the proposed ad-hoc retrieval approach in the study. Section 4 presents the experimental work and elaborates on the results. Finally, Section 5 includes future research directions and concludes the work.

2. THEORETICAL BACKGROUND

Neural embedding models have proven to be successful on a variety of downstream natural language processing tasks, including, but not limited to, text classification [10, 11], spam filtering [12, 13], sentiment analysis [14, 15], and named entity recognition [16]. The common intuition behind these models is to extract and learn high-quality representations that are capable of capturing word similarities at a semantic level with good compositionality [17].

Word2Vec [18] is such an unsupervised neural embedding model that forms a vector mapping at the word level. Based on the hypothesis that words with similar meanings exhibit close distances [19], Word2Vec leverages this mapping to derive both syntactic and semantic similarities between words. Given a sequence of words w_1, w_2, \dots, w_T , the model maximizes the average log probability of the next words within a window size of k using the equation given in (1).

$$\frac{1}{T} \sum_{t=k}^{T-k} \log p(w_t | w_{t-k}, \dots, w_{t+k}) \quad (1)$$

Let W , U , b , and h denote the word embedding matrix, parameters of the softmax function, and the concatenation (or average) of word vectors from W , respectively. Then, Word2Vec calculates the predictions using the equations shown in (2) and (3).

$$p(w_t | w_{t-k}, \dots, w_{t+k}) = \frac{e^{y w_t}}{\sum_i e^{y_i}} \quad (2)$$

$$y = b + Uh(w_{t-k}, \dots, w_{t+k}; W) \quad (3)$$

Paragraph Vectors, introduced by Le and Mikolov [5], is an extension to Word2Vec that learns continuous distributed vector representations for any variable-length textual data (e.g., sentences, paragraphs, or documents). In addition to the word embedding matrix W in Word2Vec, Paragraph

Vectors framework also employs a paragraph embedding matrix D that contains the vector mapping of each paragraph as its columns. As a result of this notable difference, the equation in (3) is re-formulated to include paragraph embeddings as shown in (4).

$$y = b + Uh(w_{t-k}, \dots, w_{t+k}; W, D) \quad (4)$$

The training of paragraph vectors can be performed using two architectures, which are the Distributed Memory Model of Paragraph Vectors (PV-DM) and the Distributed Bag of Words version of Paragraph Vectors (PV-DBOW). Both of these architectures consider the semantics and order of words together when learning the embeddings. Therefore, paragraph vector models result in better representations than traditional Bag of Words (BOW) methods [5].

The PV-DM architecture acts as a memory that remembers missing information in the current context. The main idea behind PV-DM is to sample consecutive words from some piece of text and predict target word from these set of words that are regarded as the input. Figure 1 presents an illustration of learning paragraph vectors using PV-DM. Given a phrase (e.g., “Türkiye Büyük Millet Meclisi”), the algorithm learns to predict the target word (“meclisi”) based on the given context words (“türkiye”, “büyük”, and “millet”). This approach resembles the Continuous Bag of Words (CBOW) method in Word2Vec [18].

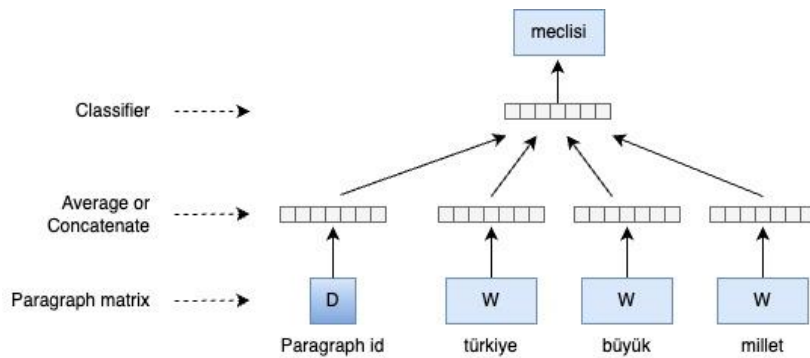


Figure 1. An illustration of learning paragraph vectors using PV-DM. The figure is derived from [5], the only difference is that the sample sentence is given in Turkish language.

On the other hand, the PV-DBOW architecture ignores the context words in the input and predicts words randomly sampled from the paragraph in the output. As illustrated in Figure 2, the output is the predictions of context words (“türkiye”, “büyük”, “millet”, and “meclisi”) for a given document indicated by a paragraph identifier. In contrast to PV-DM, PV-DBOW is inspired from the skip-gram method in Word2Vec [18].

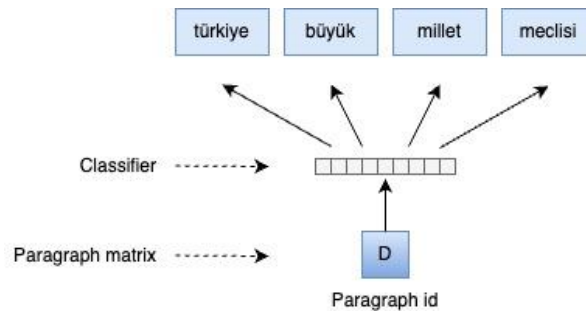


Figure 2. An illustration of learning paragraph vectors using PV-DBOW. The figure is derived from [5], the only difference is that the sample sentence is given in Turkish language.

3. PROPOSED APPROACH

Based on the idea of similar documents in content are likely to point the same point [20], we propose a semantic document similarity estimation approach for Turkish news categorization. Given a collection of news articles, a Doc2Vec model is trained using either PV-DM or PV-DBOW paragraph learning architectures. The learned embeddings are then used to capture syntactic and semantics similarities between news articles. Consequently, top- k documents retrieved for an unseen test instance constitute the news category inference for that instance.

The proposed approach consists of three main stages, which are (i) document preprocessing, (ii) paragraph vector learning, and (iii) document similarity estimation. Figure 3 illustrates the overall architecture of the proposed Turkish news categorization approach.

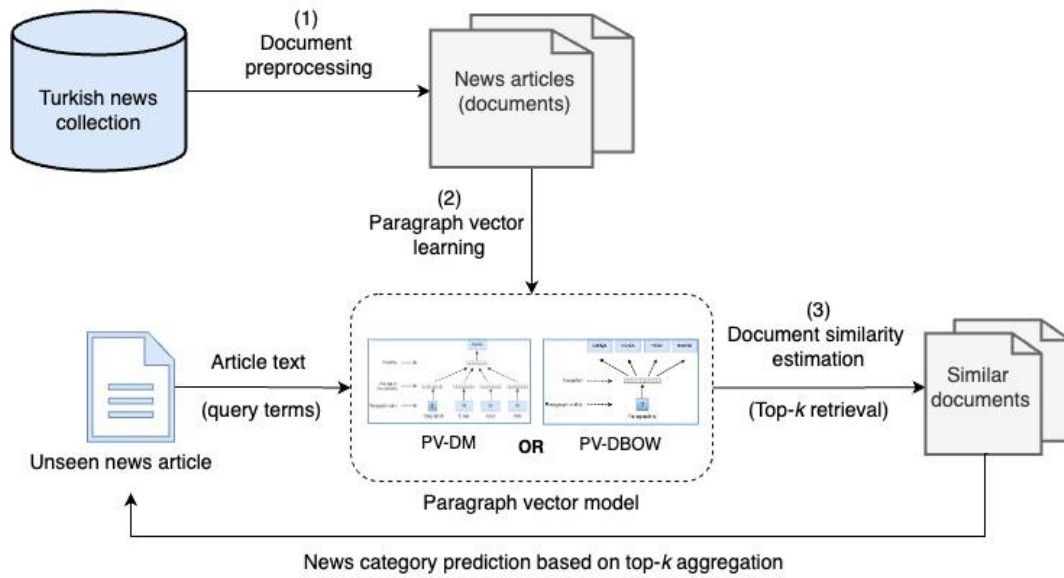


Figure 3. The overall architecture of the proposed Turkish news categorization approach.

3.1. Document Preprocessing

As practiced in the majority of text classification tasks in the literature [2], we first apply a set of well-known NLP operations on the news collection. The steps we employ for the purpose of homogenizing the data are lowercase conversion, special character (i.e., non-alphanumeric characters like whitespaces and punctuations) elimination, stemming, stop word elimination, and tokenization, respectively. Since stemming is a language-specific process, we use Zemberek-NLP¹ that is a highly favorable toolkit to perform Turkish morphological analysis.

3.2. Paragraph Vector Learning

In the prior stage, where data preprocessing is carried out, the news articles are transformed into logical document representations. The next stage of the proposed approach aims to learn paragraph embeddings of these documents via PV-DM and PV-DBOW architectures.

¹ <https://github.com/ahmetaa/zemberek-nlp>

During paragraph learning, we instantiate and train several Doc2Vec models varying with respect to notable factors such as the learning architecture and vector size. While models trained using PV-DM utilize both context word vectors and document vectors, the models based on PV-DBOW use only document vectors. Detailed information about the parameters employed at this stage can be found in Section 4.2.

When implementing the paragraph vector learning stage, we use Gensim², which is an open-source Python library designed to process unstructured text data using unsupervised machine learning algorithms.

3.3. Document Similarity Estimation

During document similarity estimation, we assess how similar two news articles are by the cosine similarity of their corresponding paragraph embeddings [21]. Suppose A and B are two paragraph vectors representing two news articles from the news collection. Then, the cosine of the angle θ between these vectors corresponds to their measure of similarity. The mathematical equation of cosine similarity between A and B is presented in (5).

$$\cos(\theta) = \frac{A \cdot B}{\|A\| \|B\|} = \frac{\sum_{i=1}^n A_i B_i}{\sqrt{\sum_{i=1}^n A_i^2} \sqrt{\sum_{i=1}^n B_i^2}} \quad (5)$$

The ability to estimate document similarities also allows us to employ top- k document retrieval for a given news article. When an unseen test instance is given to the system, the k most similar documents, both syntactically and semantically, are retrieved from the collection. Afterwards, news categorization is performed by aggregating the actual categories of the retrieved documents.

4. EXPERIMENTAL WORK

This section presents the experimental work performed during the study. First, we describe the Turkish news collection and evaluation metrics to create and evaluate classification models. Then, we explain our full-factorial setup aiming to explore the factors affecting overall performance of the proposed system. Finally, we present our results including our discussions.

4.1. Dataset and Evaluation Metrics

In this study, we use the public TTC-3600 dataset [9] to develop and evaluate models for Turkish news categorization. As its name implies, the collection consists of 3600 Turkish news articles and their corresponding categories. In the whole collection, there exist exactly 600 news articles for six major news categories, which are culture, economy, health, politics, sports, and technology. Accordingly, TTC-3600 can be considered an instance of balanced datasets.

Besides publicity and balance, there exists one more factor promoting TTC-3600 as a valuable dataset with high research potential. During the publication of the dataset, Kılınç et al. [9] had also provided a baseline presenting the performances of a set of well-known classifiers along with data preprocessing and feature selection aspects. For all these reasons, TTC-3600 has been widely used as a benchmark dataset in several studies [6, 22-25] concerning Turkish text classification.

For the purpose of training document similarity models and evaluating these models in terms of their classification performance, we split TTC-3600 into train and test sets using the stratified k-fold cross

² <https://radimrehurek.com/gensim/index.html>

validation method with $k=10$. This technique preserves the percentage of samples for each class and reduces experimental variance [26]. Consequently, for each fold, 90% of the data is used for training and the remaining 10% for testing. Table 1 shows the distribution of news categories in TTC-3600 to the train and test sets on the fold basis.

Table 1. The distribution of news categories obtained by stratified k -fold cross validation with $k=10$.

Category	Number of train instances (per fold)	Number of test instances (per fold)
Culture	540	60
Economy	540	60
Health	540	60
Politics	540	60
Sports	540	60
Technology	540	60

During the experimental evaluation phase of the study, we employ the accuracy metric to measure the classification performance of the proposed models. As given in (6), accuracy can simply be defined as the ratio of correct predictions to total predictions. It is noteworthy that Kılınç et al. [9] also uses accuracy as the primary evaluation metric in their Turkish news classification benchmark.

$$Accuracy = \frac{\text{Number of correct predictions}}{\text{Total number of predictions}} \quad (6)$$

4.2. Experimental Setup

Classification accuracy of the proposed approach depends on three main factors: (i) the training algorithm of the paragraph vectors, (ii) the dimensionality of feature vectors (i.e., vector size), and (iii) the number of documents retrieved to categorize a given news article. Table 2 presents these factors along with their notations, scope, and set of intended options.

Table 2. The factors affecting classification accuracy of the proposed approach.

Factor	Notation	Scope	Options
Paragraph vector architecture	PV	Training	PV-DM, PV-DBOW
Vector size	VS	Training	40, 80, ..., 400
Top- k documents	K	Classification	1, 2, ..., 20

As illustrated in Table 2, two of the factors affecting classification accuracy (PV and VS) are defined during the learning phase of paragraph embeddings. Therefore, tuning their corresponding options requires training of new models from scratch. However, K can be determined dynamically when classifying the test instances. In other saying, top- k document retrieval does not require any additional model training.

Since we search for the best-performing configuration of the proposed system, we follow a full-factorial experimental design that models and evaluates all possible combinations of above-mentioned factors. In total, 20 different models (i.e., 2 options for PV and 10 options for VS) are trained. Each of these models is tested with 20 choices of K varying from 1 to 20. The ranges for both K and VS values are determined empirically. Consequently, the proposed approach is subjected to 400 extensive experiments.

4.2.1. Technical details and code availability

All experiments are performed on a MacBook Pro with the M1 chip and 16GB RAM. In this environment, the final model (i.e., the best-performing configuration) can be trained and tested within less than a few minutes. The source code required to reproduce the experimental results is publicly available on GitHub³. In addition to the source code, the repository also contains a script to perform all the above-mentioned experiments from scratch.

4.3. Results and Discussions

4.3.1. Offline evaluations

In line with our experimental setup, we train and evaluate a total number of 200 distinct system configurations to explore the effectiveness of paragraph vector models over document retrieval for Turkish news categorization. Figure 4 presents the classification accuracy of all the configurations as a 3-D scatter plot, in which the x-axis represents VS , the y-axis represents K , and the z-axis represents accuracy, respectively. In addition, plus signs (+) colored in blue indicate the data points belonging to PV-DBOW models, and asterisk signs (*) colored in green show the data points belonging to PV-DM models.

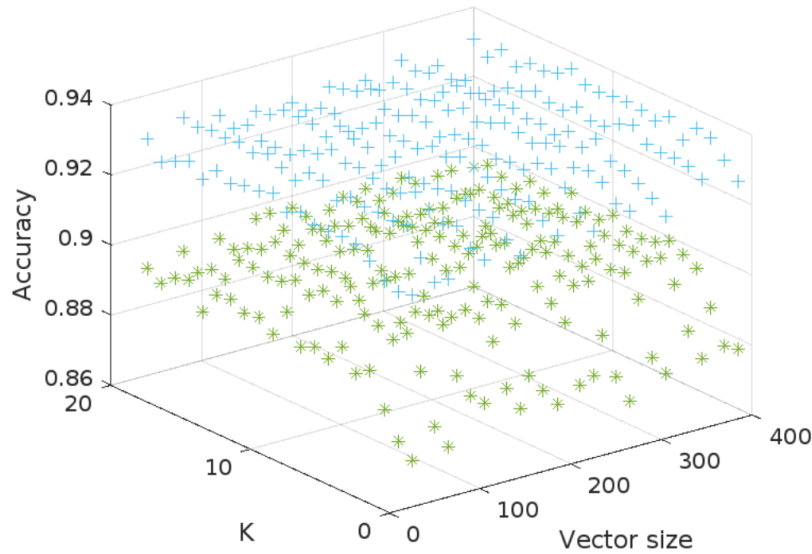


Figure 4. Data points showing the classification accuracies of PV-DM and PV-DBOW models regarding VS and K .

As illustrated in Figure 4, the data points of PV-DBOW models are located substantially higher on the z-axis than the data points of PV-DM models. While the accuracy of PV-DBOW models varies between 91.5% and 93.5%, the accuracy of PV-DM models is in the range of 87% to 90.5%. Accordingly, it can be concluded that PV-DBOW performs better than PV-DM in detecting similarities between Turkish news articles.

The choice of VS and K has a notable impact on news classification accuracy of the proposed approach. Particularly, the ranges in which PV-DM and PV-DBOW architectures achieve the best performance

³ <https://github.com/aliyurekli/turkish-news-categorization>

(i.e., paragraph vector learning and document retrieval) also differ from each other. PV-DBOW achieves the highest accuracy of 93.51% with $VS=360$ and $K=6$, while PV-DM reaches 90.48% with $VS=200$ and $K=12$. The optimal VS option is in the range of 200-240 for PV-DM and 360-400 for PV-DBOW. Additionally, the optimal K value to be used in determining the news category is between 8-12 for PV-DM and 4-6 for PV-DBOW. Accordingly, in our setting, PV-DBOW makes more accurate predictions by choosing from a narrow document pool with larger vector sizes, while PV-DM succeeds by accessing more documents based on smaller vector representations.

For further insights on Turkish news categorization, we examine classification accuracy of the proposed system in terms of the news categories in the TTC-3600 dataset. Using the best-performing configuration of the proposed retrieval approach (i.e., settings chosen as $PV=PV\text{-}DBOW$, $VS=360$, and $K=6$), the classification accuracy of each news category is measured. As illustrated in Figure 5, news articles belonging to “Sports” category can be predicted accurately as high as 98%. Similarly, predictions in “Health”, “Politics”, and “Culture” categories are also satisfactory (i.e., approximately 96%). On the other hand, it seems that it is more difficult to categorize “Economy” and “Technology” news correctly when compared to the other categories. The accuracies for these two categories drop down to 87% and 88%, respectively.

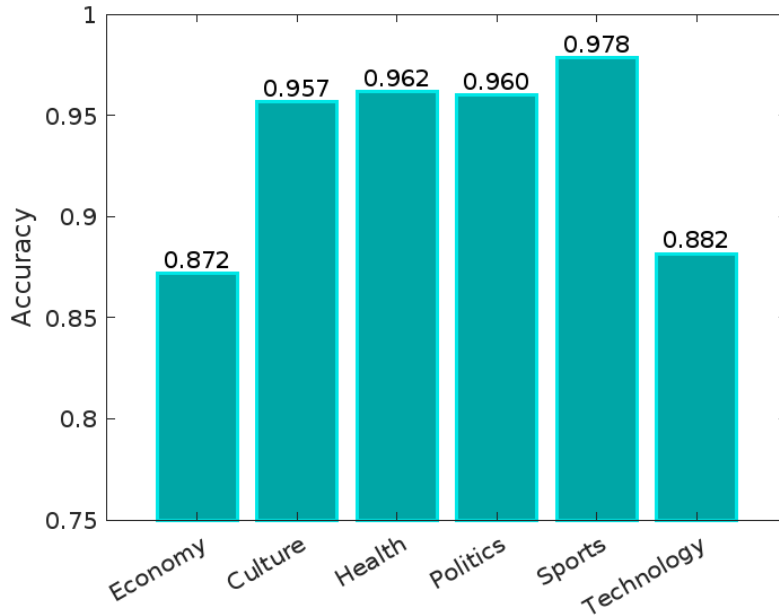


Figure 5. Classification accuracy achieved with the best-performing configuration of the system for news categories in the TTC-3600 dataset.

The accuracy analysis on the basis of news categories shows us that different categories achieve different degrees of classification performance. This observation indicates that documents from particular categories have varying characteristics in terms of semantics and structure. Nevertheless, uncovering the underlying reasons for the obvious accuracy decline in “Economy” and “Technology” might be a potential step towards overall performance improvement.

In addition to classification accuracy, we also evaluate paragraph vector learning architectures in terms of their training time. Figure 6 presents the time elapsed (in seconds) for model training according to the vector sizes varying from 40 to 400. As shown in the plot, PV-DBOW operates approximately 22% faster than PV-DM. Furthermore, as the vector size increases, the model training time for both paragraph vector learning architectures naturally increases.

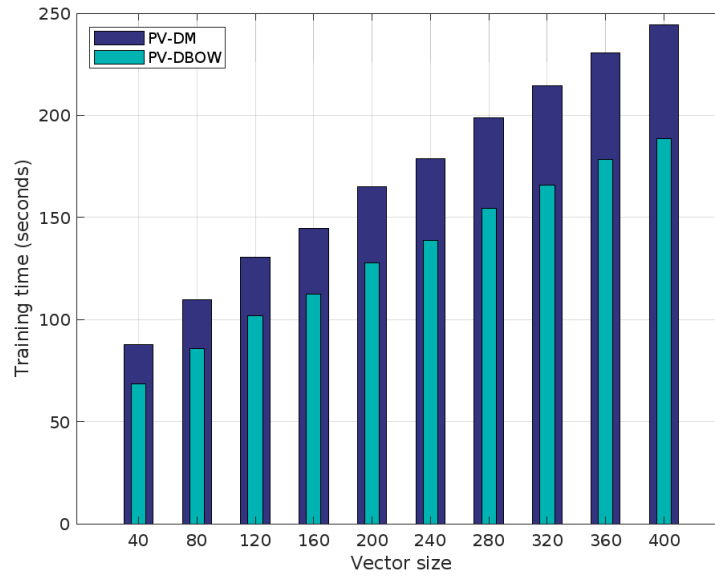


Figure 6. Comparison of paragraph vector learning algorithms in terms of training time with respect to varying vector size.

4.3.2. Comparison with the baseline and the state-of-the-art

In order to explore the effectiveness of the proposed system, we compile and compare a number of Turkish news categorization studies experimenting on the TTC-3600 dataset as the baseline and the state-of-the-art.

The baseline comprises of several classifiers evaluated in the Turkish news classification benchmark by Kılınç et al. [9]. The authors employ five well-known techniques, which are Naïve Bayes (NB), Support Vector Machine (SVM), K-Nearest Neighbor (KNN), Decision Tree (J48), and Random Forest (RF), on TTC-3600. The models have been diversified with the options of preprocessing, stemming, correlation-based feature selection (CFS), and attribute ranking-based feature selection (ARFS). In studies following this benchmark work, the state-of-the-art results have been obtained by utilizing convolutional neural networks (CNN) on neural embeddings of Doc2Vec or Word2Vec models [6, 22].

Table 3. Comparison of the proposed approach with the baseline and state-of-the-art methods.

Study		Model	Accuracy (%)
Baseline	Kılınç et al. [9]	KNN (stemming + CFS)	74.97
		J48 (stemming + ARFS)	79.39
		SVM (no stemming or feature selection)	86.03
		NB (stemming + ARFS)	87.19
		RF (stemming + ARFS)	91.03
State-of-the-art	Acı et al. [22]	CNN (Word2Vec + stemming)	93.30
	Doğru et al. [6]	CNN (Doc2Vec + stemming)	94.17
Our work		PV-DM ($VS=200, K=12$)	90.48
		PV-DBOW ($VS=360, K=6$)	93.51

Table 3 presents the classification accuracies on the TTC-3600 dataset of the approaches included in our comparison. As given in the table, our system provides better predictions than baseline methods and performs close to the state-of-the-art approaches that use CNN classifiers on Word2Vec or Doc2Vec embeddings. Therefore, the proposed model can be considered as an effective and alternative solution to the task of Turkish news categorization.

5. CONCLUSION

News categorization is a text classification task that automatically associates news articles with a predefined news category. Due to the idiosyncratic characteristics of natural languages, it is essential to develop elegant categorization techniques that take language-specific requirements and situations into consideration.

In this work, we focus on Turkish news categorization and investigate the effectiveness of paragraph vector models for document similarity estimation. The proposed approach utilizes the neural embeddings of Turkish news articles to retrieve documents with semantically and syntactically similar content. For unseen articles, the predictions are generated by aggregating category labels of top- k similar documents. The experiments performed on the TTC-3600 dataset show that our approach outperforms the baseline methods and performs highly close to the state-of-the-art. Specifically, learning paragraph vectors with PV-DBOW can reach up to 93.5% classification accuracy. On the other hand, the performance is bounded by 90.5% accuracy for the models trained with PV-DM. Our analyses also reveal that classification performance may vary based on news categories. For example, a sports news is more likely to be categorized correctly than an economy news.

In the near future, we are planning to refine the proposed system to hybridize PV-DM and PV-DBOW architectures. As emphasized by Le and Mikolov [5], the combination of these algorithms usually results in more consistent neural embeddings, which might also be a possible way to improve the overall classification accuracy of the proposed approach. Furthermore, our document similarity estimation method can be adapted for novel similarity measures [27].

ACKNOWLEDGEMENTS

The author would like to thank the editor and anonymous reviewers.

CONFLICT OF INTEREST

The author stated that there are no conflicts of interest regarding the publication of this article.

REFERENCES

- [1] Kowsari K, Jafari Meimandi K, Heidarysafa M, Mendu S, Barnes L, Brown D. Text classification algorithms: A survey. *Information*, 2019; 10(4): 150.
- [2] Uysal AK, Gunal S. The impact of preprocessing on text classification. *Information Processing & Management*, 2014; 50(1): 104-112.
- [3] Minaee S, Kalchbrenner N, Cambria E, Nikzad N, Chenaghlu M, Gao J. Deep learning-based text classification: a comprehensive review. *ACM Computing Surveys*, 2021; 54(3): 1-40.
- [4] Skogerbø E, Winsvold M. Audiences on the move? Use and assessment of local print and online newspapers. *European Journal of Communication*, 2011; 26(3): 214-229.
- [5] Le Q, Mikolov T. Distributed representations of sentences and documents. In: 31st International Conference on Machine Learning (ICML 2014); Beijing; China; 2014; pp. 1188-1196.
- [6] Dogru HB, Tilki S, Jamil A, Hamed AA. Deep learning-based classification of new texts using doc2vec model. In: 2021 1st International Conference on Artificial Intelligence and Data Analytics (CAIDA); Riyadh, Saudi Arabia; 2021; pp. 91-96.

- [7] Trieu LQ, Tran HQ, Tran MT. News classification from social media using twitter-based doc2vec model and automatic query expansion. In: Proceedings of the Eight International Symposium on Information and Communication Technology (SoICT 2017); Nha Trang, Vietnam; 2017; 460-467.
- [8] Kim D, Seo D, Cho S, Kang P. Multi-co-training for document classification using various document representations: TF-IDF, LDA, and Doc2vec. *Information Sciences*, 2019; 477: 15-29.
- [9] Kılınç D, Özçift A, Bozyigit F, Yıldırım P, Yücalar F, Borandag E. TT-3600: A new benchmark dataset for Turkish text categorization. *Journal of Information Science*, 2017; 43(2): 174-185.
- [10] Guo B, Zhang C, Liu J, Ma X. Improving text classification with weighted word embeddings via a multi-channel TextCNN model. *Neurocomputing*, 2017; 363: 366-374.
- [11] Pittaras N, Giannakopoulos G, Papadakis G, Karkaletsis V. Text classification with semantically enriched word embeddings. *Natural Language Engineering*, 2021; 27(4): 391-425.
- [12] Fahfouh A, Riffi J, Mahraz MA, Yahyaouy A, Tairi H. PV-DAE: A hybrid model for deceptive opinion spam based on neural network architectures. *Expert Systems with Applications*, 2020; 157: 113517.
- [13] Madisetty S, Desarkar MS. A neural network-based ensemble approach for spam detection in Twitter. *IEEE Transactions on Computational Social Systems*, 2018; 5(4): 973-984.
- [14] Severyn A, Moschitti A. Twitter sentiment analysis with deep convolutional neural networks. In: Proceedings of the 38th International ACM SIGIR Conference on Research and Development in Information Retrieval (SIGIR 2015); Santiago, Chile; 2015; pp. 959-962.
- [15] Tang D, Wei F, Qin B, Yang N, Liu T, Zhou M. Sentiment embeddings with applications to sentiment analysis. *IEEE Transactions on Knowledge and Data Engineering* 2015; 28(2): 496-509.
- [16] Unanue IJ, Borzeshi EJ, Piccardi M. Recurrent neural networks with specialized word embeddings for health-domain named-entity recognition. *Journal of Biomedical Informatics*, 2017; 76: 102-109.
- [17] Ai Q, Yang L, Guo J, Croft WB. Analysis of the paragraph vector model for information retrieval. In: Proceedings of the 2016 ACM International Conference on the Theory of Information Retrieval (ICTIR 2016); New York, USA; 2016. pp. 133-142.
- [18] Mikolov T, Chen K, Corrado G, Dean J. Efficient estimation of word representations in vector space. In: Proceedings of the 1st International Conference on Learning Representations (ICLR 2013); Scottsdale, Arizona, USA; 2013.
- [19] Sahlgren M. The distributional hypothesis. *Italian Journal of Disability Studies*, 2008; 20: 33-53.
- [20] Benedetti F, Beneventano D, Bergamaschi S, Simonini G. Computing inter-document similarity with context semantic analysis. *Information Systems*, 2019; 80: 136-147.

- [21] Yürekli A, Kaleli C, Bilge A. Alleviating the cold-start playlist continuation in music recommendation using latent semantic indexing. *International Journal of Multimedia Information Retrieval*, 2021; 10(3): 185-198.
- [22] Acı Ç, Çırak A. Turkish news categorization using convolutional neural networks and word2vec. *Bilişim Teknolojileri Dergisi*, 2019; 12(3): 219-228 (in Turkish with an abstract in English).
- [23] Borandağ E, Özçift A, Kaygusuz Y. Development of majority vote ensemble feature selection algorithm augmented with rank allocation to enhance Turkish text categorization. *Turkish Journal of Electrical Engineering and Computer Sciences*, 2021; 29(2): 514-530.
- [24] Cimen E. A random subspace based conic functions ensemble classifier. *Turkish Journal of Electrical Engineering and Computer Sciences*, 2020; 28(4): 2165-2182.
- [25] Wang H, Hong M. Supervised Hebb rule based feature selection for text classification. *Information Processing & Management*, 2019; 56(1): 167-191.
- [26] Forman G, Scholz M. Apples-to-apples in cross-validation studies: pitfalls in classifier performance measurement. *ACM SIGKDD Explorations Newsletter*, 2010; 12(1): 49-57.
- [27] Eminagaoglu M. A new similarity measure for vector space models in text classification and information retrieval. *Journal of Information Science*, 2022; 48(4): 463-476.



RESEARCH ARTICLE

MODELING OF CO₂ EMISSION STATISTICS in TURKEY BY FUZZY TIME SERIES ANALYSIS

Fatih ÇEMREK¹ 

¹ Department of Statistics, Faculty of Science, Eskişehir Osmangazi University, Eskişehir, Türkiye.

ABSTRACT

The process of determining the values which a time series will receive in the future is a very important concept. The fuzzy time series method has been widely used in recent years as it is more convenient to process data in small samples which are incomplete and/or ambiguous, and it does not contain any assumptions for time series. In this study, fuzzy time series analysis was used to predict CO₂ emission values for Turkey. For this purpose, time series (annual) for total greenhouse gas emissions by sectors (CO₂ equivalent) between 1990 and 2016 were analyzed. The main goal of this study is to model greenhouse gas emission statistics in Turkey with fuzzy time series analysis.

The RMSE value was taken into consideration to determine the most suitable model among the analysis performed.

Keywords: Time Series Analysis, Fuzzy Time Series Analysis, CO₂ emission, RMSE, Chen Models, Gustafson-Kessel clustering algorithm

1. INTRODUCTION

Global warming and climate change are among the most important problems in recent years. Global warming is caused the global economy, energy consumption, and by gases with greenhouse effect such as carbon dioxide (CO₂), methane (CH₄), nitrous oxide (N₂O), Hydro flora carbon (HFC), Fluorocarbones (PFC), sulfur hexaflor (SF₆). Carbon dioxide (CO₂) is one of the most important greenhouse gases that cause climate change and global warming [1].

Greenhouse gases are released from both natural and human sources. The major greenhouse gases which exist in the atmosphere are water vapor (H₂O), carbon dioxide (CO₂), nitrogen oxide (N₂O), methane (CH₄), and ozone (O₃) gases. The most important greenhouse gases which are not naturally present in the atmosphere and which occur as a result of human activities are hydrofluorocarbones (HFCs), perfluorocarbones (PFCs), and sulfur hexafluoride (SF₆) gases. The amount of greenhouse gases has been increasing rapidly in recent years with economic activity and the use of fossil fuels. Consequently, this causes global warming [2]. With the atmosphere's heat retention feature, the seas and oceans do not freeze. This heating and heat retention feature of the atmosphere is called **the greenhouse effect**.

Emission factors are provided as carbon dioxide (CO₂) equivalent (CO₂). Emissions of greenhouse gases other than CO₂ (CH₄, N₂O and CFC, HCFC) are calculated separately and converted into CO₂ equivalent. During this conversion, the release amounts of each greenhouse gas are multiplied by the global warming potential of that gas [3].

Carbon dioxide (CO₂): its share in greenhouse gases is 82%. CO₂, whose amount did not change in the atmosphere for millions of years, has increased by 31% since the start of the Industrial Revolution.

According to the calculations, the annual increase of CO₂ gas in the atmosphere in the 20 years prior to 1990 was 0.4%, while the amount of increase in the following years ranged from 0.2% to 0.8%. The biggest source of CO₂ released into the atmosphere is fossil fuels, which are used a lot [4].

The Turkish Statistical Institute (TÜİK, 2018) announced that the total greenhouse gas emissions in Turkey in 2016 were 496.1 million tons of carbon dioxide equivalents. In this period, energy-derived emissions as CO₂ equivalent received the largest share of total emissions (72.8%). This was followed by industrial operations and crop use (12.6%), agricultural activities (11.4%), and waste (3.3%), respectively. Total greenhouse gas emissions as CO₂ equivalent increased by 135.4% compared to 1990. CO₂ equivalent emissions per capita were 3.8 tonnes per capita in 1990, while in 2016 it was 6.3 tonnes per capita [5].

2. LITERATURE REVIEW

2.1. Examining Classical ARIMA and CO₂ Studies

Abdullah and Pauzi (2015) examined the methods used to estimate CO₂ emissions. The articles published in international journals between 2003 and 2013 were analyzed to determine which methods should be applied and which factors have been regularly investigated [6].

Ozceylan (2018) estimated CO₂ emissions with the help of particle optimization (PSO) and artificial bee colony (ABC) techniques (models were used as linear, exponential, and quadratic) and by means of the socio-economic indicators in Turkey (energy consumption, population, GDP and number of motor vehicles). The data used are from 1980-2008 and the predictions have been made until 2030 [7].

Ayvaz et al. (2017) used different discrete grey models (DGM) to estimate energy-related CO₂ emissions in Turkey, Europe, and the Eurasian region. The data used covers the years between 1965 and 2014. With this data, CO₂ emissions from 2015-2030 have been estimated [1].

Liu et al. (2017) handled the problem of carbon emission based on carbon emission time series data and chaos theory to make the relationships between the data clearer. The BP neural network model was used to estimate carbon emissions [8].

Appiah et al. (2018) exploited a two-layer forward feed neural network model with Tangent activation function that occurs with hidden neurons where neurons are used as linear output in their work. In the study, a nonlinear least squares algorithm such as LM (Levenberg-Marquardt) was applied to estimate emission for the selected emerging economies [9].

Garip and Oktay (2018) estimated Turkey's CO₂ emissions using random forest and support vector machines methods from popular machine learning methods. In the study, data from 1965-2003 were used for training, and estimates for 2004-2014 were obtained. According to the results of the study, the Support Vector Machine yielded more successful results than the random forest method [10].

Wang et al. (2019), in their study, used the metabolic grey model (MGM), adapted exponential curve model (MECM), autoregressive integrated moving average model (ARIMA), and neural network model Back Propagation (BP) to estimate the metabolic energy demand of Central Africa [11].

Sutthichaimethee et al. (2019) made use of a second-degree autoregressive structural equality model (second-degree autoregressive SEM) [12].

Dorogoi and Mokhtar (2019) implemented trend analysis and a double exponential smoothing method using the data between 1967 and 2014 to estimate energy consumption in some sectors (industry,

agriculture, transport, and households - in general-commercial) which have a significant relationship with the greenhouse gas emissions in Iran [13].

Oyehan et al. (2017) applied trend analysis to CO₂ data for the years 1980-2008 for Persian Gulf Countries (Bahrain, Iran, Iraq, Qatar, Saudi Arabia, Kuwait, and the United Arab Emirates) [14].

Maleki et al. (2018) employed autoregressive integrated moving average (ARIMA) and Sini Network autoregressive (NNAR) techniques to the time series on water characteristics of water treatment plants. As a result of the study, it was determined that, compared to ARIMA, NNAR provided better predictive success for CO₂ in terms of R² [15].

2.2. On Reviewing the Studies Using Fuzzy ARIMA

In their study, Abd Rahman et al. (2013) envisioned a monthly air pollution index (API) for 10 years with data obtained from industrial and residential monitoring stations in Malaysia. In the study, ARIMA and Fuzzy Time Series (Chen's method and Yu's method) were used to predict API measurements. A comparison was made by obtaining RMSE values for the three proposed models. It was determined that the neural network model (ANN) provided better results [16].

Karaaslan and Gezen (2017) attempted to predict the total energy demand for Turkey and determine the amount of unused energy and the distribution of this demand among sectors. The study used annual data from 1990 to 2012 and estimated energy demand until 2023 using a fuzzy grey regression model [17].

Mahla et al. (2019) used the ARIMA model to predict emissions from biogas [18].

Atsalakis et al. (2015) examined hourly data (n=8760) for January 1, 2009-December 31-, 2009 period using an integrated neuro-fuzzy controller (PATSOs) technique. The prediction system is based on Adaptive Neural Fuzzy Systems (ANFIS) [19].

2.3. When Fuzzy and CO₂ Studies are Inspected

Tavan M (2019) introduced a new hybrid modelling to predict carbon dioxide emissions in order to make the correct decision to reduce air pollution in Iran. In the paper, CO₂ emissions in Iran in the period of 1980-2014 was predicted using three models of Auto-Regressive Distributed Lag (ARDL), Fuzzy Linear Regression (FLR), and hybrid model based on the combination of ARDL and FLR models, and then the prediction accuracy of the models is compared [20].

Examining the literature, it is observed that studies on greenhouse gas emissions and classical ARIMA, and studies on Fuzzy ARIMA and other application areas exist. However, the aim of this study is to model greenhouse gas emission statistics in Turkey with fuzzy time series analysis. For this purpose, greenhouse gas emission was modeled using four different Fuzzy ARIMA models, and their performances were evaluated.

This paper consists of four parts. The first section is the introductory section, and the second part contains fuzzy time series models. The third section is the application section. The fourth part is the concluding part.

3. FUZZY TIME SERIES

The fuzzy time series method has been widely used in recent years as it is more convenient to process data in small samples which are incomplete and/or ambiguous, and it does not contain any assumptions for time series. There is a fundamental difference between fuzzy time series and traditional time series.

The values in fuzzy time series are fuzzy clusters, whereas the values used in traditional time series are real numbers. A fuzzy set is a cluster with fuzzy boundaries.

The first definition of the fuzzy time series was proposed by Song and Chissom (1993a, 1993 b), and the method was developed by Chen (1996) [21-23]. Later, other studies were conducted on prediction problems using the fuzzy time series concept [21, 24-30].

Song and Chissom (1993a, 1993b, 1994) suggested the model of first order time-invariant fuzzy time series, and to predict an annual time series, they proposed first-order fuzzy time-varying time series [21, 22-24].

Sullivan and Woodall (1994) examined the first-order time-varying time series model proposed by Song and Chissom and the first-order time-invariant fuzzy time-series model. They compared the models to each other [30].

Song et al (1995) presented a new fuzzy time series model for a fuzzy number observation [28]. Chen (1996) developed a new prediction method using fuzzy time series [23]. Hwang et al (1998) proposed a method that eliminates the prediction problems with the use of fuzzy time series [26]. Chen and Hwang (2000) developed a method for temperature estimation using fuzzy time series [25].

Chen (2000) developed a new method for the prediction problem using high-order fuzzy time series [24].

3.1. Chen (1996) model: This method consists of 6 steps defined as follows.

Step 1: Determination of universal sets and subintervals.

In this step, the universal set is determined according to the smallest and largest values of the time series. The defined universal set is divided into a predetermined number of subintervals. If the smallest value of the time series is D_{min} and the largest value is D_{max} , the universal set is defined as follows.

$$U=[D_{min}-D_1, D_{max}+D_2] \quad (1)$$

Here, D_1 and D_2 are two small randomly chosen numbers.

Step 2: Determination of fuzzy sets: fuzzy sets defined in peer (1) are determined.

Step 3: Observations are fuzzy

Subinterval for the observation of each classical time series is determined. The fuzzy set with the largest membership value of this subinterval gives the fuzzy value of the classical time series observation.

Step 4: Determination of fuzzy relations

Determination of the fuzzy logical relationships can be explained with an example. Let the elements of t , a fuzzy time series (FTS) with five observations, be as follows. A_1, A_1, A_2, A_2, A_3 .

In this case, fuzzy relations are defined as follows.

$$A_1 \rightarrow A_1 \quad A_1 \rightarrow A_2 \quad A_2 \rightarrow A_2 \quad A_2 \rightarrow A_3$$

Fuzzy relations are grouped as follows.

$$A_1 \rightarrow A_1, A_2 \quad A_2 \rightarrow A_2, A_3$$

Step 5: Predictions are obtained.

There are 3 different situations in the process of obtaining predictions.

Case 1, A_j is the predictive value for time t when there is only one fuzzy logical relationship as $A_i \rightarrow A_j$ in the fuzzy relations sequence.

Case 2, If $A_i \rightarrow A_j, s, Al$, the predictive value is equal to A_j, As, Al .

Case 3, If $A_i \rightarrow \emptyset$, the predictive value equals A_i .

Step 6: Obtained predictive values are defuzzified.

‘Centralization-defuzzification method’ is used to obtain the results. There are 3 different situations in defuzzification process.

Case 1, if the predictive value is equal to A_j , defuzzified predictive value is the cluster center c_j of A_j fuzzy set.

Case 2, if the predictive value is $A_{j,l}$, the defuzzified predictive value is calculated in the form of $(c_j + c_s + c_l) / 3$ as an arithmetic average of the cluster centers of the fuzzy sets A_j, As, Al .

Case 3, if A_i is equal to the empty set (\emptyset), then the defuzzified predictive value is cluster center c_i of AI fuzzy set [31].

3.2. Chen (2002) Model: General Definitions

Let $U = \{u_1, u_2, u_3, \dots, u_n\}$ be the universal cluster. The elements of U have intervals. These intervals are obtained by breaking down the universal set according to a previously determined fixed interval length. Fuzzy sets of U are defined as:

$$sA = f_A(u_1)/u_1 + f_A(u_2)/u_2 + \dots + f_A(u_n)/u_n \quad (2)$$

f_A : is the membership function of A function. $f_A : U \rightarrow [0,1]$ and (u_i) denote the membership degree of the UI in A [32].

Definition 1:

Let $X(t)$ be a real-valued subset with $(t = \dots, 0, 1, 2, \dots)$. $F(t)$ is the sum including the fuzzy set defined as $f_i(t)$ ($i = 1, 2, \dots$) and is defined as a fuzzy time series to $F(t)$.

$F(t)$ time series obtained after determining A_i fuzzy set corresponding to appropriate sub-intervals of the X time series and to the observation of each time series is called “**fuzzy time series**”. $F(t)$ is also a function of time. In other words, since the universal set can take different values at different times, $F(t)$ can also take different values at different times.

In definition 1;

1. $F(t)$ is a function of time.
2. $F(t)$ can be thought of as a verbal variable, taking verbal values where all the values it will take can be represented by fuzzy sets.
3. $f_i(t)$ ($i = 1, 2, \dots$) are possible verbal values of $F(t)$. $f_i(t)$ ($i = 1, 2, \dots$) is represented by fuzzy sets.

Definition 2: including $F(T)$ fuzzy time series, for any time $F(T) = F(T-1)$, and $F(T)$ has only finite elements. Thus, $F(t)$ is called time-invariant fuzzy time series.

Definition 3:

Let $F(t)$ be a fuzzy time series. If $F(t), F(t-1), F(t-2), \dots$ causes $F(t-n)$, then the fuzzy logical relationship is expressed as follows.

$F(t-n), \dots, F(t-2), F(t-1) \rightarrow F(t)$ (3)
and it is called n-th order fuzzy time series predictive model.

Chen (2002) method consists of the following stages.

Step 1: Determination of universal sets and subintervals.

In this step, the universal set (U) is determined with the smallest (Dmin) and the largest value (Dmax) of the time series.

$$U=[Dmin-D_1, Dmax+D_2] \tag{4}$$

Here, D_1 and D_2 are two randomly chosen positive numbers.

A predetermined number of subintervals of u_i are defined so that this universal set is $U=\{u_1, u_2, u_3, \dots, u_n\}$.

Step 2: Determination of fuzzy sets

The fuzzy A_1, A_2, \dots, A_k . sets are defined in the universal set of U.

$$\begin{aligned} A_1 &= a_{11}/u_1 + a_{12}/u_2 + \dots + a_{1m}/u_m \\ A_2 &= a_{21}/u_1 + a_{22}/u_2 + \dots + a_{2m}/u_m \end{aligned} \tag{5}$$

.

.

.

$$A_k = a_k/u_1 + a_k/u_2 + \dots + a_{km}/u_m$$

Here, $a_{ij} \in [0,1]$ ve $1 \leq i \leq k$ $1 \leq j \leq m$. The values of a_{ij} in the A_i fuzzy set.

Step 3: Observations are defuzzified.

It is matched with the fuzzy set with the largest membership value for the subinterval set determined for each time series data. Thus, the time series is defuzzified.

Step 4: Determination of fuzzy relations

The determination of the fuzzy logical relationships can be explained with an example., let the elements of (t), a FTS with five observations, be as follows. A_1, A_1, A_2, A_2, A_3 . In this case, fuzzy relations are determined as follows. $A_1 \rightarrow A_1$ $A_1 \rightarrow A_2$ $A_2 \rightarrow A_2$ $A_2 \rightarrow A_3$ Fuzzy relations are grouped as follows. $A_1 \rightarrow A_{1,2}$ $A_2 \rightarrow A_2, A_3$

Fuzzy predictions are obtained. Using the model obtained in the previous step, the outputs of the model are calculated. The calculated outputs are the numbers of fuzzy sets which the predictions belong to. Accordingly, fuzzy predictions are derived from the outputs of the model obtained in the previous step.

Step 5: Calculating predictions.

The following principles are taken into account at this stage.

Case 1: If fuzzified observations for year i, \dots, \dots , from $K(k \geq 2)$ k^{th} level are $A_{ik}, A_{i(k-1)}, \dots$, and A_{il} , and there is a fuzzy logic present in k^{th} level fuzzy logic relations, then the groups are defined as follows.

$$A_{ik}, A_{i(k-1)}, \dots, A_{il} \rightarrow A_j$$

$A_{ik}, A_{i(k-1)}, \dots, A_{il}$ ve A_j are fuzzy sets, and they are in m_j interval which is the midpoint of u_j and u_j , which is the largest membership of A_j , and predictive value for year i is m_j .

Case 2 If observations fuzzified from the k^{th} level ($k \geq 2$) for the year are $A_{ik}, A_{i(k-1)}, \dots$, and A_{il} , if there is a fuzzy logic relationship in the k^{th} level fuzzy logic relations, the groups are defined as follows.

$$A_{ik}, A_{i(k-1)}, \dots, A_{il} \rightarrow A_{j1}$$

$$A_{ik}, A_{i(k-1)}, \dots, A_{il} \rightarrow A_{j2}$$

.

.

.

$$A_{ik}, A_{i(k-1)}, \dots, A_{il} \rightarrow A_{jp}$$

$A_{ik}, A_{i(k-1)}, \dots, A_{il}, A_{j1}, A_{j2}, \dots, A_{jp}$ are fuzzy sets. It can be seen that there is an uncertainty to predict the record of year i (fuzzy observation for year i can be A_{j1}, A_{j2} or A_{jp}). In this case, there should be high-order fuzzy observations for year i . Therefore, there will be no uncertainty for the prediction of the year i . To eliminate this uncertainty, suppose there is an integer value of m ($m \geq k$). For the year i , the m^{th} degree fuzzified observation values are $A_{im}, A_{i(m-1)}, \dots, A_{i1}$ and the fuzzy logic relationships in m^{th} degree fuzzy logic relation groups are defined as follows:

$$A_{im}, A_{i(m-1)}, \dots, A_{i1} \rightarrow A_j$$

$A_{im}, A_{i(m-1)}, \dots, A_{i1}$ and A_j are fuzzy sets.

The largest membership value of A_j is u_j , and it occurs in m_j interval which is the midpoint of u_2, \dots, u_j . Consequently, the predictive value of year i is m_j .

Case 3: Let the observations fuzzified from k^{th} degree for year i be $A_{ik}, A_{i(k-1)}, \dots$, and A_{il} . If the right side of the fuzzy logic relation is empty, the logical relation groups of k^{th} degree are defined as follows.

$$A_{ik}, A_{i(k-1)}, \dots, A_{il} \rightarrow \#$$

Here, $A_{ik}, A_{i(k-1)}, \dots$ and A_{il} are fuzzy sets, and the largest membership value of $A_{ik}, A_{i(k-1)}, \dots$ and A_{il} is $u_{ik}, u_{i(k-1)}, \dots$; and it occurs in $m_{ik}, m_{i(k-1)}, \dots, i$ and m_{il} interval. Thus, the predicted value for year i is calculated as follows [31].

$$\frac{1 \cdot m_{ik} + 2 \cdot m_{i(k-1)} + \dots + k \cdot m_{ik}}{1 + 2 + \dots + k} \quad (6)$$

Step 6. Defuzzification process for fuzzy predictions

The defuzzification process is applied to fuzzy predictions. During defuzzification, the centralization method is used. If fuzzy prevision is A_j , defuzzified prediction is the midpoint value of u_j which is the interval with the highest membership value for this fuzzy set.

3.3. Fuzzy Time Series Models Based on Fuzzy Clustering

Gustafson ve Kessel (1979)

Gustafson and Kessel (1979) proposed an adapted version of the fuzzy clustering algorithm. This algorithm uses the Mahalanobis distance instead of the Euclidean distance. The distance of Mahalanobis forms ellipse-shaped clusters.

Mahalanobis distance ($d_{ikA_i}^2$), the distance norm of the GK algorithm, is defined as

$$d_{ikA_i}^2 = (Z_k - V_i)^T A_i (Z_k - V_i) \quad (7)$$

The purpose function of the GK clustering algorithm is expressed in equation (8).

$$J(X, U, V, A) = \sum_{i=1}^N \sum_{k=1}^c (u_{ik})^m d_{ikA_i}^2 \quad (8)$$

The steps of the Gustafson-Kessel clustering algorithm are as follows:

Step 1: Initial values, cluster number (c), fuzzification index (m), number of iterations (i), membership degrees matrix (u), cluster center values (v) and stop criteria (ϵ) are determined. Here, it is defined as (> 0), ($1 < c < N$), ($m > 1$).

Step 2: Fuzzy cluster centers are calculated.

$$v_k = \frac{\sum_{i=1}^N u_{ik}^m x_i}{\sum_{i=1}^N u_{ik}^m}, \quad 1 \leq k \leq c \tag{9}$$

Step 3: The Mahalanobis distance is calculated for each element.

Step 4: Fuzzy covariance matrices (F_i) are calculated for each set separately.

$$F_i = \frac{\sum_{k=1}^N (d_{ik})^m (Z_k - V_i)(Z_k - V_i)^T}{\sum_{k=1}^N (d_{ik})^m} \tag{10}$$

Step 5: The membership matrices are updated.

$$u_{ik} = \left[\sum_{j=1}^c \left(\frac{d_{ikA_k}}{d_{ijA_k}} \right)^{2/(m-1)} \right]^{-1} \tag{11}$$

Step 6: The process is terminated when $\|V_t - V_{t-1}\| < \epsilon$ condition is met. If not, return to step 2 [33-34].

4. ANALYSIS OF GREENHOUSE GAS EMISSION STATISTICS in TURKEY with FUZZY TIME SERIES ANALYSIS

Fuzzy logic applications, unlike statistical methods, may include methods that can be analyzed with a small number of data which do not require any assumptions. Fuzzy time series is also a method that can be applied in cases where the number of samples is small without requiring any assumption on the time series. The most important step in the implementation of the fuzzy time series models in the literature is that the fuzzy equivalent of the classical time series can be obtained, that is they can be fuzzified. The main purpose of the application is to model the greenhouse gas emission statistics in Turkey with fuzzy time series analysis. Expressing which model is the most appropriate in the analysis performed will be evaluated by considering the RMSE value.

In the implementation phase of the study, total greenhouse gas emissions (CO₂ equivalent) in Turkey between 1990 and 2016 will be evaluated using fuzzy time series analysis. For this purpose, data (Table 1) will be analyzed using Chen (1996) method, Chen (2002) method, and fuzzy time series models based on fuzzy clustering, which are fuzzy time series based on fuzzy C-Means (FCMFTS) and fuzzy time series based on Gustafson - Kessel clustering (GKFTS).

Table 1. Total greenhouse gas emissions by sector in Turkey (CO₂ equivalent)

Year	Greenhouse gas emission (million tons)	Year	Greenhouse gas emission (million tons)	Year	Greenhouse gas emission (million tons)
1990	210,7	1999	272,1	2008	387,9
1991	218,7	2000	293,5	2009	395,9
1992	224,7	2001	274,4	2010	402,6
1993	233,4	2002	280,8	2011	431,4
1994	227,6	2003	300,3	2012	445,6
1995	242,2	2004	311,2	2013	439,0
1996	261,2	2005	332,7	2014	451,8
1997	272,6	2006	356,8	2015	469,9
1998	274,5	2007	390,5	2016	496,1

(Source: Turkish Statistical Institute 13th 2018)

4.1. Chen 1996 Model Results

Implementing the prediction algorithm of Chen 1996 fuzzy time series model, fuzzy time series model prediction analysis was performed for CO₂ emission value in Turkey. After the related analysis, RMSE value for CO₂ emissions of Chen (1996) model was obtained as 11.61.

Table 2. Chen (1996) Model Results

Year	Greenhouse gas emission (million tons)	Chen (1996)
2012	445,6	445,6
2013	439	439
Test Data 2014	451,8	451,8
2015	469,9	469,9
2016	496,1	496,1
	RMSE	11,61

4.2. Chen (2002) Model Results

Chen (2002) model, one of the fuzzy time series analysis methods, was applied for CO₂ emission value in Turkey. The Chen (2002) model is the high-order fuzzy time series model. Analyzing the Chen 2002 model for the related data, the values in Table 3 were obtained. In the analysis of time series, Chen (2002) model was tested from 2nd order to 12th order model by changing the number of fuzzy sets between 3 and 10.

The optimal model order and number of fuzzy sets were determined according to the RMSE criteria calculated for the validation by taking the time series training set between 1990 and 2006 and the observations validity set between 2007 and 2011. The performance of the method was observed using as a test set between 2012-2016 in the last 5 observations. The best results were obtained when the model rating was chosen as 2 and the number of fuzzy sets as 5. For CO₂ emissions in Turkey, the RMSE value obtained by Chen 2002 method was obtained as 24.86.

Table 3. Chen (2002) Model Results

Year	Greenhouse gas emission (million Tons)	Chen (2002) Order=2, number of cluster=5
2012	445,6	410,4800
2013	439	448,5333
Test Data 2014	451,8	429,5067
2015	469,9	448,5333
2016	496,1	467,5600
	RMSE	24,86

4.3. Fuzzy Time Series Model Based on Fuzzy Sets

Fuzzy time series analysis based on fuzzy clustering uses fuzzy cluster analysis methods in the step of converting into fuzzy time series. In this study, analysis was performed using fuzzy time series based on fuzzy c-means and fuzzy time series models based on Gustafson-Kessel clustering. In both methods, the number of clusters was taken as 5. As a result of the analysis, the RMSE value of the FCMFTS (Fuzzy-Cluster Means Time Series) method was obtained as 30.42, and the RMSE value of the GKFTS method was 25.85. The related results are given in Table 3.

Table 4: Fuzzy Time Series Model Based on Fuzzy Sets Results :

Year	Greenhouse gas emission		
	(million tons)	FCMTS	GKFTS
2012	445.6	417,4968	430,0034
2013	439	417,4968	430,0034
Test Data 2014	451,8	417,4968	430,0034
2015	469,9	417,4968	430,0034
2016	496,1	417,4968	430,0034
	RMSE	30,42	25,85

5. CONCLUSIONS

In this study, fuzzy time series analysis was used to predict CO₂ emission values for Turkey. For this purpose, time series (annual) for total greenhouse gas emissions by sectors (CO₂ equivalent) between 1990 and 2016 were analyzed. In the data analysis section of this study, total greenhouse gas emissions (CO₂ equivalent) in Turkey between 1990 and 2016 will be evaluated using fuzzy time series analysis. For this purpose, data (Table 1) will be analyzed using Chen (1996) method, Chen (2002) method, and fuzzy time series models based on fuzzy clustering, which are fuzzy time series based on fuzzy C-Means (FCMFTS) and fuzzy time series based on Gustafson - Kessel clustering (GKFTS) and the performances of the models were evaluated.

Expressing which model is the most appropriate in the analyses performed was put forward considering the RMSE value. As a result, modeling the greenhouse gas emission statistics with fuzzy time series analysis as the main goal of the study was achieved, and the applicability of four different fuzzy time series models proposed to the related data set was revealed. Comparing RMSE values, it was seen that Chen 1996 model had the smallest value. In this study, it was tried to estimate the CO₂ emission value for Turkey by using Chen (1996), Chen (2002) and Gustafson and Kessel (1979) techniques. Since such a comparison is made, the study is original.

The techniques used in the study can be used for other time series. As there is no other study using four different fuzzy time series as in this study, the study has originality as it is.

CONFLICT OF INTEREST

The author stated that there are no conflicts of interest regarding the publication of this article.

REFERENCES

- [1] Ayvaz B, Kusakçı AO, Temur GT. Energy-related CO₂ emission forecast for Turkey and Europe and Eurasia A discrete grey model approach. *Grey Systems: Theory and Application* 2017; 7(3):,437-4532.
- [2] Kuşkaya S, Gençoğlu P. A comparison of OECD countries by the years 1995-2015 to green gas Emission analysis: a statistical analysis *International Journal of Disciplines Economics and Administrative Sciences Studies*, 2017; 3(3):177-188.
- [3] Tatar V, Özer MB. Effects on climate change of greenhouse gases emissions:current status analysis of Turkey. *Journal of Social and Humanities Sciences Research* 2018; 5(30):3993-3999.
- [4] Akın G Global warming, reasons and outcomes. *Ankara Üniversitesi Dil ve Tarih-Coğrafya Fakültesi Dergisi*, 2006; 46(2):29-43.
- [5] Dikmen AÇ. Contributions of electricity generation by the sun and wind on reduction greenhouse gas emissions and environmental costs in Turkey. *Turkish Studies*, 2019; 14(2):275-293.
- [6] Abdullah L, Pauzi HM. Methods in forecasting carbon dioxide emissions: A decade review, *Jurnal Teknologi*, 2015; 75(1):67-82.
- [7] Özceylan E. Forecasting CO₂ Emission of Turkey: Swarm intelligence approaches. *International Journal of Global Warming*, 2016; 9(3): 337-61.
- [8] Liu Y, Tian Y, Chen M. Research on the prediction of carbon emission based on the chaos theory and neural network. *International Journal of Bioautomation*, 2017; 21(4), Special Issue, 339-348.
- [9] Appiah K, Du J, Appah R, Quacoe D. Prediction of potential carbon dioxide emissions of selected emerging economies using artificial neural network. *Journal of Environmental Science and Engineering A*, 2018; 7: 321-335.
- [10] Garip E. Oktay AB. CO₂ emisyonunun makine öğrenmesi metotları ile tahmin edilmesi. *Conference: 2018 International Conference on Artificial Intelligence and Data Processing (IDAP)*, 262-266, 28-30 September 2018, Malatya, Turkey.
- [11] Wang L, Zhan L. Li R. Prediction of the Energy Demand Trend in Middle Africa—A Comparison of MGM, MECM, ARIMA and BP Models *Sustainability*, 2019; 11, 1-16.
- [12] Sutthichaimethee P, Apinyar C, Suyaprom S. A forecasting model for economic growth and CO₂ emission based on industry 4.0 political policy under the government power: adapting a second-order autoregressive-sem. *Journal of Open Innovatin Technolgy Market and Complexity*, 2019; 5(3): 69-89.
- [13] Doroodi M, Mokhtar A. Comparison of time series approaches for prediction of energy consumption focusing on greenhouse gases emission in Iran. *International Journal of Energy Sector Management*, 2019; 13(3):486-499.
- [14] Oyehan TA, Tawabini BS. Forecasting CO₂ emissions in the Persian Gulf States. *Global Journal of Environmental. Science and Management*, 2017; 3(1): 1-10, Winter 2017.

- [15] Maleki A, Nasser S, Aminabad MS, Hadi M. Comparison of ARIMA and NNAR models for forecasting water treatment plant's influent characteristics. *KSCE Journal of Civil Engineering*, 2018; 22(9):3233-3245.
- [16] Abd Rahman NH, Lee MH, Talib ML, Suhartono S. Forecasting of air pollution index with artificial neural network. *Jurnal Teknologi (Sciences and Engineering)*, 2013; 63(2):59–64.
- [17] Karaaslan A, Gezen M. Forecasting of Turkey's sectoral energy demand by using fuzzy grey regression model. *International Journal of Energy Economics and Policy*, 2017; 7(1): 67-77.
- [18] Mahla SK, Parmar KS, Singh J, Dhir A, Sandhu SS, Chauhan BS., Trend and time series analysis by ARIMA model to predict the emissions and performance characteristics of biogas fueled compression ignition engine, *Energy Sources, Part A: Recovery, Utilization, and Environmental Effects*, 2019; <https://doi.org/10.1080/15567036.2019.1670286>
- [19] Atsalakis G, Frantzis D, Zopounidis C Energy's exports forecasting by a neuro-fuzzy controller. *Energy Systems*, 2015, 6(2):249-267. DOI 10.1007/s12667-015-0140-1
- [20] Tavan M. Estimation and forecast of carbon dioxide emission in Iran: Introducing A New Hybrid Modelling. *Journal of Economics and Management*, 2019; 36 (2) 144-167.
- [21] Song Q, Chissom BS. Forecasting enrollments with fuzzy time series, Part I. *Fuzzy Sets and Systems*, 1993-a; 54(1):1-9.
- [22] Song Q, Chissom BS. Fuzzy time series and its models", *Fuzzy Sets and Systems*, 1993-b; 54 (3): 269-277.
- [23] Chen SM. Forecasting enrollments based on fuzzy time-series. *Fuzzy Sets and Systems*, 1996, 81(3):311-319.
- [24] Chen SM. Using high-order fuzzy time series for handling forecasting problems. *Proceedings of the 11th National Conference on Information Management, Kaohsiung, Taiwan, 2000; Republic of China, 2000.*
- [25] Chen SM, Hwang JR Temperature predication using fuzzy time series. *IEEE Transactions on Systems, Man and Cybernetics, Part B: Cybernetics*, 2000; 30(2):263-275. DOI: 10.1109/3477.836375
- [26] Hwang JR, Chen SM, Lee CH (1998) Handling forecasting problems using fuzzy time series. *Fuzzy Sets and Systems*, 100 (2):217- 228. [https://doi.org/10.1016/S0165-0114\(97\)00121-8](https://doi.org/10.1016/S0165-0114(97)00121-8)
- [27] Song Q, Chissom BS. Forecasting enrollments with fuzzy time series, Part II.. *Fuzzy Sets and Systems*, 1994; 62(1):1- 8.
- [28] Song Q, Leland RP. Adaptive learning defuzzification techniques and applications. *Fuzzy Sets and Systems*, 1996; 81(3):321-329.
- [29] Song Q, Leland RP, Chissom BS. A new fuzzy time-series model of fuzzy number observations. *Fuzzy Sets and Systems*, 1995; 73(3):341- 348.
- [30] Sullivan J, Woodall WH . A Comparison of fuzzy forecasting and markov modeling. *Fuzzy Sets and Systems*, 1994; 64(3):279- 293.

- [31] Eğrioğlu E, Aladağ CH, Yolcu U, Uslu VR, Erilli NA. Fuzzy time series forecasting method based on Gustafson–Kessel fuzzy clustering, *Expert Systems with Applications*, 2011; 38(8), 10355-10357.
- [32] Chen SM Forecasting enrollments based on highorder fuzzy time series. *Cybernetics and Systems: An International Journal*, 2002; 33(1): 1-16.
- [33] Gustafson D, Kessel W. Fuzzy clustering with a fuzzy covariance matrix. *Proc. 18th IEEE CDC Conference, San Diego, USA, 1979; 761-766.*
- [34] Balasko B, Abonyi J, Feil B. *Fuzzy clustering and data analysis toolbox*. 2005; Department of Process Engineering University of Veszprem.



RESEARCH ARTICLE

QUARTZ FIBER RADOME AND SUBSTRATE FOR AEROSPACE APPLICATIONS

Mete BAKIR *, 

Department of Mechanical Engineering, Faculty of Engineering and Natural Sciences, Ankara Yildirim Beyazıt University,
Ankara, Turkey

ABSTRACT

Quartz fiber is an ultra-high purity silica glass having immediate use applications on radomes and satellite communications for aerospace systems. In this study, the uses of quartz fiber as an antenna radome and a dielectric substrate were investigated for a patch antenna designed to operate at $f=8$ GHz. In order to compare the performance of quartz fiber as an antenna radome, glass fiber is examined for the same antenna. For the dielectric substrate case, quartz fiber is compared with the well-known and widely used dielectric substrate of FR-4. The electromagnetic properties of the quartz fiber were examined for different temperature values using a free space measurement setup and a controllable furnace. The antenna parameters, including radiation pattern, gain, return loss and beamwidth, are investigated and compared in detail for all cases in order to demonstrate the effects of using quartz fiber as a radome and an antenna substrate. The results highlight that quartz fiber shall have high-end use for low electromagnetic interference characteristics without compromising on structural integrity.

Keywords: Quartz fiber, Glass fiber, Radome, Substrate, Antenna

1. INTRODUCTION

Quartz fiber, which is also known as fused silica fiber or silica glass fiber, is a type of fiber made from quartz glass. Quartz is a type of ultra-pure crystalline silica. Quartz fiber is preferred due to its unique properties, such as high strength, high temperature resistance as well as low thermal expansion coefficient [1-3]. The history of quartz fiber dates back to the early 20th century, when researchers began exploring the potential of silica as a material for making fibers. Researchers at Corning Glass Works developed a process for making fibers from silica glass in 1930s. This process covered melting high-purity silica and drawing it into fibers using a special apparatus. Since then, Quartz fiber has been used in a variety of applications, including insulation, reinforcement, and structural support. In the 1960s, quartz fiber was used to make the first optical fibers, which revolutionized the telecommunications industry. Today, quartz fiber is used in a variety of applications, including telecommunications, aerospace, and automotive industries, as well as in scientific researches [4-6].

By definition, a radome is a protective cover or enclosure that is used to protect radar or other types of antennas from the external elements. Quartz fiber-made radomes are used in a variety of applications, including satellite communication, air traffic control, and radar systems. Quartz fiber-made radomes are chosen for their high transparency to electromagnetic waves, which makes them ideal for use with radar and other types of antennas. They are also resistant to extreme temperatures and UV radiation, making them suitable for use in a variety of extreme environments. In addition, radomes made by using quartz fiber are very durable and have a long lifespan, making them a cost-effective choice for many applications [7-9]. On the other hand, radomes made with quartz fiber can be more expensive than other traditional radomes because of the initial high cost of quartz raw material. Because of the fragile and brittle nature of quartz, they require careful handling and processing during manufacture. Despite these

challenging properties, radomes made with quartz fiber are widely used in a variety of applications due to their unique combination of transparency, durability, and resistance to extreme conditions [10, 11]. In the literature, Yaoyao Wang studied the applicability of quartz fiber-based radomes for high frequencies, specifically between 10-20 GHz [8]. As well, there are several other studies on the use of quartz as substrate and radome [12]. In a study conducted by Dyck et al., quartz is used as the substrate of an antenna operating at 300 GHz [14]. In another study, Xu et al. investigated quartz glass as the substrate of a patch antenna array for radar applications [15].

In line with this, antennas operating in this frequency range are used in a variety of applications, including satellite communication, radar, and wireless networking. Patch antennas is composed of a ground plane, radiating patch and a dielectric substrate which is mostly preferred as FR-4 due to its relatively high performance and low-cost. Patch antennas are known for their high gain and narrow beam width, which makes them well suited for directional communication and radar applications. They are also relatively simple and inexpensive to manufacture, which makes them a popular choice for many applications. However, patch antennas are sensitive to the size and shape of the patch and the dielectric constant of the substrate, so careful design and manufacturing are required to achieve the desired performance characteristics. The substrate is typically a dielectric material, which is a type of insulating material that can support the propagation of electromagnetic waves. Antenna substrates are used to provide mechanical support for the antenna and to help shape and direct the electromagnetic field generated by the antenna. Antenna substrates have effects on antenna performance as well as providing mechanical support and shaping the electromagnetic field [13]. Ceramic and glass substrates are often chosen for their high dielectric constant, which allows them to support the propagation of electromagnetic waves with low loss. Plastic and metal substrates are often preferred for their low cost and ease of machining/ Overall, along with the radome application, in this study, a printed circuit board (PCB) patch antenna operating at $f=8$ GHz was investigated. Combined the radome application and patch antenna cases, the performance of quartz fiber is compared to other well-known, conventional alternative materials.

2. MATERIALS AND METHODS

2.1. PCB Patch Antenna Design

The patch antenna was designed by etching a metallic patch onto a dielectric substrate. The patch was then connected to a feed line, which supplies the RF energy to the antenna (Figure-1). The patch and feed line were designed to operate at a specific frequency or range of frequencies between 2 GHz to 20 GHz.

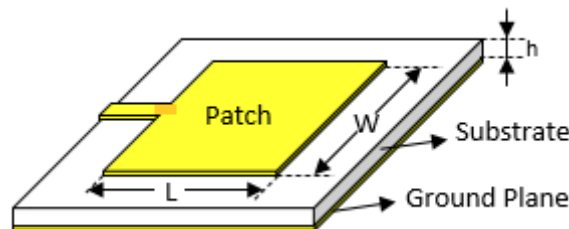


Figure 1. The schematic perspective view of the patch antenna

The dimensions of the patch antenna (W -width and L -length) used within the scope of the study were determined with the utilization of appropriate equations as shown below. In this study, dimensions of a patch antenna (W -width and L -length) can be calculated as follows;

$$W = \frac{c}{2f_0\sqrt{\frac{\epsilon_R+1}{2}}} \text{ and } L = \frac{c}{2f_0\sqrt{\epsilon_{eff}}} - 0,824h \left(\frac{(\epsilon_{eff}+0.3)\left(\frac{W}{h}+0.264\right)}{(\epsilon_{eff}-0,258)\left(\frac{W}{h}+0.8\right)} \right)$$

Here, ϵ_R is the relative permittivity of the substrate used for the patch antenna, c is the speed of light, f_0 is the central frequency point, h is the thickness of the substrate.. In addition, ϵ_{eff} can be calculated as;

$$\epsilon_{eff} = \frac{\epsilon_R+1}{2} + \frac{\epsilon_R-1}{2} \left[\frac{1}{\sqrt{1+12\left(\frac{h}{W}\right)}} \right]$$

In order to have operating frequency at $f=8$ GHz, W and L were optimized as 10 mm and 7.77 mm as shown below. In order to have better return loss, the feeding line was selected to have 1mm thickness as shown in the figure below (Figure 2).

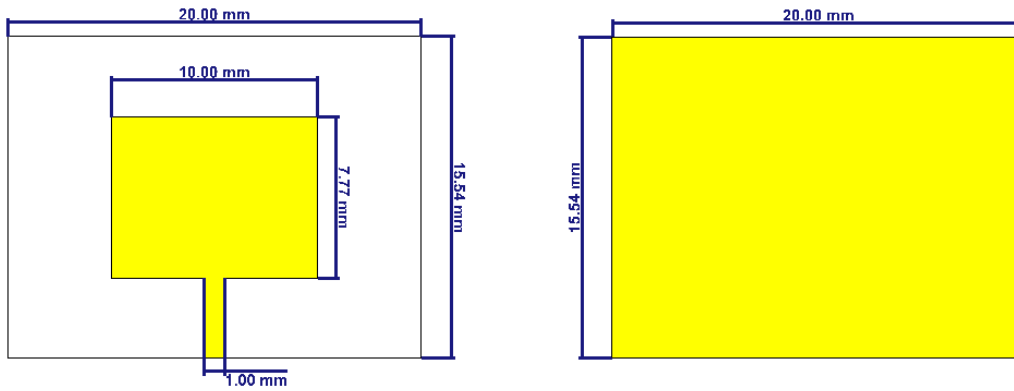


Figure 2. Dimensions of the designed PCB patch antenna (Left - Front side and Right – Back side)

2.2. Electromagnetic Characterization of Quartz Fiber and Glass

Quartz fiber and glass fiber specimens were manufactured in 30 cm x 30 cm dimensions in order to test on a free-space electromagnetic measurement setup, which involves the use of two linearly polarized high gain antennas and a vector network analyzer. A sample setup is shown below (Figure 3).

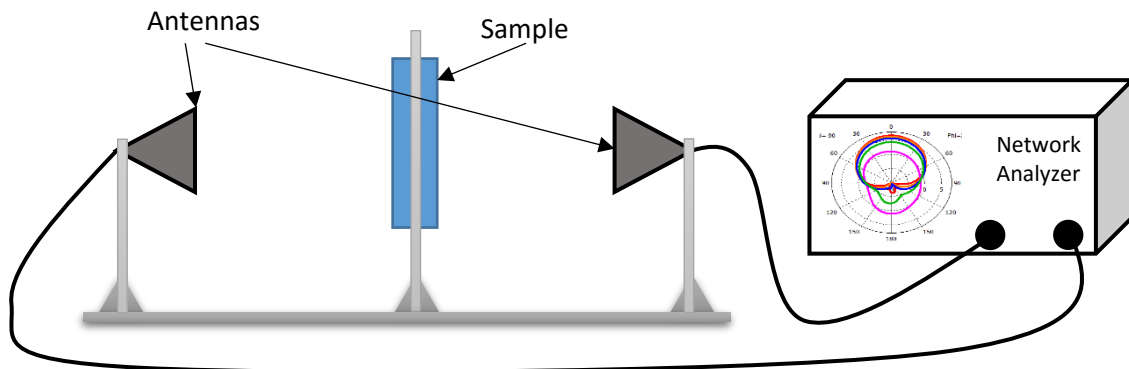


Figure 3. The schematic of the free space measurement setup

In this setup, the calibration was made using a metal plate and air for full Reflection and full Transmission. By using this method, the reflection and the transmission behavior of the sample under test were measured. These parameters are known as Scattering Parameters (S-parameters for short). There are a few methods to obtain electrical permittivity values from scattering parameters. One of the most commonly used one is Nicholson Ross Weir (NRW) method developed by Nicholson, Ross and Weir [17,18]. The obtained complex electrical permittivity (ϵ) values for the samples are given in the figure below for quartz fiber and glass.

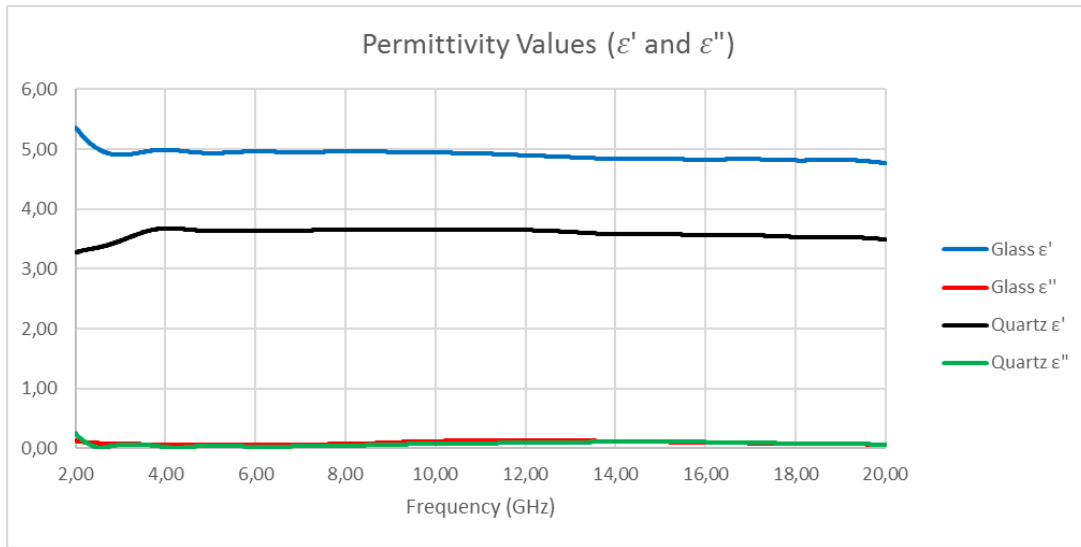


Figure 4. Electrical permittivities of glass and quartz fibers between 2 GHz to 20 GHz frequency range.

3. RESULTS AND DISCUSSION

The results will be given for two cases. The first case is about the use of Quartz Fiber as the substrate and the second case is about the use of Quartz Fiber as the radome of a patch antenna.

3.1. Quartz and Glass as the Substrate of the PCB Patch Antenna

A patch antenna is a type of radio frequency (RF) antenna that is commonly used in wireless communication systems. It is called a "patch" antenna because it consists of a flat or slightly curved rectangular patch of conductive material, which was chosen as copper in our case mounted on a dielectric substrate. The patch antenna is often mounted on a ground plane, which is also chosen as copper in our case. During the design phase, the substrate was selected as FR-4 to finalize the antenna design in order to set the operating frequency as $f=8$ GHz. The substrate material was then changed to Quartz and Glass fiber, respectively and the return loss graphs were obtained (Figure 5).

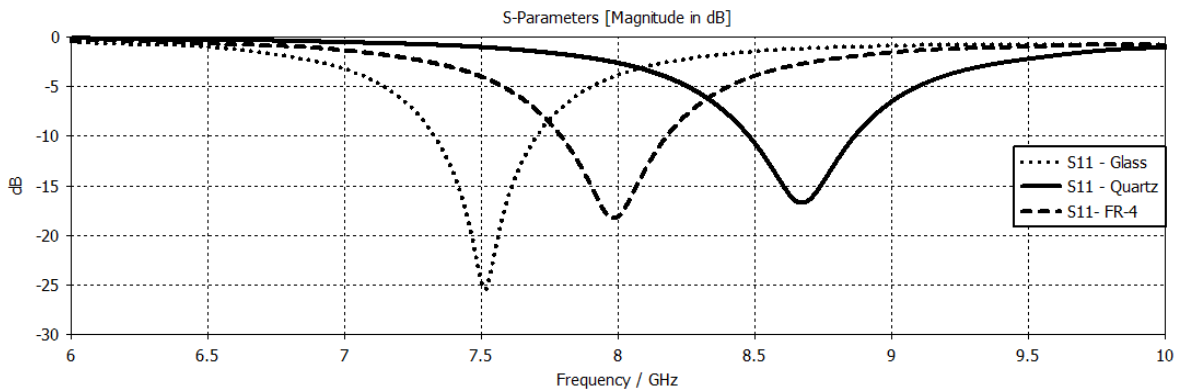


Figure 5. Return loss of the antenna with quartz, glass, and FR-4 substrates.

As observed in the return loss graphs (S11) of the designed antenna with different substrates, the antenna operating frequency shifts depending on the substrate type. Considering that the electrical permittivity value of FR-4 is about 4.3, glass fiber is about 5.2, and quartz fiber is about 3.7 we can easily say that the operating frequency shifts to higher frequencies as the permittivity value of the substrate decreases. The antenna operates at 8 GHz for FR-4 substrate, it shifts to a lower frequency ($f=7.5$ GHz) for Glass fiber substrate and shifts to a higher frequency ($f=8.5$ GHz). Therefore, the effect of the substrate must be considered while designing the antenna. Since these antennas may be used under different environmental conditions including different temperature values, the dielectric constant variation of quartz material was tested using the free space measurement setup with temperature controlled furnace. The measurement was performed starting from room temperature up to 175° (Figure 6). As seen in the figure, the electrical permittivity values of Quartz increase as the temperature increases. The temperature effect on the antenna performance in terms of the substrate used is examined by P. Kabacik and M. E. Bialkowski [19]. In their study, they classified the substrates under four different categories in terms of the dielectric values and their temperature dependence behaviors for microstrip patch antennas.

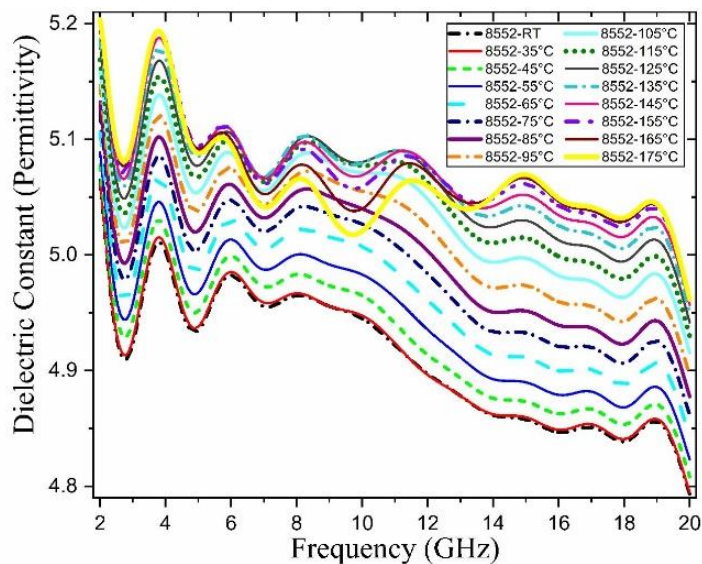


Figure 6. Dielectric constant of the quartz sample at different temperatures

In order to check the electromagnetic performance of an antenna, farfield radiation patterns should also be examined along with its return loss behavior. For this purpose, farfield radiation patterns have been obtained and the results are given in the figure below for three frequency points obtained in the return loss graphs ($f=7.5$ GHz, 8 GHz and 8.5 GHz) (Figure 7).

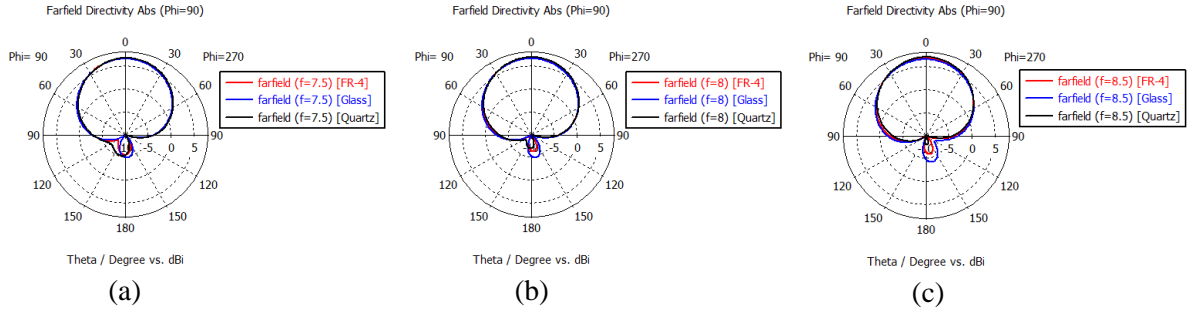


Figure 7. Farfield radiation pattern for quartz, glass, and FR-4 substrates at $f=7.5$, 8, 8.5 GHz.

Farfield radiation pattern plots are given in polar form showing the electromagnetic radiation behavior of the antenna in far-field region. From the radiation pattern plots, gain, half power beamwidth (HPBW), side lobes and back lobes of the antenna can be determined. As known, gain of an antenna is a quantity measuring the radiated electromagnetic energy in a particular direction which can be determined from the maximum radiation intensity of the main lobe in the radiation pattern. Half power beamwidth is the angle indicating the directional ability of the antenna. It is the angular width of the main lobe of the radiation pattern of the antenna showing the angle between two points where the radiation intensity is half of its maximum value. As shown in Figure 7, there is no significant difference between the results with different substrates for all frequencies. However, there are slight changes in terms of back lobe magnitudes. In order to clarify the results, these parameters along with the front to back ratio and main lobe direction of the antenna were tabulated in Table 1. Here, the front to back ratio refers to the ratio between the main lobe and back lobe magnitudes. One can see from the table that the main lobe direction of the designed antenna does not change significantly with various substrates while HPBW changes up to 10° which can be used for applications requiring different HPBW. On the other hand, the antenna gain increases when quartz substrate was used compared to the other substrate materials.

Table 1. Performance parameters of the antenna for different substrates at the three frequencies.

Frequency (GHz)	Material	Gain (dB)	HPBW	Front to Back Ratio	Main Lobe Direction
7.5	FR-4	6.59	95.0°	-12.2	0.0°
	Glass	6.49	96.6°	-11.5	0.0°
	Quartz	6.67	93.5°	-12.0	2.0°
8.0	FR-4	6.72	94.4°	-13.0	0.0°
	Glass	6.55	97.1°	-11.5	1.0°
	Quartz	6.85	91.9°	-13.9	1.0°
8.5	FR-4	6.75	95.3°	-12.7	1.0°
	Glass	6.49	100.4°	-10.7	1.0°
	Quartz	6.98	91.1°	-15.0	0.0°

3.2. Quartz and Glass as the Radome of the PCB Patch Antenna

In this case, quartz and glass fiber were used as the radome of the designed PCB antenna. The radome shape is shown below (Figure 8). The thickness of the radome was selected as $t=2$ mm in the designed structure. The control of the performance of the produced radome was carried out only with the far-field radiation model.

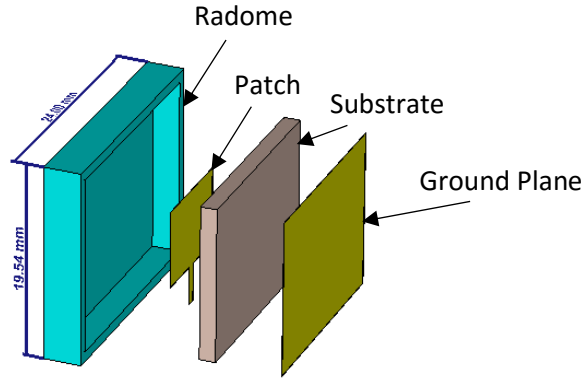


Figure 8. The schematic of the radome application on the designed PCB patch antenna.

The effect of the radome can be seen more clearly by examining the farfield radiation pattern of the designed antenna. In this case, the substrate was selected as FR-4 while changing the radome material between Quartz and Glass fiber. The farfield radiation patterns of the designed antenna for different radome materials were simulated for $f=7.5$ GHz, 8 GHz and 8.5 GHz, respectively. The results are given in the following figure (Figure 9). As seen in these figures the gain, main lobe direction and side lobe levels are almost the same for Quartz and Glass based radomes.

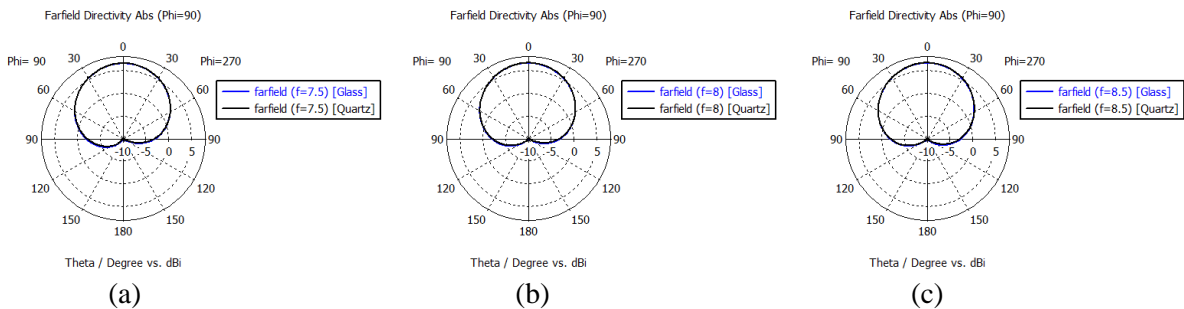


Figure 9. Farfield radiation pattern for quartz and glass substrates at $f=7.5, 8, 8.5$ GHz.

4. CONCLUSION

In conclusion, the uses of quartz fiber as an antenna radome and a dielectric substrate were investigated for a patch antenna designed to operate at $f=8$ GHz. The well-known FR-4 substrate was also compared to quartz and glass-made substrates. In both cases, the antenna performance parameters including antenna gain, half-power beamwidth, main lobe direction and front-to-back ratio (the ratio between the main lobe and back lobe of the radiation pattern) were examined. In both cases, it was found that the use of quartz and glass fiber as the substrate and radome material shifts the operating frequency while it does not change the antenna radiation parameters significantly. The highest change was observed in

the HPBW of the antenna up to 10° which can be used in application areas requiring sensitive coverage area. From this perspective, it was concluded that the electromagnetic performance of an antenna can be adjusted using these materials as radome and/or antenna substrate depending on the application type by also considering the environmental performances of the Quartz and Glass fiber reinforced materials.

CONFLICT OF INTEREST

The author stated that there are no conflicts of interest regarding the publication of this article.

REFERENCES



- [1] Wu Y, Xiao Y, Zou C, Sha X, Gao L, Li S. High-temperature resistance and wave-transmitting quartz-fibre/polyimide composite. *Plast Rubber Compos*, 2022; 51(9): 489-496.
- [2] Li J, Wang Y, Zhao W, Xu P, Wang T, Kong J. High-performance quartz fiber/polysilazane and epoxy-modified cyanate ester microwave-transparent composites. *Adv Compos Mater*, 2022; 5: 1830-1840.
- [3] Yang L, Jia J, Sun Y, Kong Z, Wang Y, Liu B, Na T, Yu G, Meng Z, Meng F. Effect of ultra-low expansion quartz glass layer on the enhancement performance of quartz optical fiber. *J Phys Conf Ser*, 2021; 2044: 012031.
- [4] Yang B, Li Y, Liu J, Li Y, Jin C, Li H. Influence of quartz fiber on electromagnetic wave transmission properties of high-alumina cement paste. *Front Mater* 2021; 9: 893927.
- [5] Wang H, Quan X, Yin L, Jin X, Pan Y, Wu C, Huang H, Hong C, Zhang X. Lightweight quartz fiber fabric reinforced phenolic aerogel with surface densified and graded structure for high temperature thermal protection. *Compos - A: Appl Sci Manuf*, 2021; 159: 107022.
- [6] Elseify L, Midani M, El-Badawy AA, Jawaid M. Natural fibers in the automotive industry. *Manufacturing Automotive Components from Sustainable Natural Fiber Composites*, 2021:1-10.
- [7] Wang Y. Application of quartz fiber reinforced composite material in high frequency radome. Duan, B., Umeda, K., Kim, Cw. (eds) *Proceedings of the Eighth Asia International Symposium on Mechatronics. Lecture Notes in Electrical Engineering*, 2022: 214-221.
- [8] Nguyen T, Nguyen T. Design and analysis of a quartz fiber reinforced polymer radome for a microsatellite communication system. *J Reinf Plast* 2016; 35(9): 667-680.
- [9] Fujimoto K, Ushijima K, Nakamura M, Murakami T Development of a quartz fiber reinforced epoxy radome. *Proceedings of the International Conference on Composite Materials*, 2001: 1-8.
- [10] Park J, Lee J, Park J. Development of a quartz fiber-reinforced polymer radome for millimeter-wave communication systems. *J Compos Mater*, 2018; 52(8): 1087-1095.
- [11] Dong J, Wang H, Liu W, Wang C. Design and experimental study of a radome with improved thermal stability. *Mater* 2019; 12(21): 3583.

- [12] Wang X, Zhang S, Ma J, Zhang H, Guo Y, Zhang W. Design and preparation of quartz fiber-reinforced glass-ceramic substrates for high-frequency electronic devices. *J Mater Sci Mater Electron* 2018; 29(3): 2424-2430.
- [13] Sze JY, Chen TH, Chen HM, Wu CH. Effect of substrate materials on antenna performance. *Appl Sci*, 2019; 9(10): 2114.
- [14] Dyck A et al. A 300 GHz microstrip multilayered antenna on quartz substrate. *International Workshop on Antenna Technology*, 2018: 1-3.
- [15] Xu J, Lin S, Huang Y, Wang Z. Design of patch antenna array with cavity structure on quartz glass for radar applications. *IEEE 9th International Symposium on Microwave, Antenna, Propagation and EMC Technologies for Wireless Communications*, 2022: 208-211.
- [16] Nicolson AM, Ross GF. Measurement of the Intrinsic Properties of Materials by Time-Domain Techniques. *IEEE Trans Instrum Meas*, 1970; 19: 377–382.
- [17] Weir WB. Automatic measurement of complex dielectric constant and permeability at microwave frequencies. *Proc. IEEE*, 1974; 62: 33–36.
- [18] Kabacik P, Bialkowski ME. The temperature dependence of substrate parameters and their effect on microstrip antenna performance. *IEEE Transactions on Antennas and Propagation*, 1999; 47(6): 1042-1049.



RESEARCH ARTICLE

ASYMPTOTIC ANALYSIS OF ACOUSTIC GREEN'S FUNCTIONS

Hazel YÜCEL ^{1,*} , Yağmur Ece UÇAR ² 

¹ Department of Computer Engineering, Başkent University, Ankara, Turkey

² Department of Mathematics, Eskişehir Technical University, Eskişehir, Turkey

ABSTRACT

An asymptotic expansion of layered Green's function is examination in a spatial domain and parametric approach is proposed by determining a small parameter to derive the shortened form of Green's function for 3- and 4-layered structures. For qualitative testing and comparison of the exact Green's function and asymptotic shortened Green's functions associated with the measurement and source point in the same layer, we performed numerical calculations.

Keywords: Green's function, Layered media, Parametric analysis, Asymptotic approach

1. INTRODUCTION

In acoustic imaging, the measured waves are converted to image using certain algorithms commonly involving the Green's functions [1,3]. Considering the layered acoustic environment, which includes different acoustical and physical parameters, the layered Green's functions involving infinite integrals with highly oscillatory and slowly attenuating integrands must be calculated. [4,5]. In [6], an out-of-plane analysis of a layered elastic plate using asymptotic expansions are investigated whereas low-frequency analysis of multi-component rods are considered employing an asymptotic procedure together with a multiparametric analysis of the problem parameters in [7]. In both works, approximate analytical solutions were obtained and dispersion equations, which are difficult or impossible to calculate analytically due to the complicated functions they contain, are expressed through simplified polynomials resulting in much simpler analysis of the considered problems. In [8] a parametric analysis was performed to evaluate the effect of layer densities on the Green's function.

It is therefore possible to formulate the mathematical model of the problem considered in this paper through the physical and acoustic parameters in an understandable way whereby a multiparametric approach may be utilized after a successful application of an asymptotic expansion to the layered Green's function in a spatial domain [9].

In this study, asymptotic expansions of each term in the coefficients of acoustic layer Green's functions used in the solution of the photoacoustic wave equation are obtained for 3 and 4 layers in spatial domain, and a parametric analysis is carried out according to medium velocities for a 3 layered media. Numerical comparisons of exact Green's functions and Green's functions obtained through the asymptotic expansions of coefficients are given. Using these expansions in photoacoustic imaging can both provide a physical interpretation of the problem and speed up the calculation time.

2. STATEMENT OF THE PROBLEM

The medium is modeled as a layered planar medium consisting of 3 and 4 layers, respectively, each of which is homogeneous with different acoustic properties from others, extending infinitely in the transverse direction, subject to continuity conditions on the boundary of layers and the wave propagation is represented by layered Green's functions.

Assuming that the source and measurement locations are in the same layer, $r = (x, z)$ and $r' = (x', z')$, respectively, acoustic layered Green's functions are expressed as follows [8]:

$$G(r, r') = \int_0^\infty \frac{\cos(k_x(x - x'))}{k_{z1}} (e^{(-k_{z1}|z-z'|)} + R_N e^{(-k_{z1}|z+z'|)}) dk_x \quad N = 3,4 \quad (1)$$

where R_N denotes transmission and reflection coefficients. Equations $k_x^2 = k_{zi}^2 + k_i^2$ are valid and the variables of this equations are wave numbers ($i = 1, 2, 3, 4$).

The initial condition at $t = 0$, and continuity conditions on the boundary are expressed as

$$p_0 = p(r, t = 0), \quad \frac{\partial p(r, t = 0)}{\partial t} = 0 \quad (2)$$

$$\lim_{r \rightarrow S_m^-} p(r, t) = \lim_{r \rightarrow S_m^+} p(r, t) \quad (3)$$

and

$$\lim_{r \rightarrow S_m^-} \frac{1}{\rho_m} \frac{\partial p(r, t)}{\partial \mathbf{n}} = \lim_{r \rightarrow S_m^+} \frac{1}{\rho_{m+1}} \frac{\partial p(r, t)}{\partial \mathbf{n}}, \quad m = 1, 2, 3, 4 \quad (4)$$

Here, $p(r, t)$ is the acoustic wave function at position r and time t . S_m denotes the surface of the m^{th} boundary. ρ_m and ρ_{m+1} are densities of the layers m and $m + 1$, respectively. Also, since the geometry of the problem is taken as unbounded from above and below, thus, radiation conditions are valid at infinity.

To simplify the analysis, we introduce a dimensionless spatial wave number K_x , and the spectral frequency Ω given by

$$\Omega = \frac{\omega h_2}{c_1}, \quad K_x = k_x h_2, \quad (5)$$

where h_2 is the thickness between the first and second layers. We introduce the dimensionless acoustic velocity and density ratios as

$$\chi_{1m} = \frac{c_1}{c_m}, \quad \rho_{nm} = \frac{\rho_n}{\rho_m}, \quad m = 2, 3, 4; n = m - 1. \quad (6)$$

Using non-dimensional parameters, the wave numbers appearing in eqn.(1) are rewritten as

$$K_{z1} = \begin{cases} -i \sqrt{\Omega^2 - K_x^2}, & |\Omega| > |K_x| \\ \sqrt{K_x^2 - \Omega^2}, & |K_x| > |\Omega| \end{cases}, \quad (7)$$

$$K_{zm} = \begin{cases} -i \sqrt{\Omega^2 \chi_{1m}^2 - K_x^2}, & |\Omega \chi_{1m}| > |K_x| \\ \sqrt{K_x^2 - \chi_{1m}^2 \Omega^2}, & |K_x| > |\chi_{1m} \Omega| \end{cases}, \quad m = 2, 3, 4. \quad (8)$$

2.1. 3- LAYERED MEDIA

For a 3 layer media, the geometry of problem is given in following figure.

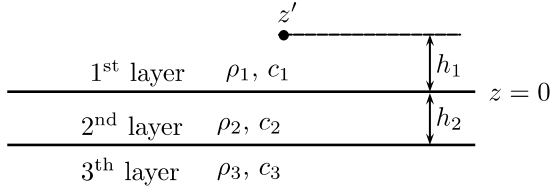


Figure 1. Geometry of 3-layer media.

Here, ρ_i and c_i are the density and velocity of medium, respectively ($i = 1, 2, 3$). h_1 is the distance between the source and first layer, h_2 is the thickness between layers and the source is located the first layer at z' . The Green's function, in this case, takes the form

$$G_1 = \frac{1}{2\pi} \int_0^{\infty} \left(e^{-k_{z_1}|z-z'|} + R_3 e^{-k_{z_1}|z+z'|} \right) \frac{\cos(k_x(x-x'))}{k_{z_1}} dk_x, \quad z \in \text{Medium 1.} \quad (9)$$

The coefficients R_3 can be written as a piecewise function for the first, second and third regions of integration, as $K_x < \Omega$, $\Omega - \varepsilon < K_x < \Omega + \varepsilon$ and $K_x > \Omega$, respectively. For these regions, the coefficient of layered Green's function is represented as

$$R_3 = \begin{cases} R_3^{(I)}, & K_x < \Omega \\ R_3^{(II)}, & K_x \in (\Omega - \varepsilon, \Omega + \varepsilon), \\ R_3^{(III)}, & \Omega < K_x \end{cases} \quad (10)$$

$$R_3 = \frac{E_3}{\Delta_3}, \quad (11)$$

where E_3 and Δ_3 are calculated using boundary conditions on the interfaces of layers which includes the physical and acoustic parameters of the medium. The coefficient of Green's function given in equation (10) may be expanded in the small variables, $\frac{K_x}{\Omega} \ll 1$ and $\frac{\Omega}{K_x} \ll 1$, in the 1st and 3rd regions, respectively. At the branch points, the coefficient of $R_3^{(II)}$ is calculated numerically since an asymptotic expansion around these points is not visible.

When the source and measurement points are located in the first layer as depicted in Figure 1, the coefficient (R_3) of the Green's function is given by

$$\frac{E_3}{\Delta_3} = \frac{-\cosh(K_{z_2}) K_{z_2} (\rho_{13} K_{z_3} + K_{z_1}) + \sinh(K_{z_2}) (\rho_{23} K_{z_1} K_{z_3} + \rho_{12} K_{z_2}^2)}{\cosh(K_{z_2}) K_{z_2} (\rho_{13} K_{z_3} - K_{z_1}) + \sinh(K_{z_2}) (\rho_{23} K_{z_1} K_{z_3} - \rho_{12} K_{z_2}^2)}. \quad (12)$$

On expanding each term of the ratio $\frac{E_3}{\Delta_3}$ in an asymptotic series, equation (12) maybe reduced to a polynomial. As an example, the series expansions of the following two terms are given in the first region:

$$\cosh(K_{z_2}) = 1 + \frac{K_{z_2}^2}{2!} + \dots = 1 + \frac{K_x^2 - \Omega^2}{2} + \dots = \Omega^2 \left(\frac{1}{\Omega^2} + \frac{K_x^2}{2\Omega^2} - \frac{1}{2} \right) + O\left(\frac{K_x^4}{\Omega^4}\right), \quad (13)$$

$$K_{z_3} = \sqrt{K_x^2 - \chi_{13}^2 \Omega^2} = i\chi_{13}\Omega \sqrt{1 - \frac{K_x^2}{\chi_{13}^2 \Omega^2}} = i\chi_{13}\Omega \left(1 - \frac{K_x^2}{2\chi_{13}^2 \Omega^2} + O\left(\frac{K_x^4}{\Omega^4}\right) \right). \quad (14)$$

Assuming $\Omega \gg 1$, asymptotic order of each term in (12) can be decided on expanding the expression $\frac{a\Omega+b}{c\Omega+d}$ where the constants a, b, c and d can be easily determined from (12).

Case 1:

In this case, asymptotic expansion of all terms of the coefficient of the Green’s function is carried out by assuming that $\frac{K_x}{\Omega} \ll 1$.

If the asymptotic expressions of all terms contained in the coefficient of Green’s function given by equation (12) are written, similar to the equations (13) and (14), the first two terms of the numerator E_3 and denominator Δ_3 are obtained for the first region ($\Omega \gg K_x$), respectively as follows:

$$\begin{aligned}
 E_{3(1^{st}region)} \sim & -i\rho_{13}\chi_{13}\Omega^5\frac{\chi_{12}^4}{2} - i\Omega^5\frac{\chi_{12}^4}{2} + \chi_{12}^2\chi_{13}\rho_{23}\Omega^4 + \chi_{12}^4\rho_{12}\Omega^4 \\
 & + \frac{K_x^2}{\Omega^2}\left(i\rho_{13}\chi_{13}\Omega^5\left(\chi_{12}^2 + \frac{\chi_{12}^4}{4\chi_{13}^2} - \frac{1}{\Omega^2} - \frac{\chi_{12}^2}{2\Omega^2}\right)\right) \\
 & + i\Omega^5\left(\frac{\chi_{12}^2}{4} + \frac{\chi_{12}^4}{4} - \frac{1}{\Omega^2} - \frac{\chi_{12}^2}{2\Omega^2}\right) - \chi_{13}\rho_{23}\Omega^4\left(1 + \frac{\chi_{12}^2}{2\chi_{13}^2} + \frac{\chi_{12}^2}{2}\right) \\
 & - 2\rho_{12}\Omega^4\chi_{12}^2),
 \end{aligned} \tag{15}$$

$$\begin{aligned}
 \Delta_{3(1^{st}region)} \sim & i\rho_{13}\chi_{13}\Omega^5\frac{\chi_{12}^4}{2} - i\Omega^5\frac{\chi_{12}^4}{2} + \chi_{12}^2\chi_{13}\rho_{23}\Omega^4 - \chi_{12}^4\rho_{12}\Omega^4 \\
 & - \frac{K_x^2}{\Omega^2}\left(i\rho_{13}\chi_{13}\Omega^5\left(\chi_{12}^2 + \frac{\chi_{12}^4}{4\chi_{13}^2} - \frac{1}{\Omega^2} - \frac{\chi_{12}^2}{2\Omega^2}\right)\right) \\
 & + i\Omega^5\left(\frac{\chi_{12}^2}{4} + \frac{\chi_{12}^4}{4} - \frac{1}{\Omega^2} - \frac{\chi_{12}^2}{2\Omega^2}\right) - \chi_{13}\rho_{23}\Omega^4\left(1 + \frac{\chi_{12}^2}{2\chi_{13}^2} + \frac{\chi_{12}^2}{2}\right) \\
 & + 2\rho_{12}\Omega^4\chi_{12}^2).
 \end{aligned} \tag{16}$$

Substituting equations (15) and (16) in (12), we obtain the coefficient R_3 for the first region as follows

$$R_3^{(I)} = \frac{\Omega^5\left(1+O\left(\frac{K_x^2}{\Omega^2}\right)\right) - \Omega^4\left(1+O\left(\frac{K_x^2}{\Omega^2}\right)\right)}{\Omega^5\left(1+O\left(\frac{K_x^2}{\Omega^2}\right)\right) - \Omega^4\left(1+O\left(\frac{K_x^2}{\Omega^2}\right)\right)}. \tag{17}$$

Since the term Ω^5 is the dominant term in the first region, the coefficient $R_{3(1^{st}region)}$ may be written in the shortened form as

$$R_3^{(I)} = \frac{-i\rho_{13}\chi_{13}\Omega^5\frac{\chi_{12}^4}{2} - i\Omega^5\frac{\chi_{12}^4}{2} + \frac{K_x^2}{\Omega^2}\left(i\rho_{13}\chi_{13}\Omega^5\left(\chi_{12}^2 + \frac{\chi_{12}^4}{4\chi_{13}^2} - \frac{1}{\Omega^2} - \frac{\chi_{12}^2}{2\Omega^2}\right) + i\Omega^5\left(\frac{\chi_{12}^2}{4} + \frac{\chi_{12}^4}{4} - \frac{1}{\Omega^2} - \frac{\chi_{12}^2}{2\Omega^2}\right)\right)}{i\rho_{13}\chi_{13}\Omega^5\frac{\chi_{12}^4}{2} - i\Omega^5\frac{\chi_{12}^4}{2} + \frac{K_x^2}{\Omega^2}\left(i\rho_{13}\chi_{13}\Omega^5\left(\chi_{12}^2 + \frac{\chi_{12}^4}{4\chi_{13}^2} - \frac{1}{\Omega^2} - \frac{\chi_{12}^2}{2\Omega^2}\right) + i\Omega^5\left(\frac{\chi_{12}^2}{4} + \frac{\chi_{12}^4}{4} - \frac{1}{\Omega^2} - \frac{\chi_{12}^2}{2\Omega^2}\right)\right)}. \tag{18}$$

Comparisons of exact Green's function and asymptotic Green's function and the relative error are given in the following numerical implementations. In all our computations, we have considered the temporal frequency as 1 MHz and the wavelength as $\lambda = 16 \times 10^{-4} m$. Densities of medium are $\rho_1 = 500 \text{ gr/cm}^3, \rho_2 = 700 \text{ gr/cm}^3, \rho_3 = 600 \text{ gr/cm}^3$ respectively, and velocities of medium are $c_1 = 1600 \text{ m/sec}, c_2 = 1000 \text{ m/sec}, c_3 = 500 \text{ m/sec}$, respectively. Layer thickness is taken as $|h_2| =$

3λ. The source is located at $(x', z') = (2λ, 2λ)$ and the measurement point is fixed at $2λ$ in the x -coordinate but in the z -axis the measurement point is varied from $2.001λ$ to $11λ$.

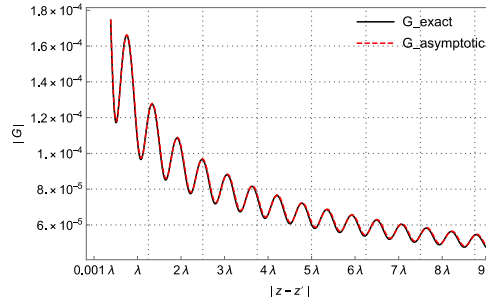


Figure 2. Comparison of exact and asymptotic Green's function for a three layered media for the first region

It can be seen from Figure 2, that there is a notable overlap between the absolute value of exact and asymptotic Green's function for all points both in the near and far fields in the first region.

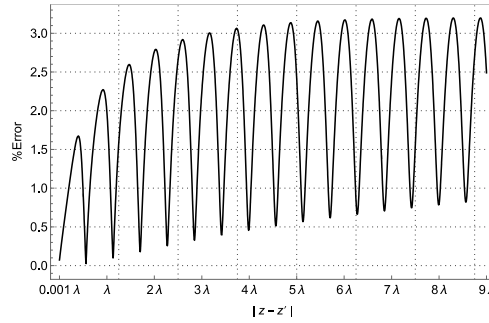


Figure 3. Relative error of exact and asymptotic Green's function for a three-layered media for the first region

The relative error, presented in Figure 3, between exact and asymptotic Green's function is limited to about 3% for all distances.

Case 2:

By taking $\frac{\Omega}{K_x}$ as the small parameter, similar calculations for R_3 can be repeated for the third region giving the numerator E_3 and the denominator Δ_3 of coefficients R_3 by

$$E_{3(3^{rd}region)} = \left(1 - \frac{\Omega^2}{2K_x^2} + \frac{1}{24} \frac{\Omega^4}{K_x^4}\right) - \rho_{13} \left(1 - \frac{\chi_{13}^2}{2} \frac{\Omega^2}{2K_x^2} + \frac{\chi_{13}^4}{24} \frac{\Omega^4}{K_x^4}\right) - \rho_{12} + \rho_{23} + \frac{\Omega^2}{K_x^2} \left(\rho_{12}\chi_{12}^2 + \frac{\rho_{23}}{2} + \chi_{13}^2 \frac{\rho_{23}}{2}\right) + \frac{\Omega^4}{K_x^4} \left(\frac{\rho_{23}}{24} + \chi_{13}^2 \frac{\rho_{23}}{4} + \chi_{13}^4 \frac{\rho_{23}}{24}\right), \quad (19)$$

$$\Delta_{3(3^{rd}region)} = \left(1 - \frac{\Omega^2}{2K_x^2} + \frac{1}{24} \frac{\Omega^4}{K_x^4}\right) + \rho_{13} \left(1 - \frac{\chi_{13}^2}{2} \frac{\Omega^2}{2K_x^2} + \frac{\chi_{13}^4}{24} \frac{\Omega^4}{K_x^4}\right) + \rho_{12} + \rho_{23} + \frac{\Omega^2}{K_x^2} \left(-\rho_{12}\chi_{12}^2 + \frac{\rho_{23}}{2} + \chi_{13}^2 \frac{\rho_{23}}{2}\right) + \frac{\Omega^4}{K_x^4} \left(\frac{\rho_{23}}{24} + \chi_{13}^2 \frac{\rho_{23}}{4} + \chi_{13}^4 \frac{\rho_{23}}{24}\right). \quad (20)$$

The coefficient of Green's function, therefore, takes the form

$$R_3^{(III)} = \frac{K_x^5 \left(1 + O\left(\frac{\Omega^2}{K_x^2}\right)\right) + K_x^5 \left(1 + O\left(\frac{\Omega^2}{K_x^2}\right)\right) - K_x^4 \left(1 + O\left(\frac{\Omega^2}{K_x^2}\right)\right) - K_x^4 \left(1 + O\left(\frac{\Omega^2}{K_x^2}\right)\right)}{K_x^5 \left(1 + O\left(\frac{\Omega^2}{K_x^2}\right)\right) - K_x^5 \left(1 + O\left(\frac{\Omega^2}{K_x^2}\right)\right) + K_x^4 \left(1 + O\left(\frac{\Omega^2}{K_x^2}\right)\right) - K_x^4 \left(1 + O\left(\frac{\Omega^2}{K_x^2}\right)\right)} \quad (21)$$

Since the variable K_x is much larger than the frequency Ω in this region, the coefficient $R_3^{(III)}$ can be approximately written as

$$R_3^{(III)} = \frac{\left(1 - \frac{\Omega^2}{2 K_x^2} + \frac{1}{24} \frac{\Omega^4}{K_x^4}\right) - \rho_{13} \left(1 - \frac{\chi_{13}^2}{2} \frac{\Omega^2}{2 K_x^2} + \frac{\chi_{13}^4}{24} \frac{\Omega^4}{K_x^4}\right)}{\left(1 - \frac{\Omega^2}{2 K_x^2} + \frac{1}{24} \frac{\Omega^4}{K_x^4}\right) + \rho_{13} \left(1 - \frac{\chi_{13}^2}{2} \frac{\Omega^2}{2 K_x^2} + \frac{\chi_{13}^4}{24} \frac{\Omega^4}{K_x^4}\right)} \quad (22)$$

The exact and asymptotic Green's functions are compared in the third region in Fig.4.

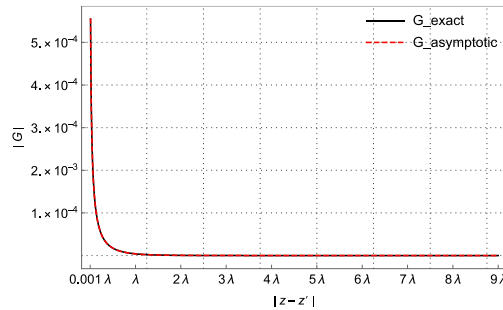


Figure 4. Comparison of exact and asymptotic Green's functions for a three layered media for the third region

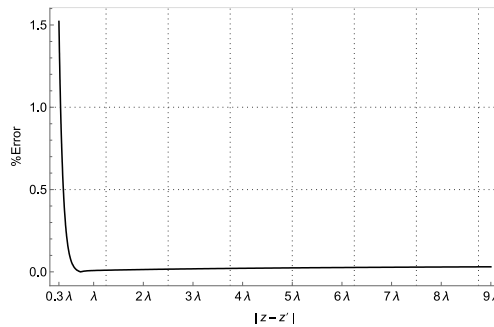


Figure 5. Relative error of exact and asymptotic Green's function for a three-layered media for the third region

As seen in Figure 5, the error stays the same for all distances between the source and the measuring point.

2.2. Parametric Analysis For a 3-Layered Media

The order of magnitude of the ratios of the layer velocities allows us to use parametric analysis in asymptotic expansions of the coefficient of Green's function given by Eqn. (18) and (22) in the first and third regions, respectively. By applying parametric analysis, the smallness of nondimensional quantities χ_{mn} ($m, n = 1, 2, 3$) permit certain terms to be eliminated in the asymptotic expansion of coefficient and it enables the speed of calculations within acceptable accuracy.

For the first region, let us take the configuration where the velocities are in increasing order of magnitude, that is, $c_3 \ll c_2 \ll c_1$. In this case, the term $1/\chi_{13}$ ($1/\chi_{13} = \ll 1$), is the smallest term among the terms given in Eqn. (15) and (16). If we neglect the smallest terms in the coefficient R_3 which is given by Eqn. (15) and (16), we write the shortened asymptotic coefficient as

$$R_{shortened}^{(I)} = \frac{-i\rho_{13}\chi_{13}\Omega^5 \frac{\chi_{12}^4}{2} - i\Omega^5 \frac{\chi_{12}^4}{2} + \frac{K_x^2}{\Omega^2} \left(i\rho_{13}\chi_{13}\Omega^5 \left(\chi_{12}^2 - \frac{1}{\Omega^2} - \frac{\chi_{12}^2}{2\Omega^2} \right) + i\Omega^5 \left(\frac{\chi_{12}^2}{4} + \frac{\chi_{12}^4}{4} - \frac{1}{\Omega^2} - \frac{\chi_{12}^2}{2\Omega^2} \right) \right)}{i\rho_{13}\chi_{13}\Omega^5 \frac{\chi_{12}^4}{2} - i\Omega^5 \frac{\chi_{12}^4}{2} + \frac{K_x^2}{\Omega^2} \left(i\rho_{13}\chi_{13}\Omega^5 \left(\chi_{12}^2 - \frac{1}{\Omega^2} - \frac{\chi_{12}^2}{2\Omega^2} \right) + i\Omega^5 \left(\frac{\chi_{12}^2}{4} + \frac{\chi_{12}^4}{4} - \frac{1}{\Omega^2} - \frac{\chi_{12}^2}{2\Omega^2} \right) \right)} \quad (23)$$

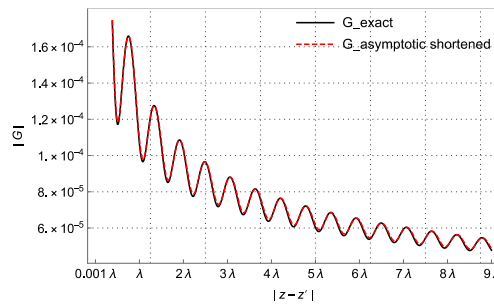


Figure 6. Comparison of exact and asymptotic shortened Green’s functions for a three layered media for the first region.

In Figure 6, the absolute values of exact Green’s function and the asymptotic shortened form of Green’s function is compared in terms of distance $|z - z'|$. In this calculation, acoustical and physical parameters are taken as the same numerical values above, except for the sound velocities. Sound velocities are taken as $c_1 = 1600 \text{ m/sec}$, $c_2 = 1000 \text{ m/sec}$, $c_3 = 500 \text{ m/sec}$. Thus the ratio of velocities $1/\chi_{13} = 0.3$ and there is a significant coincidence between the functions as is depicted in Figure 6.

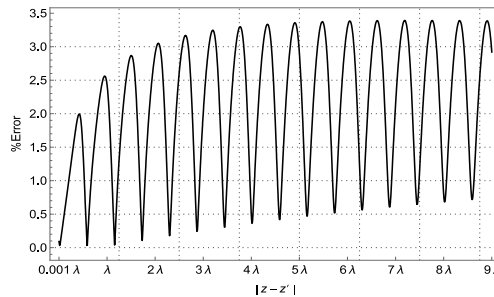


Figure 7. Relative error of exact and asymptotic shortened Green’s function for the first region.

The graph of the relative error between exact and asymptotic shortened Green’s functions is shown in Figure7 which is bounded by 3.5 % for all distance ranges. For the third region, the order of velocities is considered as $c_1 \ll c_2 \ll c_3$ where $c_1 = 500 \text{ m/sec}$, $c_2 = 700 \text{ m/sec}$, $c_3 = 1400 \text{ m/sec}$. In this case, the term $\chi_{13} = c_1/c_3 \ll 1$ is the smallest term. Then, the terms χ_{13} are neglected in the coefficient $R_3^{(III)}$ expressed by eqn (22), and asymptotic shortened Green’s function’s coefficient is obtain as

$$R_{Shortened}^{(III)} = \frac{\left(1 - \frac{\Omega^2}{2K_x^2} + \frac{1}{24} \frac{\Omega^4}{K_x^4}\right) - \rho_{13}}{\left(1 - \frac{\Omega^2}{2K_x^2} + \frac{1}{24} \frac{\Omega^4}{K_x^4}\right) + \rho_{13}} \quad (24)$$

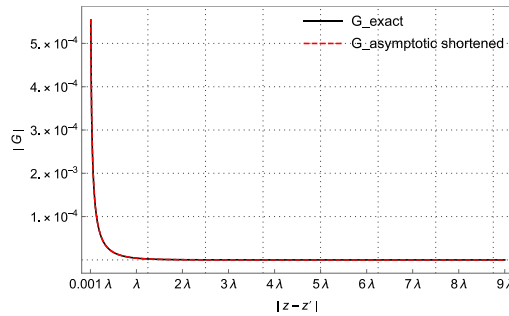


Figure 8. Comparison of exact and asymptotic shortened Green’s functions for a three-layered media for the third region.

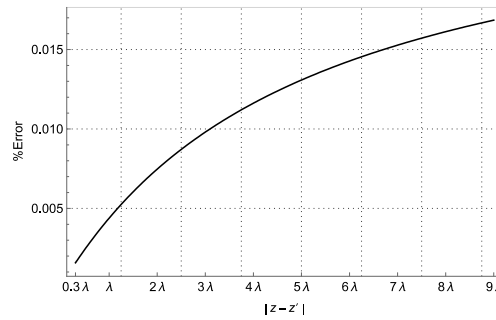


Figure 9. Relative error of exact and asymptotic shortened Green’s function for a three-layered media for the third region.

It can be seen from Figures 8 and 9 that the compatibility between exact and asymptotic shortened Green’s functions is quite favorable in the third region.

Table 1. CPU time in seconds per point for distance $|z - z'| = 3\lambda$ for exact Green’s, asymptotic Green’s and asymptotic shortened Green’s function in the first region for 3-layered media.

Ratio of velocities	Exact Green’s Function	Asymptotic Green’s Function	Asymptotic Shortened Green’s Function
$1/\chi_{13} = 0.3$	0,000501383	0,000457215	0,000456886

Therefore, we can say that the computation times are very close in this region. Hence, the analysis of the computational times is done only in the first region by Table 1. It is clearly observed that the CPU times decrease in case of asymptotic and asymptotic shortened form of Green’s functions which proves to be an important advantage in imaging algorithms where the Green’s function is required to be computed recursively.

3. 4-LAYERED MEDIA

For a 4-layered media, the geometry of problem is given in the following figure.

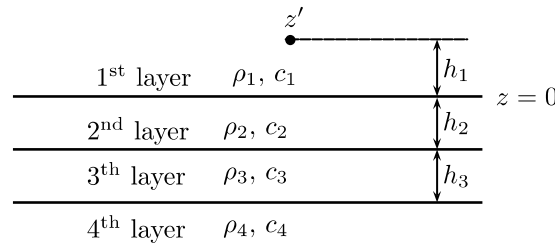


Figure 11. Geometry of 4-layered media.

$r = (x', z')$ and $r = (x, z)$ represent source and measurement locations, c_1, c_2, c_3 and c_4 are acoustic wave speeds, and ρ_1, ρ_2, ρ_3 and ρ_4 are densities of layers 1, 2, 3 and 4, respectively. The coefficient appearing in equation (1), in this setting, is given by

$$R_4 = \frac{E_4}{\Delta_4} \tag{25}$$

where

$$E_4 = K_{z_1} \cosh K_{z_2} \left\{ K_{z_3} \cosh \left(K_{z_3} (1 - h_{32}) \right) (K_{z_1} - \rho_{14} K_{z_4}) + \sinh \left(K_{z_3} (1 - h_{32}) \right) (\rho_{34} K_{z_1} K_{z_4} - \rho_{13} K_{z_3}^2) \right\} + \sinh K_{z_2} \left\{ K_{z_3} \cosh \left((1 - h_{32}) K_{z_3} \right) (\rho_{12} K_{z_2}^2 - \rho_{24} K_{z_1} K_{z_4}) + \sinh \left((1 - h_{32}) K_{z_3} \right) (K_{z_2}^2 K_{z_4} \rho_{12} \rho_{34} - \rho_{23} K_{z_1} K_{z_3}^2) \right\} \tag{26}$$

and

$$\Delta_4 = K_{z_2} \cosh K_{z_2} \left\{ K_{z_3} \cosh \left(K_{z_3} (1 - h_{32}) \right) (K_{z_1} + \rho_{14} K_{z_4}) + \sinh \left(K_{z_3} (1 - h_{32}) \right) (\rho_{34} K_{z_1} K_{z_4} + \rho_{13} K_{z_3}^2) \right\} + \sinh K_{z_2} \left\{ K_{z_3} \cosh \left((1 - h_{32}) K_{z_3} \right) (\rho_{12} K_{z_2}^2 + \rho_{24} K_{z_1} K_{z_4}) + \sinh \left((1 - h_{32}) K_{z_3} \right) (K_{z_2}^2 K_{z_4} \rho_{12} \rho_{34} + \rho_{23} K_{z_1} K_{z_3}^2) \right\}. \tag{27}$$

Similar to R_3 , the coefficient R_4 can also be written as a piecewise function for the first, second and third regions of integration, as $K_x < \Omega$, $\Omega - \varepsilon < K_x < \Omega + \varepsilon$ and $K_x > \Omega$, respectively and the coefficient of layered Green’s function is written as

$$R_4 = \begin{cases} R_4^{(I)}, & K_x < \Omega \\ R_4^{(II)}, & K_x \in (\Omega - \varepsilon, \Omega + \varepsilon) \\ R_4^{(III)}, & \Omega < K_x. \end{cases} \tag{28}$$

In the 4-layered media, we take into account the leading terms of series expansion of sinh and cosh functions appearing in the numerator and denominator in Eqn. (26)-(27) as follows:

$$\cosh K_{z_i} \sim 1 \text{ and } \sinh K_{z_i} \sim K_{z_i} \tag{29}$$

Unlike layer 3, performing the asymptotic expansion of the coefficient in layer 4, we take the first terms of the expansions of the hyperbolic functions in (26)-(27) and the first 3 terms of the expansions of the wave numbers defined in terms of square root functions in the first and third integration regions, respectively. We analyze it in two cases.

Case 1

According to the order of the variable of frequency, the coefficient of Green’s function can be written in the first region briefly as

$$R_4^{(I)} = \frac{c_1\Omega + c_2\Omega^2 + (1 - h_{32})c_3\Omega^2 + (1 - h_{32})c_4\Omega^3}{d_1\Omega + d_2\Omega^2 + (1 - h_{32})d_3\Omega^2 + (1 - h_{32})d_3\Omega^3} \quad (30)$$

where the constants c_1, c_2, c_3, c_4 and d_1, d_2, d_3, d_4 can be easily determined from equations (26) and (27) which are given by eqns. (A1) and (A2) in appendix A.

For $\Omega \gg 1$, equation (30) takes the form

$$R_4^{(I)} \sim \frac{c_4 + (c_2 + c_3)\frac{1}{\Omega}}{d_4 + (d_2 + d_3)\frac{1}{\Omega}} \quad (31)$$

We then can express equation (31) asymptotically as

$$R_4^{(I)} \sim \frac{1}{d_4} \left(c_4 + \frac{(c_2 + c_3)1}{\Omega} \right) \left(1 - \frac{(d_2 + d_3)1}{d_4\Omega} \right) + \frac{c_4}{d_4} \left(\frac{d_2 + d_3}{d_4} \right)^2 \left(\frac{1}{\Omega} \right)^2 \quad (32)$$

Here, the coefficients c_i and d_i include the square root functions. When expanding the asymptotic series of root functions, terms of order up to six $\left(\frac{K_x^6}{\Omega^6}\right)$ should be kept to reduce the relative error between the exact coefficient of the Green's function and its asymptotic expression. The asymptotic expansion of coefficient is given by eqn. (A3) presented in appendix A.

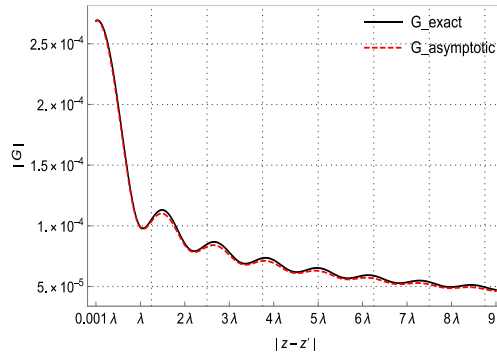


Figure 12. Comparison of exact and asymptotic shortened Green’s functions for a four layered media for the first region.

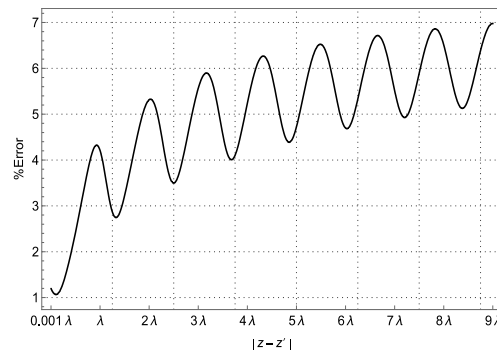


Figure 13. Relative error of exact and asymptotic shortened Green’s function for a three-layered media for the first region.

Figures 12 and 13 illustrate that the exact and asymptotic Green's functions match quite well in the first region demonstrating the validity of the considered approach.

Case 2:

The calculation performed above for R_4 in the first region can be similarly repeated for the third region. It is clear that the term $\frac{\Omega}{K_x}$ should be taken as the small parameter in this region. Since this region is semi-infinite, it will be sufficient to expand the square root function up to 4th-order. For $\Omega \ll K_x$, we have

$$R_4^{(III)} \sim \frac{1}{d_4} \left(c_4 + \frac{c_2 + c_3}{K_x} \right) \left(1 - \frac{d_2 + d_3}{d_4} \right) \frac{1}{K_x} + \frac{c_4}{d_4} \left(\frac{d_2 + d_3}{d_4} \right)^2 \frac{1}{K_x^2} \quad (33)$$

which is given explicitly in appendix A by eqn. (A4).

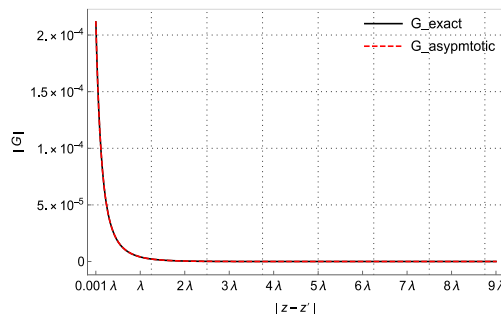


Figure 14. Comparison of exact and asymptotic shortened Green’s functions for a four layered media for the third region.

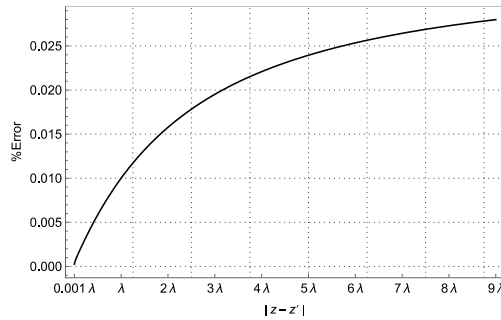


Figure 15. Relative error of exact and asymptotic shortened Green’s function for a four-layered media for the third region.

Figure 14 demonstrates the numerical comparison with the exact and asymptotic shortened Green’s functions while Figure 15 shows the relative error between the exact and asymptotic shortened Green’s functions for four layered media for the third region.

Table 2. CPU time in seconds per point for distance $|z - z'| = 3\lambda$ for exact Green’s and asymptotic Green’s function in the first region for 4 layered media.

Exact Green’s Function	Asymptotic Green’s Function
0,00007509	0,00003565

It is seen that from Table 2 the computation time of the asymptotic Green's function is quite short.

5. CONCLUSION

Asymptotic series expansions for the reflection coefficient (R_n) of the component of the acoustic Green's function obtained for the 3- and 4-layer geometry, see eqns. (18), (22), (32) and (33), with the source and the observation points in the first region, are performed by dividing the integration region according to the temporal frequency (Ω) and spatial frequency (K_x). Since the terms of the coefficients are written as polynomials on expanding the asymptotic series with respect to the regions containing the acoustic velocities of the layers, a parametric analysis is performed according to the ratios of the acoustic velocities. Green's functions written in polynomial form over the regions are analyzed and the leading terms are retained, and the next order terms (the lowest order term) are neglected. The relative errors between the exact Green's function and the Green's functions analyzed parametrically according to the velocities are calculated. It is observed that, the parametrically and asymptotically analyzed Green's functions in the layered structure agree quite well with the exact ones and their relative errors are in acceptable range. Calculation time comparisons are also carried out between Green's function given in the shortened form and the full Green's function for layered structures by asymptotic and parametric analysis. From Table 1 and Table 2, it can be seen that the reduced computation time of asymptotic and shortened asymptotic Green's functions will save time in photoacoustic imaging algorithms particularly due to recursive calculations required by the Green's functions.

ACKNOWLEDGEMENTS

This work was supported by TUBITAK of Turkey through the ARDEB-1001 Program under Grant No. 119E624.

CONFLICT OF INTEREST

The authors stated that there are no conflicts of interest regarding the publication of this article.

AUTHORSHIP CONTRIBUTIONS

Autors' contributions are equal.

REFERENCES

- [1] Uzun B, Yücel H. An inverse source problem connected with thermoacoustic imaging in multi-layer planar medium. *Journal of Mathematical Imaging and Vision* 61 (2019): 874-884
- [2] Xu M, Wang LV. Universal back-projection algorithm for photoacoustic computed tomography. *Physical Review E*, 2005; 71(1), 016706.
- [3] Schoonover RW, Anastasio MA. Image reconstruction in photoacoustic tomography involving layered acoustic media. *JOSA A*, 2011; 28(6), 1114-1120.
- [4] DiNapoli FR, Deavenport RL. Theoretical and numerical Green's function field solution in a plane multilayered medium. *The Journal of the Acoustical Society of America*, 1980; 67(1), 92-105.
- [5] Dural G, Aksun MI. Closed-form Green's functions for general sources and stratified media. *IEEE transactions on microwave theory and techniques*, 1995;43(7), 1545-1552.

- [6] Kaplunov J, Prikazchikov D, Sergushova O. Multi-parametric analysis of the lowest natural frequencies of strongly inhomogeneous elastic rods. *Journal of Sound and Vibration*, 2016; 366, 264-276.
- [7] Kaplunov YD, Prikazchikova LAE. Low-frequency vibration modes of strongly inhomogeneous elastic laminates. *Известия Саратовского университета. Новая серия. Серия: Математика. Механика. Информатика*, 2018; 18(4), 447-457.
- [8] Özdemir Ö, Yücel H, Uçar YE, Erbaş B, Ege N. Green's functions for a layered high-contrast acoustic media. *The Journal of the Acoustical Society of America*, 2022; 151(6), 3676-3684.
- [9] Prikazchikova L, Aydın YE, Erbaş B, Kaplunov J. Asymptotic analysis of an anti-plane dynamic problem for a three-layered strongly inhomogeneous laminate. *Mathematics and Mechanics of Solids*, 2020; 25(1), 3-16.

APPENDIX A

$$\begin{aligned} c_1 &= K_{z_1} - \rho_{14}K_{z_4}, \\ c_2 &= \rho_{12}K_{z_2}^2 - \rho_{24}K_{z_1}K_{z_4}, \\ c_3 &= \rho_{34}K_{z_1}K_{z_4} - \rho_{13}K_{z_3}^2, \\ c_4 &= K_{z_2}^2K_{z_4}\rho_{12}\rho_{34} - \rho_{23}K_{z_1}K_{z_3}^2, \end{aligned} \quad (A1)$$

$$\begin{aligned} d_1 &= K_{z_1} + \rho_{14}K_{z_4}, \\ d_2 &= \rho_{12}K_{z_2}^2 + \rho_{24}K_{z_1}K_{z_4}, \\ d_3 &= \rho_{34}K_{z_1}K_{z_4} + \rho_{13}K_{z_3}^2, \\ d_4 &= K_{z_2}^2K_{z_4}\rho_{12}\rho_{34} + \rho_{23}K_{z_1}K_{z_3}^2. \end{aligned} \quad (A2)$$

$$\begin{aligned} R_4^{(l)} \sim & \left(8\chi_4^3 \left(-\chi_4(-1 + h_{32} + \rho_{23})\rho_{34} - (-1 + h_{32})\chi_3^2(\rho_{13} + i\rho_{23}\Omega) + \chi_2^2\rho_{12}(-1 - \right. \right. \\ & \left. \left. i(-1 + h_{32})\chi_4\rho_{34}\Omega) \right) + 4\mathbb{U}^2\chi_4^2 \left(\chi_4^2\rho_{34}(-1 + h_{32} + \rho_{23} - 2i\rho_{12}\Omega + 2ih_{32}\rho_{12}\Omega) + \right. \right. \\ & \left. \left. \rho_{34}(-1 + h_{32} + \rho_{23} - i\chi_2^2\rho_{12}\Omega + ih_{32}\chi_2^2\rho_{12}\Omega) + \chi_4 \left(2\rho_{12} + (-1 + h_{32})(2\rho_{23} + \right. \right. \right. \\ & \left. \left. \left. i(2 + \chi_3^2)\rho_{23}\Omega) \right) \right) + \mathbb{U}^4 \left(i(-1 + h_{32})(-4 + \chi_3^2)\chi_4^3\rho_{23}\Omega + \rho_{34} \left(-1 - \rho_{23} - \chi_4^4(1 + \right. \right. \\ & \left. \left. \rho_{23}) - i\chi_2^2\rho_{12}\Omega + 2\chi_4^2(1 + \rho_{23} + 2i\rho_{12}\Omega) + h_{32} \left(1 + \chi_4^4 + i\chi_2^2\rho_{12}\Omega + \chi_4^2(-2 - \right. \right. \right. \\ & \left. \left. \left. 4i\rho_{12}\Omega) \right) \right) \right) \left(\left(8\chi_4^3 \left(\chi_4(-1 + h_{32} + \rho_{23})\rho_{34} - (-1 + h_{32})\chi_3^2(\rho_{13} + i\rho_{23}\Omega) + \right. \right. \right. \\ & \left. \left. \left. \chi_2^2\rho_{12}(i + (-1 + h_{32})\chi_4\rho_{34}\Omega) \right) + 4\mathbb{U}^2\chi_4^2 \left(-\chi_4^2\rho_{34}(-1 + h_{32} + \rho_{23} - 2i\rho_{12}\Omega + \right. \right. \right. \\ & \left. \left. \left. 2ih_{32}\rho_{12}\Omega) - \rho_{34}(-1 + h_{32} + \rho_{23} - i\chi_2^2\rho_{12}\Omega + ih_{32}\chi_2^2\rho_{12}\Omega) + \chi_4 \left(2\rho_{12} + (-1 + \right. \right. \right. \\ & \left. \left. \left. h_{32})(2\rho_{23} + i(2 + \chi_3^2)\rho_{23}\Omega) \right) \right) + \mathbb{U}^4 \left(i(-1 + h_{32})(-4 + \chi_3^2)\chi_4^3\rho_{23}\Omega + \rho_{34} \left(1 - \rho_{23} - \right. \right. \right. \\ & \left. \left. \left. \chi_4^4(1 + \rho_{23}) - i\chi_2^2\rho_{12}\Omega + 2\chi_4^2(-2 + 2\rho_{23} + 2i\chi_2^2\rho_{12}\Omega) + h_{32} \left(-1 + \chi_4^4 + i\chi_2^2\rho_{12}\Omega + \right. \right. \right. \\ & \left. \left. \left. \chi_4^2(2 - 2i\chi_2^2\rho_{12}\Omega) \right) \right) \right) \right) / \left((-1 + h_{32})^2 \left(-8\chi_4^3(\chi_3^2\rho_{23} + \chi_2^2\chi_4\rho_{12}\rho_{34}) + \mathbb{U}^4 \left((-4 + \right. \right. \right. \end{aligned} \quad (A3)$$

$$\chi_3^2) \chi_4^3 \rho_{23} + \chi_2^2 \rho_{12} \rho_{34} - 4 \chi_4^2 \rho_{12} \rho_{34}) + 4 \mathbb{U}^4 \chi_4^2 \left(\left((2 + \chi_3^2) \chi_4 \rho_{23} + \chi_2^2 \rho_{12} \rho_{34} + 2 \chi_4^2 \rho_{12} \rho_{34} \right) \right)^2 \Omega^2 \right), \quad \mathbb{U}^2 = \frac{K^2}{\Omega^2}.$$

$$\begin{aligned} R_4^{(III)} \sim & ((-4(1 + (-1 + h_{32})\rho_{13} - K\rho_{23} - \rho_{24} + \rho_{34} - h_{32}\rho_{34} + K\rho_{12}\rho_{34}) + \\ & 2 \frac{\Omega^2}{K^2} (-K\rho_{23} + \kappa_3^2((-1 + h_{32})\rho_{13} - K\rho_{23}) - \rho_{24} - \kappa_4^2\rho_{24} + \rho_{34} - h_{32}\rho_{34} + \kappa_4^2\rho_{34} - \\ & h_{32}\kappa_4^2\rho_{34} + K \kappa_4^2\rho_{12}\rho_{34} + 2 \kappa_2^2(\rho_{12} + K\rho_{12}\rho_{34}) + \frac{\Omega^4}{K^4} (\kappa_4^2(\rho_{24} + (-1 + h_{32})\rho_{34}) + \\ & 2K(\kappa_3^2\rho_{23} - \kappa_2^2\kappa_4^2\rho_{12}\rho_{34}))) \left(-\frac{2\Omega^2}{K^2} (-K\rho_{23} + h_{32}K\rho_{23} - 2(-1 + h_{32})\kappa_3^2(\rho_{13} - K\rho_{23}) - \right. \\ & \rho_{24} - \kappa_4^2\rho_{24} + \rho_{23} - h_{32}\rho_{34} + \kappa_4^2\rho_{34} - h_{32}\kappa_4^2\rho_{34} - K\kappa_4^2\rho_{34}\rho_{12} + h_{32}K\kappa_4^2\rho_{12}\rho_{34} + \\ & 2\kappa_2^2\rho_{12}(-1 + (-1 + h_{32})K\rho_{34})) - 4 \left(+(-1 + h_{32}\rho_{13} + \rho_{24} - \rho_{34} + h_{32}\rho_{34} - (-1 + \right. \\ & h_{32})K(\rho_{23} + \rho_{12}\rho_{34})) + \frac{\Omega^4}{K^4} (-\kappa_4^2(\rho_{24} + (-1 + h_{32})\rho_{34}) + 2(-1 + h_{32})K(\kappa_3^2\rho_{23} + \\ & \kappa_2^2\kappa_4^2\rho_{12}\rho_{34}))) \left. \right) / (4(-1 + h_{32})^2 K^2 \left((-2 + \frac{\Omega^2}{K^2}) \left(-1 + \frac{\Omega^2}{K^2} \kappa_3^2 \right) \rho_{23} + \left(-1 + \right. \right. \\ & \left. \left. \frac{\Omega^2}{K^2} \kappa_2^2 \right) \left(-2 + \frac{\Omega^2}{K^2} \kappa_4^2 \right) \rho_{12}\rho_{34} \right)^2). \end{aligned} \tag{A4}$$



RESEARCH ARTICLE

USING INTUITIONISTIC FUZZY C-MEANS CLUSTERING ALGORITHMS TO MODEL
COVID-19 CASES FOR COUNTRIES IN THE WORLDWIDE

Nihal İNCE* , Sevil ŞENTÜRK¹ 

¹Department of Statistics, Faculty of Science, Eskişehir Technical University, Eskişehir, Turkey

ABSTRACT

Every day, the number of newly confirmed cases of coronavirus (COVID-19) rises in many countries. It is critical to adjust policies and plans in order to investigate the relationships between the distributions of the spread of this virus in other countries. During this study, the intuitionistic fuzzy c-means (IFCM) clustering method is used to compare and cluster the distributions of COVID-19 spread in 62 countries. Using the IFCM clustering algorithm, the study aims to cluster the countries that use environmental, economic, social, health, and related measurements that affect disease spread to implement policies that regulate disease spread. As a result, countries that have similar factors can take proactive measures to address the pandemic. The data are obtained for 62 countries, and six different feature variables (factors associated with the spread of COVID-19) are determined. The data are obtained for 62 countries, and six variables with different characteristics (linked to the spread of COVID-19) are identified. In this study, the IFCM clustering algorithm is used to determine the dynamic behavior of COVID-19 based on real-world data for multiple countries and Turkey around the world. Data analysis is performed through MATLAB 2018a and R programs. The clustering results revealed that the distribution of dissemination in Brazil, India, and the United States was nearly identical and distinct from that of the 59 other countries.

Keywords: Intuitionistic fuzzy sets, Fuzzy C-means clustering algorithm, COVID-19, Statistical analysis

1. INTRODUCTION

According to some sources, the world has been dealing with a massive epidemic of unprecedented proportions since December-November 2019. The epidemic is said to have occurred in late December 2019. After "Coronavirus Disease 2019 (COVID-19)" was stated, a new type of coronavirus, "Severe Acute Respiratory Syndrome Coronavirus 2 (SARS-CoV-2)", was defined, as SARS-CoV-2 causes a spectrum of disease. COVID-19 is expanding rapidly worldwide due to its high contagiousness. Since November or December 2019, according to some sources, the COVID-19 pandemic originated in Wuhan, the seventh largest city in China, from where it has spread and continues to spread throughout the world. On March 11, 2020, sometime after the COVID-19 pandemic outbreak, the World Health Organization (WHO) declared the outbreak an epidemic. The quick dissemination of the COVID-19 epidemic has aroused a lot of countries around the world to take strict measures to limit the free movement of their citizens. Taken the measures have affected overall segments of society and there are difficulties for economic and social life. Downward movements in the basic economic and financial indicators were noted in this period. On the contrary, lots of scientists from different fields have attempted to gather data on this pandemic-level disease and uncover useful findings in the light of this data. At the same time, the WHO and OECD, as well as universities and various non-governmental organizations, provide a rapid flow of data on the epidemic, effectively informing societies and researchers.

Many researchers have attempted to reduce the spread of COVID-19 in the literature since its inception. Therefore, a rapidly growing literature, especially in fuzzy clustering algorithms, has formed since the first time the COVID-19 outbreak appeared.

Fuzzy clustering algorithms reveal fuzzy partitions where observations can be roughly assigned to one cluster. Bezdek (1981) suggested fuzzy C-means (FCM) clustering, which is one of the most widely utilized fuzzy clustering algorithms [1]. Nevertheless, there is a basic disadvantage to this algorithm, which is its sensitivity to noise and outliers. In order to deal with wrongfully stated data as well as imprecise knowledge and facts, intuitionistic fuzzy set may be an effective tool. An IFCM that is a stretched version of this method is offered by Zhang and Chen (2007), Xu, Chen, and Wu (2008), and Chaira (2011) [2-4]. Also, a clustering algorithm supported by IFS is presented by R. Bhargava et al. [5]. The applications of IFCM were demonstrated in a few recently published papers (see [6-10]). Finally, the convergence theorem of IFCM was recently provided by Lohani et al. [11], and other sorts of convergence are disputed by them in [12-14].

In recent years, thanks to the big application areas of IFCM, it has developed quite well-liked algorithms, and there are also many interesting applications in areas biology, medicine, engineering, economics and finance [14-21]. It should be noted that the FCM clustering algorithms have been studied since the first time the COVID-19 outbreak appeared in the literature. Due to the use of the fuzzy clustering method, which allows them to be grouped in accordance with the resemblance of the characteristics and structures of time series, which set the dynamics of the epidemic process in them, a bibliographical investigation revealed that the COVID-19 pandemic has analogue patterns of development in various countries [22-24]. It can be summarized that, depending on the analysis, patterns in the incidence of coronavirus infection are administered to small groups of geographical countries or regions. M.R. Mahmoudi et al. (2020) [22] compared the rate of spread of COVID-19 in high-risk countries using a fuzzy clustering system. W. Dink et al. (2020) investigated the possibility of early detection of COVID-19 from radiographic images using unsupervised fuzzy clustering [23]. O. Castillo and P. Melin (2021) used a novel clustering method based on an intelligent fuzzy fractal approach to investigate COVID-19 data [24].

Our study is one of the first in the literature, in connection with the COVID-19 pandemic, to implement IFCM clustering. For such a high-dimensional grouping problem with many missing values, fuzzy clustering methods such as fuzzy C-means clustering are not very effective. In this study, we use the IFCM clustering method. Our primary objective is to provide an intuitionistic fuzzy C-means cluster analysis of 62 countries worldwide based on the cumulative confirmed COVID-19 cases, cumulative confirmed COVID-19 deaths, life expectancy, human development index, fatality rate, and population density using by IFCM algorithm.

The aim of this paper is to provide a dynamic structure for summarizing status and analysis results for countries both globally and in Turkey using current COVID-19 data. Moreover, this research allows us to track the daily flow, movement, and changes in cases and deaths around the world and on a country-by-country basis as descriptive statistics related to COVID-19 on a graph.

The rest of the paper is organized as follows: a short introduction to intuitionistic fuzzy sets is given in Section 2. The methodology of the intuitionistic fuzzy C-means clustering algorithm is offered in Section 3. Section 4 presents an application of intuitionistic fuzzy C-means clustering algorithms to model COVID-19 cases for countries worldwide. Finally, the essential results evaluated during this study are summarized, and a few proposals for further research are attributed in Section 5.

2. INTUITIONISTIC FUZZY SETS (IFS)

Zadeh (1965) established fuzzy set theory as elements have differentiating degrees of membership, which is an extension of classical set theory [25]. The basic idea of this theory is to treat uncertainty using membership values. Here, it may not always be adequate as the membership values. Atanassov (1986) suggested a generalization of fuzzy sets as intuitionistic fuzzy sets [26]. An additional uncertainty parameter, which is the hesitation degree, is also debated in the IFS theory. In clustering, there has been a prevalent study of the intuitionistic fuzzy set theory, which is constantly utilized as a method due to simplicity and its flexibility within the literature.

Each fuzzy element x in IFS is assigned a membership value and a non-membership value with some hesitancy, and this hesitancy is caused by incomplete information about x . As a result, it cannot forecast a more precise membership and non-membership value. As a result, both the membership value and the non-membership value specified in x may be incorrect. Mathematically, an intuitionistic fuzzy set A in X , is introduced as follows:

$$A = \{x, \mu_A(x), v_A(x) / x \in X\}$$

where $\mu_A(x) \rightarrow [0, 1]$, $v_A(x) \rightarrow [0, 1]$ are the membership and non-membership degrees of an element x in the set A with the condition

$$0 \leq \mu_A(x) + v_A(x) \leq 1$$

When $v_A(x) = 1 - \mu_A(x)$ for each x in set A , the set A becomes fuzzy. In addition, Atanassov demonstrated a hesitation degree, $\pi_A(x)$, which appears due to a lack of knowledge in defining the membership degree of each element x in set A for all intuitionistic fuzzy sets, and is introduced by:

$$\pi_A(x) = 1 - \mu_A(x) - v_A(x)$$

where it is clear that $0 \leq \pi_A(x) \leq 1$. Because of the hesitation level, the membership values reach out in the interval; $[\mu_A(x), \mu_A(x) + \pi_A(x)]$. If $\pi_A(x) = 0$, then $v_A(x) = 1 - \mu_A(x)$. Thus, A reduces to a fuzzy set [4].

3. IFCM CLUSTERING ALGORITHM

Clustering analysis is a statistical method that allows you to describe the common characteristics of the units, collecting the units examined in a study according to their similarities. Fuzzy clustering analysis helps cope with the uncertainty of real numbers to reveal appropriate clustering models for daily life experience. One of the most prevalent blurred clustering algorithms is fuzzy C-means (FCM) clustering. However, this algorithm has one main drawback, which is the noise and, on the contrary, the sensitivity of the values. The intuitionistic fuzzy C-means (IFCM) clustering is a proper tool for dealing with flawlessly given facts, data, and non-precision information. Chaira's method is utilized, and its algorithm in this study is defined as follows:

Algorithm: Intuitionistic Fuzzy C-Means Clustering Algorithm

The IFCM algorithm's first task is to transform crisp data into fuzzy data, which is then transformed into intuitionistic fuzzy data.

Step 1. $u_{ik}, i = 1, 2, \dots, c; k = 1, 2, \dots, n$ is the membership value of k^{th} data in i^{th} cluster.

The parameters are used to generate $r_{ik}, i = 1, 2, \dots, c; k = 1, 2, \dots, n$ values from a uniform distribution (0,1). The membership values are calculated using Eq. (1).

$$u_{ik} = \frac{r_{ik}}{\sum_{i=1}^c r_{ik}} \quad (1)$$

Step 2. Eqs. (2) and (3) are used to compute the hesitation degree (π_{ik}) and intuitionistic fuzzy membership (u_{ik}^*) values, in turn

$$\pi_{ik} = 1 - u_{ik} - (1 - u_{ik}^\alpha)^{1/\alpha}, \alpha > 0 \quad (2)$$

$$u_{ik}^* = u_{ik} + \pi_{ik} \quad (3)$$

The intuitionistic membership values (u_{ik}^*) are kept in U_{old} matrix.

Step 3. Centers of clusters (v_i^*) are computed by taking Eq. (4)

$$v_i^* = \frac{(u_{ik}^*)^m x_k}{\sum_{k=1}^n (u_{ik}^*)^m}; i = 1, 2, \dots, c \quad (4)$$

x_k is the k^{th} data and m is the fuzziness index.

Step 4. The membership values are get up to date with taking Eq. (5)

$$u_{ik} = \frac{1}{\sum_{k=1}^n \left(\frac{d_{ik}}{d_{jk}}\right)^{2/(m-1)}}; i = 1, 2, \dots, c; k = 1, 2, \dots, n \quad (5)$$

where d_{ik} is the Euclidean distance measure between k^{th} data in i^{th} clustercenter and using Eq. (6) it is computed as:

$$d_{ik} = \sqrt{(x_k - v_i^*)^2} \quad (6)$$

Step 5. Hesitation degree (π_{ik}) and intuitionistic fuzzy membership (u_{ik}^*) values are updated in turn using Eqs. (2) and (3). The novel intuitionistic membership (u_{ik}^*) values are retained in the U new matrix.

Step 6. Stopping criteria is controlled.

4. APPLICATION

The WHO defines an outbreak as the extensive spread of a recent disease, [12]. Since December 2019, there has been a significant report about over 167 million confirmed cases and 3.46 million total deaths from COVID-19. Furthermore, because it spreads very promptly and expands readily, COVID-19 may be a mortal virus. So, resulting in less confidence within the economic process and a sharp comeback in investment, the prevalent outbreaks have a deep historical impression on economic and social development.

During this application, we use the IFCM clustering algorithm for the 62 countries consistent with the basic variables associated with the COVID-19 pandemic. Data are observed over time, spanning from the first week of January 2020 to the last week of August 2021 [27]. Then, in the dataset, the relationship between the attributes (variables) is addressed, and the results obtained from clustering analysis are given. The data set includes date, numbers of cumulative confirmed COVID-19 cases and deaths, country name, country code, continental information, human development index from 1980 to 2017, population density from 1961 to 2017, life expectancy from 1543 to 2015, fatality rate.

In addition, additional attributes detailed below are calculated and added to the data set in order to better identify their similarities to the COVID-19 outbreak in clustering analysis, regardless of the geographical location of the countries. These qualities were expected to strengthen the IFCM clustering analysis. The main reasons why we prefer this algorithm are its simplicity, flexibility, and low computational complexity. The algorithm is obtained through cluster validity measures.

Because of the many dangers, the speed at which COVID-19 spreads requires particularly stringent policies and plans. Accordingly, it is very important to study the relationships between the breakdowns and the spread of this virus in other countries.

4.1. Data Sources

The distributions of the spread of COVID-19 in Austria, Azerbaijan, Australia, Bosnia and Herzegovina, Belgium, China, Costa Rica, Czech, Canada, Cyprus, Cuba, Denmark, Ethiopia, Ecuador, Egypt, France, Greece, Germany, Finland, Hungary, Indonesia, Iceland, Iraq, Israel, Ireland, Italy, Iran, Kazakhstan, Kenya, Japan, Malaysia, Norway, Mexico, Maldives, New Zealand, Nigeria, Netherlands, Pakistan, Palestine, Philippines, Peru, Portugal, Poland, Russia, Romania, Qatar, Switzerland, Saudi Arabia, South Korea, Sweden, Slovakia, South Africa, Slovenia, Ukraine, United Kingdom, Spain, Vietnam Venezuela, Turkey, Brazil, India, United States are compared and clustered using IFCM clustering technique. To study the relations of the distributions of the spread of COVID-19 among cumulative confirmed COVID-19 cases and deaths, human development index, population density, life expectancy and fatality rate are used and illustrated in Table 1.

Table 1. Used variables of the distributions of the spread of COVID-19

Variables ID	Variables
X_1	Cumulative confirmed COVID-19 cases
X_2	Cumulative confirmed COVID-19deaths
X_3	Life expectancy
X_4	Human development index
X_5	Fatality rate
X_6	Population density

The IFCM clustering analysis used six different variables, which are as follows and illustrated in detail in Figures 1-6. The figures are plotted by the R program.

Cumulative confirmed COVID-19 cases: The number of confirmed cases is more detailed than the total cases. The basis for this is testing.

Cumulative confirmed COVID-19 deaths: Limited tests and difficulties in determining the cause of death lead to the conclusion that the number of confirmed deaths cannot be an accurate count of the actual number of deaths caused by COVID-19.

Life expectancy: Life expectancy is the key metric for assessing population health. Life expectancy, which is wider than the narrow metric of infant and child mortality, which focuses only on mortality at a young age, captures mortality over the entire course of life. He tells us the typical age of death in the overpopulation.

Human development index: The Human Development Index (HDI) is a summarizing measure of average success in the three major aspects of human growth: having to live a healthy and long life, being knowledgeable, and having a reasonable standard of living. It is determined by:

- Average Life Expectancy at Birth
- Average and Projected Years of Schooling
- GNP for Each Head of Population (in PPP-adapted international dollars)

The HDI is the geometric mean of normalized indices for each of the three dimensions.

Fatality rate: The case fatality rate (CFR) is the ratio of confirmed deaths to confirmed cases. CFR can be a poor predictor of disease-related mortality.

Population density: The number of people per km² of land area [27].

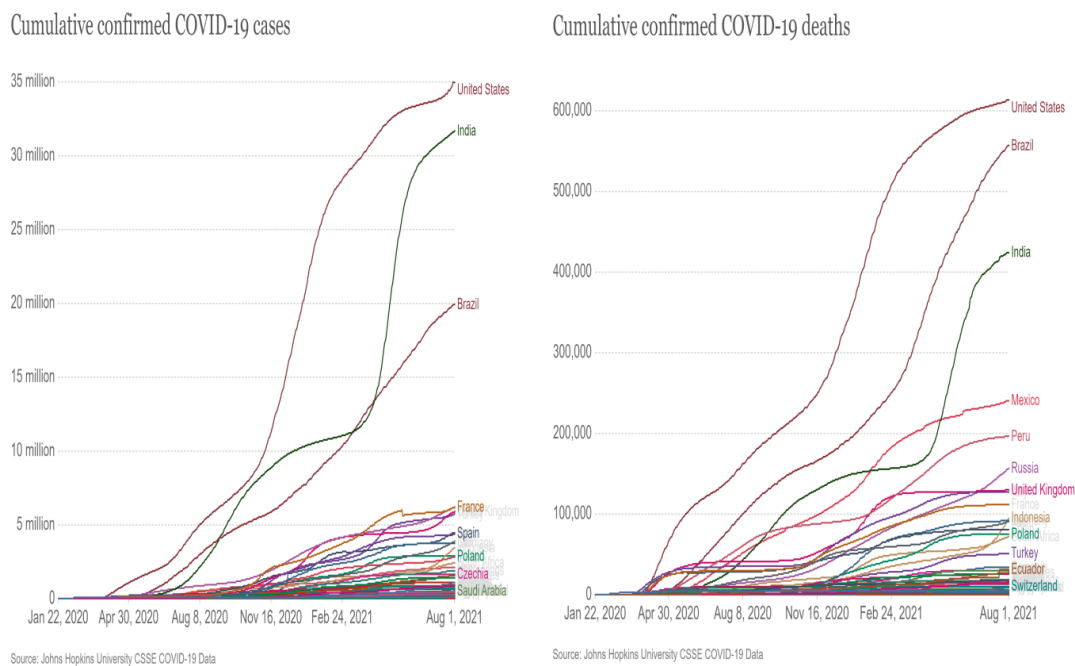


Figure 1. Plots of the variables of COVID-19 data set [28]

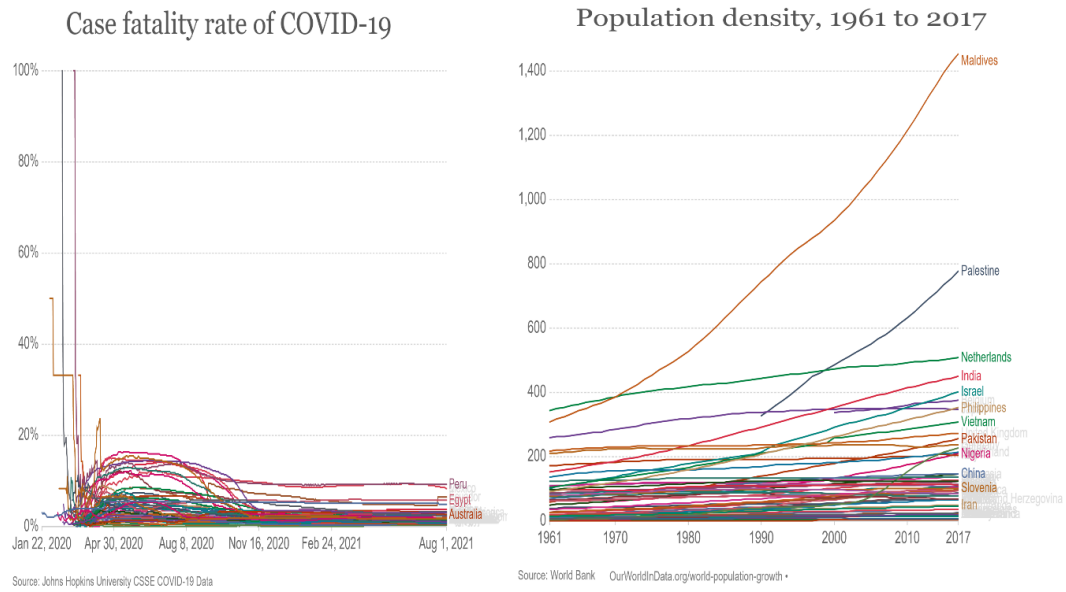


Figure 2. Plots of the variables of COVID-19 data set [28-29]

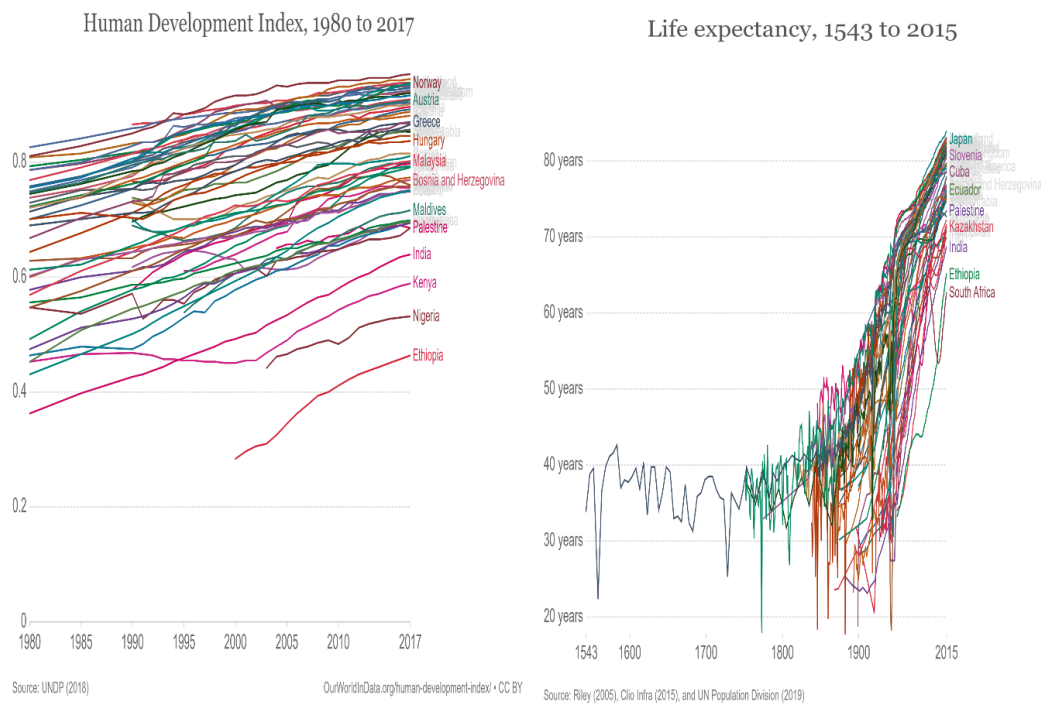


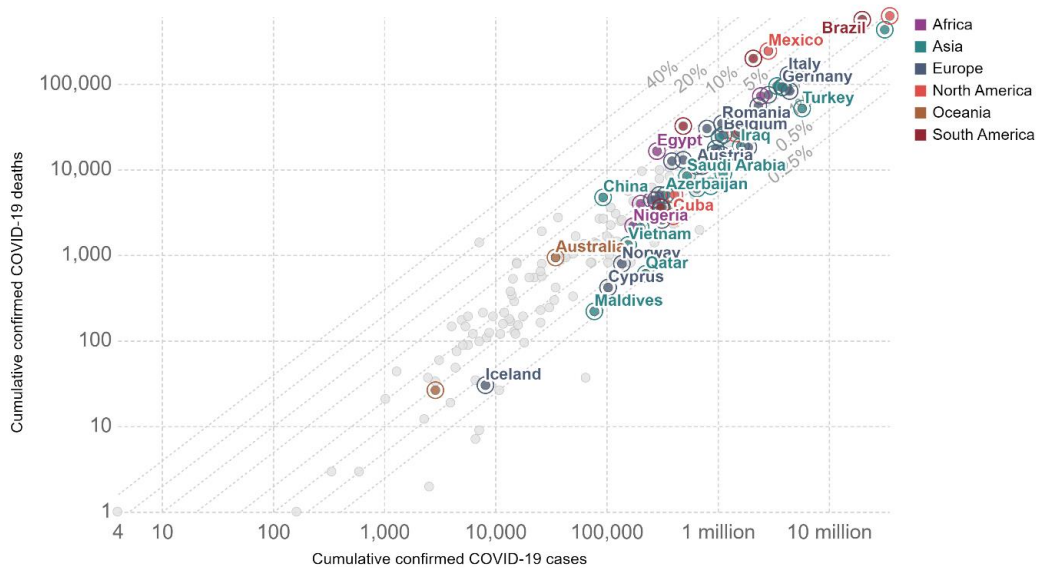
Figure 3. Plots of the variables of COVID-19 data set [30-31]

The graphs in Section 4, plotted the statistics related to the mentioned variables and the list of 62 COVID-19 affected countries until August 2021.

When we examined the number of cases, deaths, and case mortality rates from January 2020 to August 2021, the top 10 countries in the world were constantly displaced, especially Spain, Italy, Germany, France, Canada, and Turkey, while the increases were controlled, because the highest number of cases and deaths were in the USA, Brazil, and India which topped all countries in the world.

The situation of the graph comparing the number of cases and deaths in the countries is supported in Figure 4. Similarly, in Figure 5, where the number of deaths and case mortality rates are compared in the countries themselves, and in Figure 6, where the population density and number of deaths of countries are compared, the countries of the USA, Brazil, and India show proximity to each other.

It can be said that Turkey tends from critical to good due to the fact that case fatality rates are low compared to other countries, as well as the number of days needed to double the number of cases.



Source: Johns Hopkins University CSSE COVID-19 Data

Figure 4. Comparison of cumulative confirmed COVID-19 cases and deaths [28]

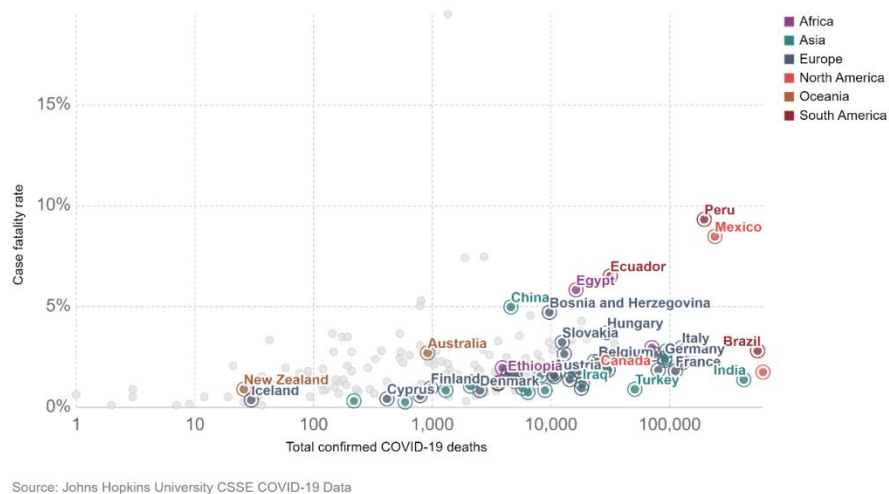


Figure 5. Comparison of cumulative confirmed COVID-19 deaths and case fatality rate [28]

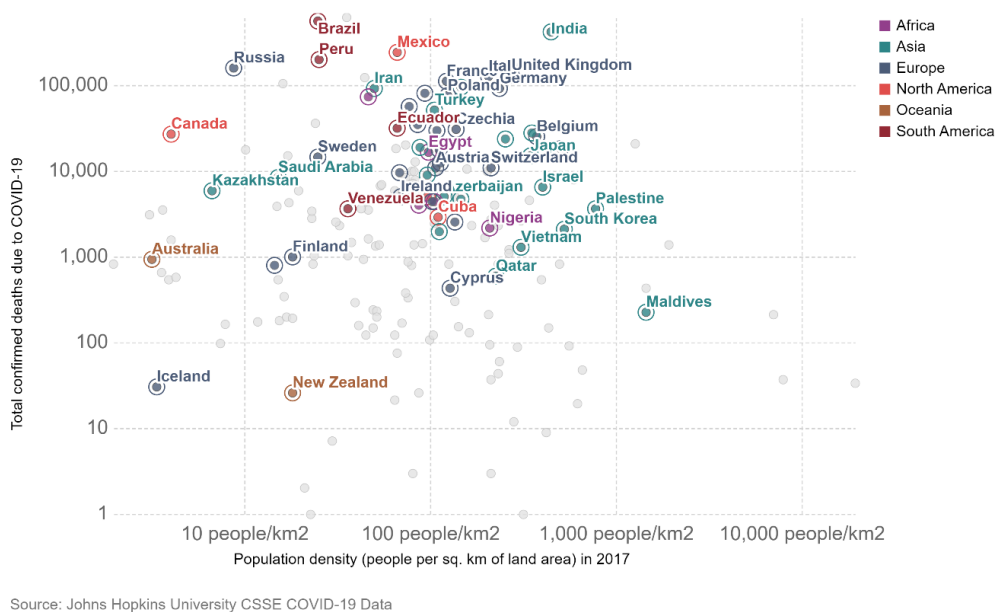


Figure 6. Comparison of cumulative confirmed COVID-19 deaths and population density [28]

4.2. Comparing of the Performances of Validity Indices

To test validity indices during a prevalent used genetics data set, comparing of defined indices above are finished the IFCM clustering algorithm. In total, different values for the fuzzier parameter in the algorithm were used, and the impact of the cluster number of adjusting values was observed. The test for convergence within the IFCM clustering algorithm was performed using $\epsilon = 10^{-5}$, and also the distance function $\| \cdot \|$ was defined as Euclidean distance, iteration number=100 and $c = 2$.

For the application, MATLAB 2018a, which is an environment for statistical computing program, was used. In an attempt to apply the algorithm, the initial parameters (excluding the quantity of clusters) were chosen randomly. It should be noted that the clustering quality or performance of a clustering algorithm is mostly evaluated by using the internal validity indices. In this paper, classification entropy (CE), the partition coefficient (PC), and the modified partition coefficient (MPC) results were calculated to work out the quantity of clusters. Apart from the MPC and PC validity indices using the maximum value, the optimum cluster result may be determined by the minimum index value in classification entropy (CE). In Table 2, the validation indices are given with respect to the number of clusters.

Table 2. Values of Validity Indices for IFCM Algorithm

Cluster Number	PC	MPC	CE
2	1.096	1.192	0.364
3	1.083	1.125	0.730
4	1.028	1.038	1.100
5	0.423	0.278	1.289
6	0.410	0.292	1.575
7	0.864	0.841	1.911
8	0.350	0.257	2.069
9	0.801	0.776	2.313
10	0.318	0.242	2.436

Since $c = 2$, PC and MPC reach its optimal (maximum) value 1.096 and 1.193, and CE also gets through its optimal (minimum) value 0.364 can be demonstrated in Table 2. In other words, PC, MPC and CE are up to find the optimal number of clusters as $c = 2$.

4.3. The IFCM Clustering Analysis

The number of clusters has been designated as 2. The clusters according to the countries are given in Table 3 as a result of the IFCM clustering analysis

Table 3. Clusters according to the countries

Cluster 1	Cluster 2
Austria, Azerbaijan, Australia, Belgium, Bosnia and Herzegovina, China, Costa Rica, Canada, Czech, Cyprus, Cuba, Denmark, Ethiopia, Ecuador, Egypt, France, Greece, Germany, Finland, Hungary, Indonesia, Iceland, Iraq, Israel, Ireland, Italy, Iran, Kazakhstan, Kenya, Japan, Malaysia, Norway, Mexico, Maldives, New Zealand, Nigeria, Netherlands, Pakistan, Palestine, Philippines, Peru, Portugal, Poland, Russia, Romania, Qatar, Switzerland, Saudi Arabia, South Korea, Sweden, Slovakia, South Africa, Slovenia, Ukraine, United Kingdom, Spain, Vietnam Venezuela, Turkey	Brazil, India, United States

To identify the number of clusters, PC, CE, and MPC validity indexes are used. Table 3 and Figure 7 ensure the fuzzy clustering technique results Table 3 and Figure 7 show how the number of cumulative confirmed COVID-19 cases and deaths, human development index, population density, life expectancy, and fatality rate in the 62 countries studied can be divided into two clusters. Based upon these values, the first cluster consists of Austria, Azerbaijan, Australia, Belgium, Bosnia and

Herzegovina, China, Costa Rica, Canada, Czech, Cyprus, Cuba, Denmark, Ethiopia, Ecuador, Egypt, France, Greece, Germany, Finland, Hungary, Indonesia, Iceland, Iraq, Israel, Ireland, Italy, Iran, Kazakhstan, Kenya, Japan, Malaysia, Norway, Mexico, Maldives, New Zealand, Nigeria, Netherlands, Pakistan, Palestine, Philippines, Peru, Portugal, Poland, Russia, Romania, Qatar, Switzerland, Saudi Arabia, South Korea, Sweden, Slovakia, South Africa, Slovenia, Ukraine, United Kingdom, Spain, Vietnam Venezuela, Turkey (with probabilities 0.76, 0.98, 0.63, 0.88, 0.94, 0.72, 0.38, 0.87, 0.18, 0.14, 0.84, 0.89, 0.61, 0.92, 0.59, 0.857, 0.07, 0.94, 0.92, 0.63, 0.38, 0.57, 0.44, 0.26, 0.76, 0.64, 0.65, 0.95, 0.95, 0.56, 0.65, 0.75, 0.38, 0.48, 0.81, 0.65, 0.23, 0.41, 0.91, 0.11, 0.71, 0.46, 0.28, 0.76, 0.92, 0.66, 0.60, 0.61, 0.96, 0.93, 0.77, 0.54, 0.34, 0.24, 0.72, 0.66, 0.77, 0.99, 0.34). Brazil, India, and the United States are also part of the second cluster (with probabilities 0.85, 0.99, 0.97).

Scattering of the clusters which are acquired as a result of IFCM clustering algorithm are shown in Figure 7.

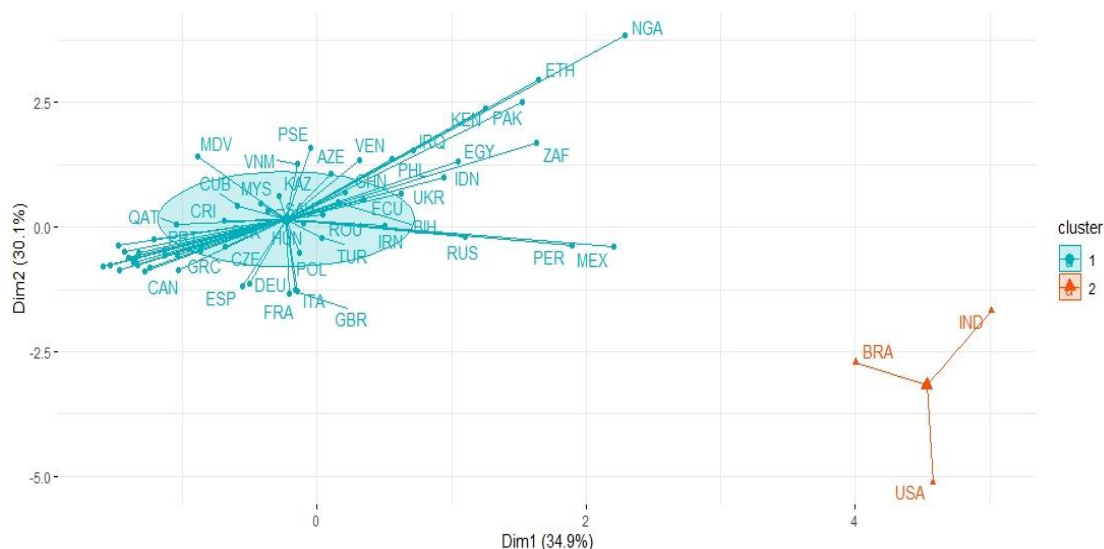


Figure 7. Plot of clustered COVID-19 data set with IFCM clustering algorithm

The grouping (clustering) of countries based on their similarities is one of the most important analyses of this study, and the results that can come from here can lead to cooperation and joint decisions on the measures and methods to be taken. The IFCM clustering analysis revealed.

According to statistical graphs of variables given in Section 4.1, the USA, Brazil, and India formed a cluster, and the other 59 countries formed a cluster. Because these three countries in Cluster 2 have been at their peak since the beginning of the outbreak, the cluster analysis has affected the result. When we look at the variable values of the three countries, especially in terms of total cases, deaths and case fatality rates, and when we examine these variables in terms of their relationship to each other, they are quite similar, which allowed them to be in the same cluster.

In Cluster 1, where Turkey is located, we see that there are more countries that have managed to control themselves since the beginning of the epidemic. Also, the similarity of the countries in Cluster 1, in which Turkey is located, especially in terms of the variables of total cases, deaths, and case death rates, caused them to be included in the same cluster.

Finally, the IFCM clustering algorithm is known to be based on the traditional FCM algorithm by adding intuitionistic features to membership and objective functions. The fuzziness level is minimized when a total of 62 countries are divided into two clusters with an accuracy rate of 95.2% using the IFCM clustering algorithm [32]. As a result of the analyzed characteristics, the countries are classified into two clusters: 59 countries in Cluster 1, and the remaining countries in Cluster 2. When the resulting group structures are examined, it is determined that Group 2 has a more decisive grouping than Group 1.

5. CONCLUSION

It is critical to investigate the relationships between the distributions of the spread of this virus in other countries in order to pay attention to COVID-19 management policies and plans. The distributions of COVID-19 spread in high-risk countries were compared and clustered in this study using the IFCM clustering technique. For example, COVID-19 data sets were compared and clustered using the IFCM clustering technique for countries such as Austria, Azerbaijan, Australia, Belgium, Bosnia and Herzegovina, China, Costa Rica, Canada, Czech, Cyprus, Cuba, Denmark, Ethiopia, Ecuador, Egypt, France, Greece, Germany, Finland, Hungary, Indonesia, Iceland, Iraq, Israel, Ireland, Italy, Iran, Kazakhstan, Kenya, Japan, Malaysia, Norway, Mexico, Maldives, New Zealand, Nigeria, Netherlands, Pakistan, Palestine, Philippines, Peru, Portugal, Poland, Russia, Romania, Qatar, Switzerland, Saudi Arabia, South Korea, Sweden, Slovakia, South Africa, Slovenia, Ukraine, United Kingdom, Spain, Vietnam, Venezuela, Turkey, Brazil, India, United States. The IFCM clustering algorithm was first applied to the relationship between the spread of the COVID-19 pandemic in this study. Moreover, the relationship between the spread of COVID-19 and six variables was examined. The obtained results showed that there were effective and important differences between the cumulative confirmed cases, cumulative deaths, and other variables between the countries. And, the distribution of distribution in Brazil, the USA and India is roughly similar but differs from other countries. Also, a clustering accuracy of over 95% can be achieved, which can be considered good to describe and deal with vague and uncertain data for this study. Furthermore, the IFCM algorithm can consider uncertainty information, which is critical for the success of some clustering tasks. For the future studies, the authors recommend that researchers classify statistical models that include fuzzy regression and fuzzy time series analysis, as well as fuzzy neural networks that can be applied to COVID-19 datasets.

ACKNOWLEDGEMENTS

Authors don't have any financial relationship with an organization that sponsored the research and didn't receive any compensation or consultancy work. This study didn't receive any other financial support.

CONFLICT OF INTEREST

The authors declare that they have no conflict of interests. There aren't any potential conflicts of interests that are directly or indirectly related to the research.

AUTHORSHIP CONTRIBUTIONS

All authors contributed to the study conception and design. Material preparation, data collection and analysis were performed by Nihal Ince and Sevil Senturk. All authors read and approved the final manuscript.

REFERENCES

- [1] Bezdek JC. Pattern Recognition with Fuzzy Objective Function Algorithms. Springer US; 1981.
- [2] Xu Z, Chen J, Wu J. Clustering algorithm for intuitionistic fuzzy sets. *Information Sciences*. 2008;178(19):3775-3790.
- [3] Xu Z, Wu J. Intuitionistic fuzzy C-means clustering algorithms. *Journal of Systems Engineering and Electronics*. 2010;21(4):580-590.
- [4] Chaira T. A novel intuitionistic fuzzy C means clustering algorithm and its application to medical images. *Applied Soft Computing*. 2011;11(2):1711-1717.
- [5] Bhargava R, Tripathy BK, Tripathy A, Dhull R, Verma E, Swarnalatha P. Rough intuitionistic fuzzy C-means algorithm and a comparative analysis. *Proceedings of the 6th ACM India Computing Convention*. Published online August 22, 2013.
- [6] Chowdhary CL, Acharjya DP. Segmentation of Mammograms Using a Novel Intuitionistic Possibilistic Fuzzy C-Mean Clustering Algorithm. *Nature Inspired Computing*. Published online October 4, 2017:75-82.
- [7] Parvathavarthini S, Karthikeyani Visalakshi N, Shanthi S, Lakshmi K. An Application Of Pso-Based Intuitionistic Fuzzy Clustering To Medical Datasets. *ICTACT Journal on Soft Computing*. 2017;8(1):1531-1538.
- [8] Kaur P, Soni AK, Gosain A. Novel Intuitionistic Fuzzy C-Means Clustering for Linearly and Nonlinearly Separable Data. *WSEAS Transactions on Computers*. 2012;11.
- [9] Tripathy BK, Basu A, Govel S. Image segmentation using spatial intuitionistic fuzzy C means clustering, 2014 IEEE International Conference on Computational Intelligence and Computing Research, Coimbatore, India, 2014, 1-5.
- [10] Kumar S, Shukla AK, Muhuri PK, Lohani QMD. Atanassov Intuitionistic Fuzzy Domain Adaptation to contain negative transfer learning. 2016 IEEE International Conference on Fuzzy Systems (FUZZ-IEEE), Vancouver, BC, Canada, 2016, 2295-2301.
- [11] Danish Lohani QM, Solanki R, Muhuri PK. A convergence theorem and an experimental study of intuitionistic fuzzy c-mean algorithm over machine learning dataset. *Applied Soft Computing*. 2018;71:1176-1188.
- [12] Mursaleen M, Danish Lohani QM. Intuitionistic fuzzy 2-normed space and some related concepts. *Chaos, Solitons & Fractals*. 2009;42(1):224-234.
- [13] Mursaleen M, Lohani QMD, Mohiuddine SA. Intuitionistic fuzzy 2-metric space and its completion. *Chaos, Solitons & Fractals*. 2009;42(2):1258-1265.
- [14] Verma H, Gupta A, Kumar D. A modified intuitionistic fuzzy c-means algorithm incorporating hesitation degree. *Pattern Recognition Letters*. 2019;122:45-52.
- [15] Kizilaslan B, Egrioglu E, Evren AA. Intuitionistic fuzzy ridge regression functions. *Communications in Statistics - Simulation and Computation*. 2019;49(3):699-708.

- [16] Egrioglu E, Bas E, Yolcu OC, Yolcu U. Intuitionistic time series fuzzy inference system. *Engineering Applications of Artificial Intelligence*. 2019;82:175-183.
- [17] Kaushal M, Lohani QMD. Generalized intuitionistic fuzzy c-means clustering algorithm using an adaptive intuitionistic fuzzification technique. *Granul. Comput.* 2022; 7, 183–195.
- [18] Kala R, Deepa P. Spatial Rough Intuitionistic Fuzzy C-Means Clustering for MRI Segmentation. *Neural Processing Letters*. 2021;53(2):1305-1353.
- [19] Hao NX, Ali M, Smarandache F. An intuitionistic fuzzy clustering algorithm based on a new correlation coefficient with application in medical diagnosis. *Journal of Intelligent & Fuzzy Systems*. 2019;36(1):189-198.
- [20] Dogan O, Oztaysi B, Fernandez-Llatas C. Segmentation of indoor customer paths using intuitionistic fuzzy clustering: Process mining visualization. *Journal of Intelligent & Fuzzy Systems*. 2019:1-10.
- [21] Wu L, Gao H, Wei C. VIKOR method for financing risk assessment of rural tourism projects under interval-valued intuitionistic fuzzy environment. Zhang J, ed. *Journal of Intelligent & Fuzzy Systems*. 2019;37(2):2001-2008.
- [22] Mahmoudi MR, Baleanu D, Mansor Z, Tuan BA, Pho KH. Fuzzy clustering method to compare the spread rate of Covid-19 in the high risks countries. *Chaos, Solitons & Fractals*. 2020;140:110230.
- [23] Ding W, Chakraborty S, Mali K, et al. An Unsupervised Fuzzy Clustering Approach for Early Screening of COVID-19 from Radiological Images. *IEEE Transactions on Fuzzy Systems* 2022; 30(8):2902-2914.
- [24] Castillo O, Melin P. A Novel Method for a COVID-19 Classification of Countries Based on an Intelligent Fuzzy Fractal Approach. *Healthcare*. 2021;9(2):196.
- [25] Zadeh LA. Fuzzy sets. *Information and Control*. 1965;8(3):338-353.
- [26] Atanassov KT. Intuitionistic fuzzy sets. *Fuzzy Sets and Systems*. 1986;20(1):87-96.
- [27] Roser M, Ritchie H. Coronavirus Disease (COVID-19). *Our World in Data*. 2020;1(1). <https://ourworldindata.org/coronavirus>
- [28] CSSEGISandData. COVID-19 Data Repository by the Center for Systems Science and Engineering (CSSE) at Johns Hopkins University. GitHub. Published 2022. <https://github.com/CSSEGISandData/COVID-1>
- [29] World Bank. World Development Indicators. *Worldbank.org*. Published October 28, 2019. <http://data.worldbank.org/data-catalog/world-development-indicators>
- [30] Human Development Reports. *Undp.org*. Published 2019. <http://hdr.undp.org/en/indicators/137506#>

- [31] Zijdeman R, Ribeira da Silva F. Life Expectancy at Birth (Total). IISH Data Collection. Published December 14, 2015. <https://datasets.socialhistory.org/dataset.xhtml?persistentId=hdl:10622/LKYT53>
- [32] Zang W, Ren L, Jiang Z, Liu X. Modified Kernel-based Intuitionistic Fuzzy C-means Clustering Method Using DNA Genetic Algorithm. *Journal of Software Engineering*. 2017;11(2):172-182.